Modelling of waves generated by landslides. Discontinuous and continuous approaches and focus on energy transfers

Lucie Clous

▶ To cite this version:

Lucie Clous. Modelling of waves generated by landslides. Discontinuous and continuous approaches and focus on energy transfers. Reactive fluid environment. Université de Pau et des Pays de l'Adour, 2018. English. NNT : . tel-02366629

HAL Id: tel-02366629
https://hal.science/tel-02366629v1

Submitted on 16 Nov 2019

HAL is a multi-disciplinary open access archive for the deposit and dissemination of scientific research documents, whether they are published or not. The documents may come from teaching and research institutions in France or abroad, or from public or private research centers.

L'archive ouverte pluridisciplinaire **HAL**, est destinée au dépôt et à la diffusion de documents scientifiques de niveau recherche, publiés ou non, émanant des établissements d'enseignement et de recherche français ou étrangers, des laboratoires publics ou privés.

N° attribué par la bibliothèque

THÈSE

PRÉSENTÉE À

L'UNIVERSITÉ DE PAU ET DES PAYS DE L'ADOUR

ÉCOLE DOCTORALE DES SCIENCES EXACTES ET DE LEURS APPLICATIONS

PAR

Lucie Clous

POUR OBTENIR LE GRADE DE

DOCTEUR

Spécialité: Mécanique des fluides

5 décembre 2018

Modelling of waves generated by landslides. Discontinuous and continuous approaches and focus on energy transfers.

Après avis de :

Finn Løvholt	Rapporteur
Anne Mangeney	Rapporteur
Stéphane Popinet	Rapporteur

Devant la commission d'examen formée de :

Stéphane Abadie	Directeur de thèse
Philippe Gondret	Examinateur
Yves Le Guer	Examinateur
Raphaël Paris	Examinateur

CONTENTS

LIST OF FIGURES

LIST OF TABLES

NOMENCLATURE

Acronyms

CFD	Computational Fluid Dynamics
DEM	Discrete Element Method
LES	Large Eddy Simulation
PIV	Particle Image Velocimetry
PTV	Particle Tracking Velocimetry
RAVEX	Risques Associés aux Volcanisme EXplosif
SPH	Smoothed Particle Hydrodynamics
TANDEM	Tsunamis in the Atlantic and the English ChaNnel: Definition of the Effects through numerical Modeling
VOF	Volume Of Fluid

Greek Symbols

Δt	Time step	s
Δx	Mesh size in direction $\underline{x}$	m
Δy	Mesh size in direction $\underline{y}$	m
$\mu(I)$	Friction coefficient	
μ	Viscosity	$Pa \cdot s$
Φ	Rate of the viscous dissipation	$J.s^{-1}$
ϕ	Colour function	
ρ	Density	$kg \cdot m^{-3}$
ρ_s	Slide density	$kg \cdot m^{-3}$
τ	Viscous stress tensor	Pa

Roman Symbols

$\underline{b}$	Volume force	$N \cdot m^{-3}$
$\underline{v}$	Velocity	$m \cdot s^{-1}$
C	Disc center	
d	Diameter of the grain	m
d	Relative density	
D_2	Second invariant of the strain rate tensor	s^{-1}
e	Newton's coefficient of restitution	

E_k	Kinetic energy	J
E_m	Mechanical energy	J
E_p	Potential energy	J
Fr	Froude number	
h_g	Gate opening height	m
h_r	Height of fluid in the reservoir	m
I	Inertial coefficient	
m	Disc mass	kg
N_D	Number of discs	
P	Impulse product parameter	
p	Pressure	Pa
R	Disc radius	m
r	Disc radius	m
V	Disc velocity	$m.s^{-1}$
X	Disc center coordinates	m
$\underline{g}$	Gravitational acceleration	$m.s^{-2}$
$\underline{\underline{D}}$	Strain rate tensor	s^{-1}

GENERAL INTRODUCTION

Tsunamis can be triggered by subaerial or submarine landslides involving numerous types of gravitational mass movements from dry to wet media more or less cohesive and moving at different velocities (Figure 1). For instance, amongst the long list of landslide tsunamis, two of the most treated examples in the litterature are the Lituya Bay tsunami generated by a subaerial landslide (Figure 2a) and the submarine Storegga slide for which tsunami evidences have been found all along the Norwegian coast, in Scotland and Greenland (Figure 2b). Wave generation by subaerial and submarine lansdlide are two kind of processes which are treated in this thesis.

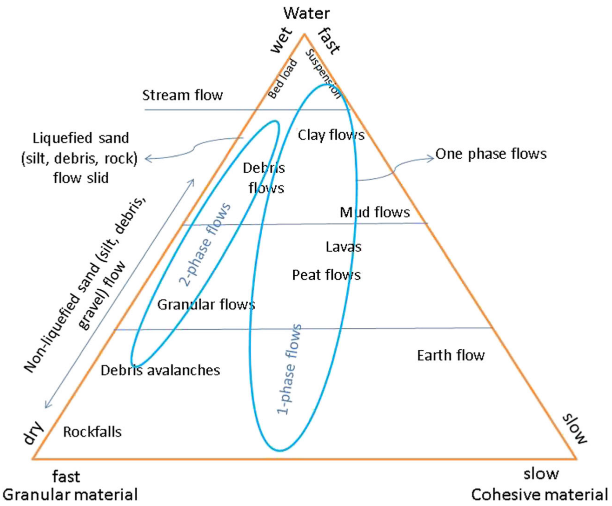

Figure 1: A classification of the gravitational mass movements as a function of water content (dry-wet), velocity (slow-fast), and material type (granular-cohesive) from Yavari-Ramshe & Ataie-Ashtiani [98]

Two mechanisms studied in this thesis are also volcanic tsunamis: wave generation by pyroclastic flows and slope instabilities.

Pyroclastic flows are gravity currents produced by explosive volcanoes. They are composed of a mixture of hot gas and particles of variable size. Evidences of tsunamis generated by pyroclastic density currents (PDC) have been found from tide gauges, deposits and observations for eruptions of Montserrat 2003 (maximum run-up of $4\,m$ in

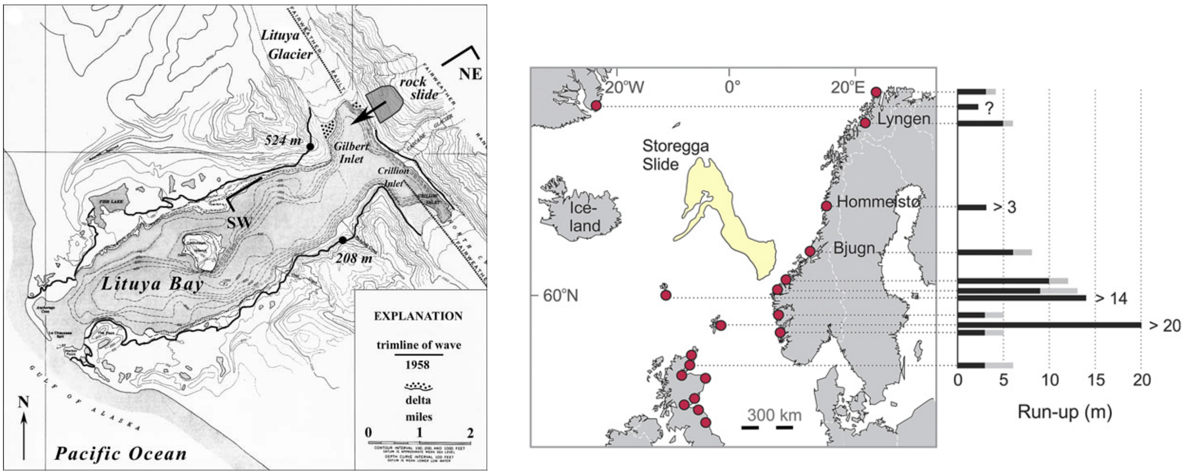

(a) Map showing topographic and bathymetric contours, trace of Fairweather fault, 1958 landslide and trimline of tsunami runup, from Fritz et al. [26]

(b) Location of deposits of the tsunami triggered by the Storegga slide indicated by red dots and reconstructed run-up heights from field evidence, from Bondevik et al. [7]

Figure 2: Two examples of landslide tsunami triggered by a subaerial slide (a) and submarine slide (b)

Montserrat and 1 m in Guadeloupe, Pelinovsky et al. [73]) and Rabaul 1994 (maximum run-up of 8 m in Rabaul Bay, Nishimura et al. [69]). Among the mechanisms that generated the tsunamis during the Krakatau eruption of 1883, pyroclastic flows are considered to be the principal source (Carey et al. [10]).

Most volcanoes have slope instabilities due to their high relief, steep slopes, the layers of more or less cohesive materials (Figure 3). The size of the volcanic landslides is in average at least twice the size of nonvolcanic landslides. These failure can be triggered by earthquakes or during eruptions but not always and which makes them difficult to predict (Siebert [83]). Volcano flank failures cover a large spectrum from small landslides, rock fall to large debris avalanche. An example of the damage done by such landslides is the tsunami generated by the landslide on Iliwerung volcano in 1979, Indonesia which killed about 900 people on Lembata Island (Paris [70]).

Tsunamis generated by volcanoes are not rare particularly in south-east Asia (Figure 4). In Europe, Italian volcanoes for instance may also be a threat. More distant volcanoes can also be a concern for the distant national territories (e.g. Montagne Pelée, Lesser Antilles) or even for Europe (e.g. Cumbre Vieja Volcano, La Palma, Canary Islands, Ward & Day [90], Løvholt et al. [57], Abadie et al. [1]).

The case of the Cumbre Vieja Volcano was in the framework of the TANDEM project (Tsunamis in the Atlantic and the English ChaNnel: Definition of the Effects through numerical Modeling) in order to assess the risk associated to this volcano on the French Atlantic coast. Some results from the present thesis are being currently used in this

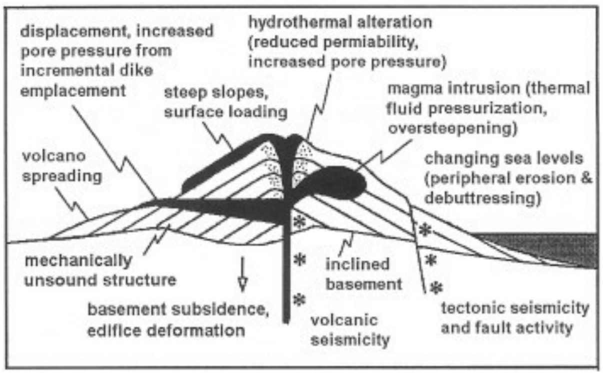

Figure 3: Factors contributing to structural instability of volcanic edifices, from Siebert [83]

program to improve the relevance of this assessment.

Part of this thesis was also carried out in the framework of the RAVEX project (Risques Associés au Volcanisme EXplosif) which aims to assess risks associated to explosive volcanism focusing on the Montagne Pelée case. Amongst those risks, we studied more specifically the wave generation by pyroclastic flows.

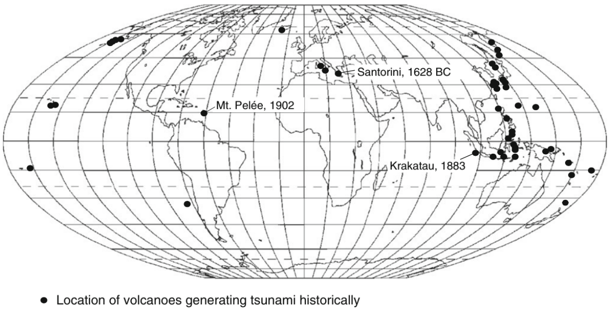

Figure 4: Location of volcanoes that have generated tsunami in recorded history, from Bryant [8]

The process of wave generation by landslide can be studied in laboratory experiments and numerical computations. Numerical models can also help to assess risks for different scenarios in real cases. Regarding wave generation by pyroclastic flows, there are only a few experimental studies available, although they are essential for the validation of numerical models and some of them are used in this study. Experimental results on granular media are presented. In the scope of the RAVEX project, new experiments for pyroclastic flow were planned and some of them are presented in this document.

In this framework, the general objective of the thesis is to propose several approaches for the modelling of wave generated by mass failure and validate them with the long term goal of better assess the risk associated to real cases such as the ones studied in RAVEX (Montagne Pelée) or TANDEM (Cumbre Vieja). The numerical study focuses on the understanding of the generation processes and the energy transfers.

The thesis is divided in five chapters:

- Chapter 1 outlines the state of the art of waves generated by landslides in terms of experimental and numerical studies.
- Chapter 2 presents the equations and methods employed for the numerical simulations.
- In Chapter 3, a model to deal with solid collision in a Navier-Stokes code is prensented and validated on one case.
- In Chapter 4, rheologies employed to model landslide as a continuous media are presented and applied on two experimental benchmarks.
- Chapter 5 deals with the validation of a model for wave generated by pyroclastic flow.

CHAPTER
ONE

STATE OF THE ART: WAVES GENERATED BY LANDSLIDES AND ENERGY TRANSFERS

Contents

Wave generation by landslide has been mainly studied with three approaches: laboratory experiments, analytical work and numerical simulations. Each of these approaches provides a specific level of understanding of the phenomenon.

In the following, the principal methods existing in literature and results are presented. The chapter is organised as follows:

- Experimental studies which present a process analysis of wave generation
- Numerical models for debris avalanches
- Flow description and the associated numerical models
- Wave generated by pyroclastic flow and the associated models
- Energy transfers in the wave generation process

1.1 Experimental studies

This section aims first to describe wave generation and processes involved and then to highlight the important parameters.

Experimental studies are presented in two categories: the ones involving rigid slide and those based on a deformable slide.

The rigid slide is the most simple approximation of a real slide. In this case, the slide is considered as one whole block which does not deform during the wave generation process.

The deformable slide model is closer to what is likely to occur in a real case. Nonetheless, the grain size varies in space and time during a real landslide which is very difficult to reproduce in experiments. Therefore, most of the experiments use beads of the same diameter. Hence, this approach can give an idea of the role of deformation and block size in wave generation compared to the rigid slide case but does not include the whole complexity.

1.1.1 Processes analysis

Rigid slide

Heinrich [38] studied the slide of a triangle solid block on a 45° incline. Two cases are presented, one with the block initially under water and one initially just above the free surface. In the submarine case, the block generates a wave exhibiting a first crest, followed by a big through, a crest of same amplitude as the through and then a wave train of three or four waves. The velocity of the first wave is $\sqrt{gh}$ (h being the water depth), corresponding to long wave celerity. The other waves are dispersive and travel at lower speed. The second crest is a nonlinear wave (crest amplitude greater than the throughs) and then evolves into a sinusoidal wave during the propagation phase. Unlike the submarine case, the subaerial case generates a first wave which has the greatest amplitude, followed by a wave train. The second difference is that the block initially above water entrains air while entering water, creating air cavities and wave breaking close to the slide.

Ataie-Ashtiani & Najafi-Jilani [4] studied the influence of shape and volume of the block, and slope angle on the waves generated in a submarine slide case. Ataie-Ashtiani & Nik-Khah [5] presented a similar study for subaerial landslides. In both cases, the wave pattern observed is a first through followed by the greatest crest and a wave train whatever the slide shapes and volumesand slope angle.

Deformable slide

Only a few studies are related to submarine deformable landslides, one of the reasons being the difficulty of properly setting up the underwater gate (i.e. disturb as little as possible the water and be watertight if it opens under the tank). For instance, experiments presented in Grilli et al. [31] consist in the release of a mass between 1.5 and 2.5 kg of glass beads with a diameter of 4 or 10 mm on a 35° slope. The water depth is between 0.320 and 0.370 mm, the slide is initially placed at a few centimetres under the free surface and has a triangular shape. When the beads are released, the slide deforms: first the triangular shape flattens and then a bulk is formed at the front of the slide and the rear gets thinner. The waves generated have the same pattern as described for rigid slide: a first crest followed by a large through, a second wave with the maximum amplitude and a wave train with decreasing amplitude.

Similar experiments were earlier performed by Viroulet [86]. In this case, the mass of glass beads were released just above the free surface. Unlike the submarine case, the slide front immediately forms a bulk as soon as it starts to slide and impacts water. The pattern of the generated waves is the same except that the first wave has the maximum amplitude. This behaviour was also observed in the subaerial experiment of Heinrich [38].

Data on actual cases are very rare. This is one of the motivations for laboratory experiments where part of a real geometry can be reproduced at smaller scale. Hence, Fritz et al. [25] reproduced at a 1 : 675 scale a cross section of the Gilbert Inlet in the Lituya Bay (Figure 1.1). The slide is modelled by a granular material with an average diameter of 4 mm. After the rockslide impact, a flow separation is observed which creates an air cavity, and an impulse wave is generated which propagates and runs up on the opposite incline. During the sliding sequence above water, the slide front inclination is gentle and its thickness increases continuously. After impact, the slide front forms a bulk. The air cavity collapses after the slide has reached the bottom and causes a mixing of water and air. This happens after the propagation of the leading wave and has therefore no effect on its generation. Waves are then reflected on both sides of the inlet.

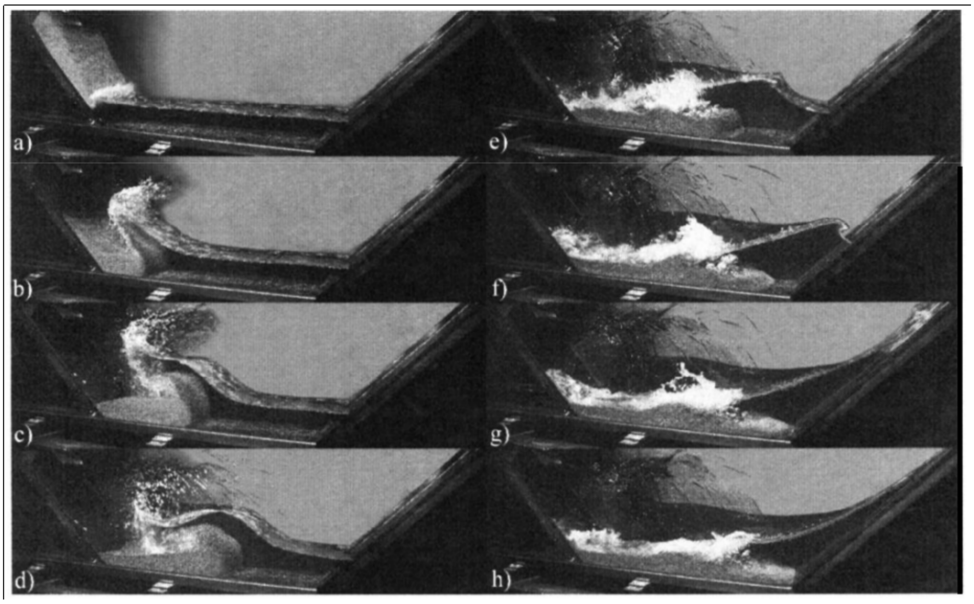

Figure 1.1: Photo-sequence of a granular slide impact experiment, time increment of 5s, from Fritz et al. [25]

Effect of slide deformation

The effects of slide deformation can be quantified based on experiments with similar initial conditions but using rigid blocks or a deformable medium. As an illustration, the experiments of Ataie-Ashtiani & Najafi-Jilani [4] and Ataie-Ashtiani & Nik-Khah [5] include both rigid and granular slides. They compare the wave train generated by deformable and rigid slides initiated from the same triangular shape and weight. In both submarine and subaerial test cases, the maximum wave crest amplitude appears reduced for the deformable slide (15 to 25% of reduction in submarine cases, 25 to 35% in subaerial cases, Figure 1.2) compared to the rigid slide. They also observed an increase in the period of the maximum wave: about 15% and 20 to 30% for submarine and subaerial cases respectively is also observed. The effect of slide deformation on wave characteristics is therefore not negligible. This shows that if a deformable slide is modelled by a rigid slide of same geometry, the maximum wave amplitude will be overestimated.

Summary of the processes involved

The examples mentioned above show the complexity of the water flow during the generation process. To sum up the processes presented above, generation of waves by landslides can lead to: creation of air cavities, air-water mixing, dispersive wave, non-linear wave, wave breaking, turbulence. A general observation is that submarine cases seems less complex in terms of the flow involved than subaerial cases as there is no impact, no air-water mixing, no wave breaking in the generation zone. Therefore, the model employed for numerical simulations has to be adapted to the specific situation.

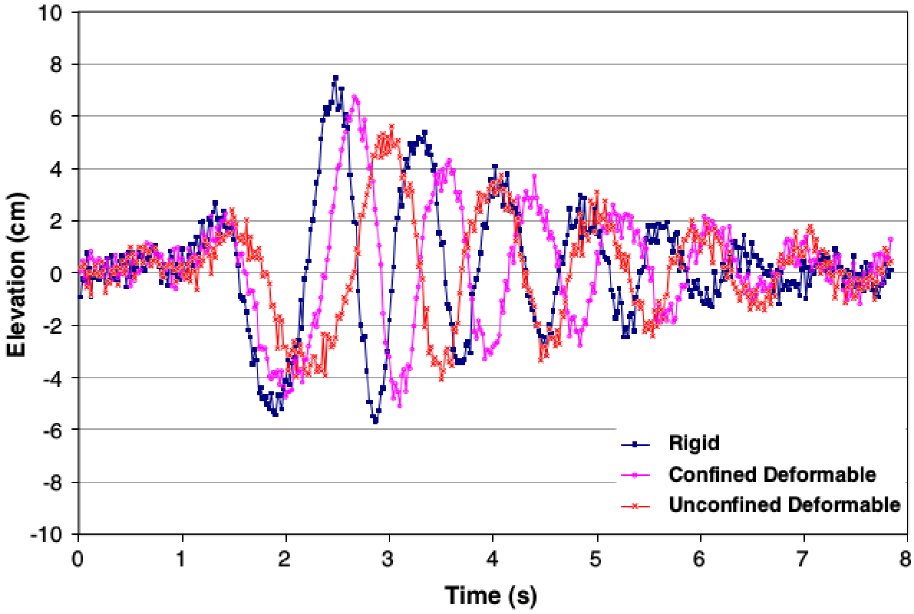

Figure 1.2: Subaerial slide rigidity effects on impulse wave feature, from Ataie-Ashtiani & Nik-Khah [5]

Waves types

The type of wave also varies with the slide characteristics during the generation phase which may subsequently have an influence on run-up height and wave force on structure. Fritz et al. [24] and Heller & Hager [42] classify the subaerial slide generated wave in function of the slide characteristics. During the experiments were observed Stokes-like, cnoidal-like, solitary-like and bore-like waves. The type of waves depends on the Froude number (computed with slide impact velocity and still water depth) and the relative slide thickness (maximum thickness of the slide at impact divided by water still depth) for Fritz et al. [24]. Heller & Hager [42] also add the slide impact angle and the relative slide mass in the parameter list. Heller & Hager [42] classified about 430 experiments including their study and two previous ones. But the classification does not hold for submarine slide, partly submerged slide or in the limit case of a subaerial case when the base of the slide levels the free surface as in all these cases, there are no slide characteristics at impact.

1.1.2 Influence of parameters on wave generation

For a dimensional analysis (Buckingham [9]), the parameters which can potentially influence the wave generation by landslides (Kamphuis & Bowering [49], Zweifel et al. [101], Fritz et al. [24], Heller & Hager [43], Mulligan & Take [67]) are: the volume, density, length, thickness, impact velocity, porosity of the slide, slide front angle, grain diameter, still depth water, slope angle.

Physical models

Physical models trying to relate the generated wave to the slide parameters are numerous. Among those, the semi-empirical models of Zweifel et al. [101] and Fritz et al. [24] are obtained with multiple regression on results of a high number of experiments (more than 100 and 200 for Fritz et al. [24] and Zweifel et al. [101] respectively) with the aim to predict impulse wave characteristics like maximum wave amplitude, wavelength or impact energy conversion ratio.

Heller & Hager [43] define an impulse product parameter P depending on governing parameters. P ((1.1)) is obtained by optimising the coefficients of determination of impulse wave parameters (relative maximum amplitude and relative wave period among others). This study tends to demonstrate that the more relevant parameters for wave generation by subaerial landslides are the Froude number Fr, the relative thickness S, the relative mass M and the slide impact angle α. The impulse wave characteristics can be determined using a simple expression depending only on the value of P in the slide impact zone and on a relative distance.

$$P = FrS^{1/2}M^{1/4}cos[(6/7)\alpha]^{1/2} \tag{1.1}$$

Analytical models

Analytical models developed to predict waves generated by landslides also give an indication on the governing parameters. For instance, the model of Mulligan & Take [67] solves the idealised momentum flux balance considering two conditions: dominantly hydrostatic or dominantly hydrodynamic. This model predicts the maximum wave amplitude in the near field. The model parameters are still water depth, slide density, thickness, impact velocity and slope angle. Their results are in agreement with the experimental results of Miller et al. [63] and Heller & Hager [43]. Moreover, this analytical model is also in agreement with the semi-empirical model of Heller & Hager [43]. It is however limited to dry granular subaerial slide on moderate slope.

Lo & Liu [56] also developed analytical models solving free surface elevation and flow velocity. By studying the wave generated for prescribed landslides of the same height and area but different shapes, they show that the slide area has more influence on the generated waves than the shape. In this sense, the slide area seems to be a critical parameter more important than the slide shape.

1.2 Numerical models of landslides

The most important slide numerical models are presented in this section divided in two subsections: rigid and deformable slides. This part focuses more specifically on the motion and deformation of the slide, not on wave generation.

1.2.1 Rigid slides

Moving boundaries

The simplest model for rigid slide is to impose the movement of the slide on the boundaries of the domain, i.e. the slide is a deformation of the bottom floor. The kinematics of the slide is prescribed. This method has the advantage of not having to manage the solid body in the domain. On the experiments presented previously, Heinrich [38] carried out a few computations imposing a moving boundary. The movement of the numerical slide is of course in agreement with experiments as it is prescribed. Similar validation computations were performed in by Grilli & Watts [34] with an idealised Gaussian shape.

Harbitz et al. [36] carried out simulations of the Tafjord event (1934) in Norway. They neglected the shear stress between masses and fluid, considering therefore the slide as a box with the total water displacement being the only important parameter for wave generation. The motion of the slide is prescribed following the method of Harbitz & Pedersen [35] to determine the slide characteristics. There are obviously no records of the slide during the event but run-up measurements along the fjord shoreline. With this simple method, they were able to obtain satisfactory run-up values.

The main limitation of this method is the no coupling between slide and waves as the motion is prescribed. From a laboratory experiment, one can get the motion of the slide but applications on real events are of course limited as the motion of the slide is never known.

Penalised fluid

The importance of coupling between water and slide is highlighted by Jiang & LeBlond [47].Abadie et al. [2] used a fluid penalised by viscosity to model a rigid landslide. This method will be described in section 3.3.4, but in a few words, the viscosity is set to a high value which allows to cancel the deformation term in the Navier-Stokes equations. This approach has the advantage of implicitly resolving the coupling previously mentioned. Abadie et al. [2] simulated the 2D submarine experiment of Heinrich [38] and the 3D experiment of a partially submerged rigid triangular body sliding down an incline (Liu et al. [55] experiment). The slide centre of mass displacement is shown to be in good agreement with experimental results (Figure 1.3).

Intermediate conclusion on rigid slide models

Assuming that only the general characteristics of the slide like its thickness, mass, velocity and volume are important in wave generation led to the rigid slide model. This first approximation can give an assessment of the wave amplitude and run-up heights. However, considering wave amplitudes observed in real events, a difference between 15 to 35% in these predictions due to the deformation of the slide (Ataie-Ashtiani & Najafi-Jilani [4], Ataie-Ashtiani & Nik-Khah [5]) can not be neglected.

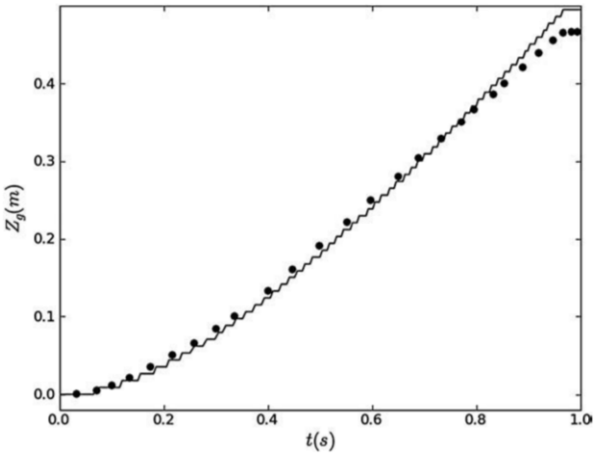

Figure 1.3: Time evolution of vertical slide displacement (dots), Heinrich's experiment (line): NS-TVD model simulations for a single rigid triangular block, from Abadie et al. [2]

1.2.2 Deformable slides

A second approach more elaborated is to take into account the landslide deformability. Most studies model the slide as a fluid based on different rheologies. Other approaches impose moving boundaries like for rigid slide or couple the fluid code with a solid code that solves the slide motion.

Moving boundaries

In a first paper, Watts et al. [95] studied the effect of deformation of submarine landslides using a parabolic shape. Comparing to a simulation with a modified Bingham model, they found that, at early stage, the movement of the slide centre of mass can be defined by a curve and the maximum thickness decreases linearly in time. They also showed that typical length and slide front position are proportional to the centre of mass position. Following this study, Grilli & Watts [34] applied this theory by imposing the movement of the slide as well as the slide thickness and length deformation working on the boundaries of a fully non-linear potential flow. The influence of the deformation on the generated waves was studied, and it was concluded that the characteristic tsunami amplitude increases for deforming slides compared to rigid slides in contrast with the observations of Ataie-Ashtiani & Najafi-Jilani [4].

Coulomb-like continuum medium

The Coulomb-like continuum model described in Savage & Hutter [81] is commonly used for landslides modelling (Yavari-Ramshe & Ataie-Ashtiani [98]). This model consists in modelling the intergranular stresses by a Coulomb friction.

For instance, Ma et al. [59] included the model of Iverson & Denlinger [46] in their two-layer granular landslide and tsunami model. The basal shear stress is a Coulomb-type friction law. There is no mixing between landslide and water and the continuity of the normal stress is imposed at the interface. The validation of the granular flow is realised by comparison with an analytical model. It is established that granular flow motion is well captured by the model. The model is also validated by simulating the 2D experiment of impulse waves generated by a subaerial landslide as presented in Heller [40] and Heller & Hager [43]. The slide profile was correctly except for a slight overprediction of the slide height. The slide velocity was also in good agreement with measurements. However, because of the use of a depth-averaged model, air cavities observed in the experiment are not present in the simulations. Additionnaly, because the Coulomb friction is not modified in the model after a change of slope, there is an overprediction of the slide front and wave height. The validation on a 3D experiments (Mohammed & Fritz [65]) gives similar conclusion: waves are slightly overpredicted.

Kelfoun et al. [51] also employed a two fluids model with a Coulomb-like continuum as landslide model for simulations on the Réunion Island volcano. The landslide rheological law was calibrated based on comparison with natural deposits. Unlike Ma et al. [59], imposing the basal shear stress as a constant frictional retarding stress, gave better results than the Mohr-Coulomb frictional law. From this calibration, simulations were carried out to predict the waves generated on the Reunion Island and Mauritius coasts for different scenarios of slide volume, type of collapse (single or retrogressive), and basal shear stress value.

Inviscid fluid

The inviscid fluid has no viscosity and therefore no tuning parameter can be used for calibration.

For instance, Abadie et al. [1] performed simulations of wave generated by the Cumbre Vieja Volcano flank collapse modelling the landslide by an inviscid fluid. Four scenarios were considered depending on slide volumes (i.e. 20, 40, 80 and 450 m^3). In this work, using an inviscid fluid for landslide model is interpreted as the worst case scenarios as there is no dissipation during the sliding.

Newtonian fluid

The Newtonian fluid includes viscous dissipation and has one parameter to calibrate, namely the viscosity.

Grilli et al. [31] simulated the experiments of wave generation by the submarine granular slide presented in section 1.1.1 and modelled the slide as a Newtonian fluid. A first approximation of the viscosity value is done by using a theoretical expression for suspension of water with a high concentration of glass beads (Eilers [20], Frankel & Acrivos [22], Quemada [78]). The viscosity is evaluated for the packing of randomly packed spheres.

By taking into account that the volume fraction decreases during the experiment as the slide runs down the incline, this viscosity value finally imposed in the model is lower than its evaluation from theoretical expressions. The influence of viscosity on wave generation is studied. Slide maximum velocity, and distance travelled by the slide at a given time are shown to drop off as the viscosity increases, also leading to a reduction of wave amplitudes. After validation on laboratory experiments, they applied the method on real geometry off the US East Coast. The model is calibrated using previous simulations with a rigid slide. The principal remark is that at this scale the slide motion is more sensitive to the bottom friction that viscosity.

Bingham fluid

The Bingham fluid is a non Newtonian fluid which flows when a specified shear stress is reached, hence the formation of a plug zone with no deformation and a shear zone during the flow. Therefore two parameters must be calibrated: yield stress and viscosity. It is usually employed for modelling snow, muds, submarine and river sediments or volcanic lava.

Jiang & LeBlond [48] used the Bingham fluid but limited their range of study to laminar cases (small incline angle) of underwater slides. Compared to a viscous fluid, the Bingham fluid travels to a finite distance and generates waves of smaller amplitudes but the evolution of the waves is quite similar. Energy transfer is greater for small values of yield stress (which lead to greater slide mobility), i.e. it is largest for a viscous fluid.

Coupling with a solid code

It is possible to couple a fluid code to a code capable of computing the motion of a large number of particles, therefore no rheology is applied to model the slide but it is represented by a set of solid blocs whose motions are solved by the solid code. This method allows water seepage between the solid bodies to be taken into account unlike the previous models which consider the slide as one fluid volume immiscible with water.

Zhao et al. [100] coupled a CFD (Computational Fluid Dynamics) code with a DEM (Discrete Element Method) code. They carried out simulation of the Vajont rockslide. The slide is modelled by relatively coarse grains (particles of diameter between 1.8 and $3.8\,m$) due to the high computational cost. The hydraulic conductivity of the model is two orders of magnitude larger than regular materials, which leads to a large permeability of the slope, i.e. the water flows back into the slope quickly. This can induce more fluid seepage than in reality. The run-up values are compared with available measurement and are found to be in relatively good agreement.

1.3 Numerical flow modelling

Different degrees of numerical flow modelling can be chosen depending on the details of interaction and on the processes which are needed for the aim of the study.

1.3.1 Shallow water equations

The shallow water equations are depth-averaged equations very commonnely used in literature. Even though it is more common for wave propagation, a few studies also employ them for wave generation (about 50% of the studies on landslide generated waves according to Yavari-Ramshe & Ataie-Ashtiani [98]).

In their simulations of the Tafjord event, Harbitz et al. [36] justify the use of linear shallow water equations by the hypothesis that landslide generated waves are long waves with a few non-linear effects. Non-linear effects can appear in the wave generation zone on a short period of time. However errors associated to the linear hypothesis are generally not greater that the errors generated by the approximations on the slide shape and motion. The shallow water approximation can be both applied to landslide and water waves. Heinrich et al. [39] compared a shallow water model and a Navier-Stokes model. Jiang & LeBlond [47] consider that the shallow water approximation can be taken only for small slope (between 1 and 10°).

From Lynett & Liu [58], the shallow water equations are valid only for submarine slides in very shallow water, i.e. a water depth above the slide 15 times greater than the characteristic horizontal length of the slide. From smaller ratio, dispersive effect can not be neglected and Boussinesq wave equations are recommended.

1.3.2 Boussinesq wave equations

Unlike shallow water equations, Boussinesq wave equations allow a non-constant value of velocity over depth, which is is often encountered during propagation and inundation (Watts, Grilli, Kirby, Fryer & Tappin [92]). Boussinesq-type models are usually employed for the propagation of waves because they take into account dispersive and non-linear effects but are not as expensive as Navier-Stokes models. Their use for wave generation by landslide is also somehow limited because of the depth-averaging. Nevertheless, there are a few studies of this kind in the litterature.

For instance, Ataie-Ashtiani & Yavari-Ramshe [6] extended the model of Lynett & Liu [58] to a fourth-order scheme. After a validation with experimental results, they applied the model on two real cases of landslide in dam reservoirs. The model is shown to achieve high accuracy on the resolution of the non-linear effects and frequency dispersion.

However, Lynett & Liu [58] indicate that depth-integrated model becomes inaccurate when the water depth above the slide is 3.5 times less than the characteristic horizontal length of the slide. For smaller water depth, other type of models need to be employed.

1.3.3 Potential flow equations

In potential flow equations, the fluid is assumed to have an ideal motion of homogeneous stream flow without whirls or friction forces (Yavari-Ramshe & Ataie-Ashtiani [98]), nevertheless, these types of models include both dispersive and non-linear effects.

A numerical wave tank based on fully non-linear potential flow theory to simulate tsunami generation by underwater landslides has been developed in 2D by Grilli & Watts [33] and 3D by Grilli et al. [32]. The 2D model was successfully validated by Grilli & Watts [34] on experimental results with a semi-elliptical rigid slide and used for the study of parameters on wave generation and the development of predictive equations (Watts et al. [93]). The validation 3D model is also demonstrated in Enet & Grilli [21], Grilli et al. [30].

However, these equations have limitations as they are accurate for rigid submarine slides but cannot be employed for subaerial landslides where the water-slide interactions are more complex with vorticity created by flow separation or interface reconnection (Abadie et al. [2]).

1.3.4 Navier-Stokes equations

The equations that take the least hypothesis on the flow are the full Navier-Stokes equations.

Examples can be found in Heinrich [38] with a prescribed slide motion. The results are in agreement with the experiments except near the block due to the absence of turbulence model according to the authors. Liu et al. [55] also prescribed the slide motion and obtained quite good agreement with experimental results for 3D simulation of subaerial rigid slide with a Large Eddy Simulation (LES) model.

Abadie et al. [2] solved the Navier-Stokes equations and simulated 2D, 3D, submarine and subaerial cases of wave generated by rigid slide (modelled as a penalised fluid as presented in the section 1.2.1) and obtained good results on the free surface deformation. Solving Navier-Stokes equations for the slide aslo allows to describe its bulbous shape and the vortex at the front as observed in the Viroulet's experiments and achieved in their simulations using a Newtonian fluid (Viroulet [86], Viroulet et al. [88]).

The models can be separated between Eulerian and Lagrangian methods. Yim et al. [99] compared simulations of the Scott Russel wave generator for a Volume Of Fluid (VOF) model and a Smoothed Particle Hydrodynamics (SPH) model. In this case, the wave amplitude and phase were better predicted by the VOF model than the SPH model.

Navier-Stokes equations can be applied in most cases, however it is also very expensive in time and computer resources for large or complex geometries.

1.4 Pyroclastic flow wave generation and models

1.4.1 Wave generation process

According to the definition of Cas & Wright [11] pyroclastic flow is a hot, variably fluidized, gas-rich, high particle concentration mass-flow of pyroclastic debris. The pyroclastic flow has two components: a first dense, ground-hugging part (the pyroclastic debris flow) and a second less dense, more buoyant part (the plume) (Watts & Waythomas [94]).

Several processes of wave generation are involved during the entering of pyroclastic flow into a water body. They are illustrated on Figure 1.4. The possible processes are the wave generation by a steam explosion which can be produced when the hot pyroclastic flow comes into contact with water, the penetration of dense pyroclastic debris flow, plume pressure or shear on water surface. To explain how those mechanisms can or cannot generate a coherent wave, Watts & Waythomas [94] evaluated the wave amplitude they can produce. They conclude that the dense part of the pyroclastic flow is the most energetic one and dominates the tsunami generation. The other possible processes do not produce coherent and significant waves able to propagate away and affect shoreline.

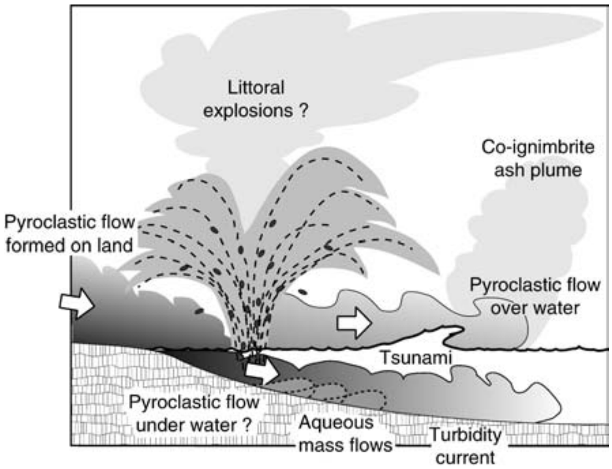

Figure 1.4: Schematic illustration of interaction scenarios where pyroclastic flows generated on land enter the sea, from Freundt [23]

1.4.2 Experimental studies

As only few observations were recorded on real events, the experiments carried out by Freundt [23] is a valuable resource to better understand the interactions between hot ($> 250°C$) and cool ($< 150°C$) pyroclastic flow and water. From this study, the pyroclastic flow enters water and generates a wave, an ash-cloud surge and a turbidity current develops. Some explosions throw ash forward that collapses and then merges with the turbidity current. At laboratory scale, it seems that the waves are mainly generated by the dense current but also by steam explosion and particles collapsing into water at low or high temperature. These experiments confirm that pyroclastic flow can generate waves whatever its temperature.

In order to model numerically the dense part of the pyroclastic flow, it is necessary to study its behaviour during motion. For Druitt et al. [16], gas retention is likely to be able to retain gas a few metres thick for a few tens to a few hundreds of seconds. In this condition, pyroclastic flows might be able to maintain low friction for a long period of time during its motion.

This theory is strengthened by Roche et al. [79] study. Comparing a water dam break to a dam break of initially fluidized dense granular flow, Roche et al. [79] observe that their propagation is very similar except in a last stage where the granular flow stops while the water flow decelerates slightly. They conclude that the pyroclastic flow can be modelled as an inertial fluid providing the flow occurs at a high shear rate. However, at lower shear rate, the behaviour is closer to dry granular flow and friction between grains has to be taken into account.

1.4.3 Numerical studies

Waythomas & Watts [96] simulated a tsunami generated by pyroclastic flow at the Aniakchak Volcano, Alaska. They computed the tsunami source using the Tsunami Open and Progressive Initial Conditions System (TOPICS) that provides tsunami sources for earthquakes, underwater slides, debris flow and pyroclastic flows (Watts, Grilli, Kirby, Fryer & Tappin [92]). TOPICS generates initial water surface elevations and velocities using curve fitting techniques (Grilli & Watts [33], Grilli & Watts [34]). This source is then used as initial condition in a Boussinesq model. Their results agree generally with the deposits recorded. The potential of far-field tsunami generation by pyroclastic flow is also demonstrated.

Maeno & Imamura [60], Maeno & Imamura [61] modelled pyroclastic flow as an inviscid flow. They tried to reproduce the tsunami generated during the Krakatau eruption of 1883 by three different sources: pyroclastic flows, phreatomagmatic explosion and caldera collapse (Maeno & Imamura [61]). Comparing their results with the estimation of wave heights from historical records, the pyroclastic flows sources appears to be the most probable source providing the better prediction.

1.5 Energy transfers between slide and waves

The study of the energy transfers between landslide and waves is an essential part of the process understanding. Before the event, the slide has a potential energy. During the motion of the landslide, this energy is part converted into kinetic energy, lost by friction or transferred to water. A part of energy transferred to water generates the waves. A few studies focused on these energy transfers for subaerial and submarine slides based on laboratory experiments or numerical simulations.

1.5.1 Slide energy computation

Potential energy released during a real event can be evaluated by knowing the initial and final positions of the slide. However, kinetic energy is more difficult to estimate as the velocity and acceleration of the slide are very seldom known. In this case, the use of laboratory experiments or numerical simulations enables to know the slide motion and to evaluate the energy released by the slide during wave generation.

For instance, Ruff [80] considers that the energy released is only the difference between potential energy before and after the event and does not take kinetic energy into account.

In other studies, only kinetic energy is computed and considered for the assessment of energy transfer from slide to waves. For example, for submarine slide, Watts [91] computes the slide kinetic energy as $E_k = \rho_s u_t^2 A$ with ρ_s the slide density, u_t the slide terminal velocity evaluated by the initial slide parameter and A the cross-sectional area. In a similar way, for subaerial slide, Fritz et al. [24] compute a kinetic slide impact energy as $E_k = \frac{1}{2} m_s v_s^2$ with m_s the slide mass and v_s the slide impact velocity depending on slide drop height, a friction coefficient and slope angle. Heller et al. [41] used sensors on a rigid slide to compute the kinetic energy.

Energy conversion from potential to kinetic energy can be evaluated from the computation of both energies. From their experiments on submarine landslides, Sue et al. [84] found that the conversion ratio increases with the initial slide acceleration (30% and 50% of conversion in their experiments) but initial submergence seems to have a low influence on this conversion.

1.5.2 Wave energy computation

Similarly, the wave field is rarely known in real events and wave heights are evaluated from records, deposits or wave gauges. This makes it even more difficult to quantify wave energy.

In laboratory experiments, wave gauges or videos give water free surface elevation. From these data, wave potential energy can be assessed. Wave kinetic energy requires more complex techniques like Particle Image Velocimetry (Heller et al. [41]) or Particle Tracking Velocimetry (Sue et al. [84]) to get the water velocity field. If kinetic energy is not known, equipartition between potential and kinetic energy is often assumed (Fritz et al. [24], Ataie-Ashtiani & Nik-Khah [5]). Fritz et al. [24] showed that this hypothesis is not correct near the impact zone. The hypothesis of equipartition is validated in linear wave theory, however it is common for landslide tsunamis to be highly non-linear and exhibit kinetic energy larger than potential energy (Heller et al. [41], Heller & Hager [42]). Heller et al. [41] computed kinetic and potential energy at probes considering that the wave crest and through travel at the same speed even if this is not completely true (Fritz et al. [24]) and estimated that this hypothesis leads to a maximum error of 10%. Sue et al. [84]) computed both energies directly on parts of the domain. Considering the repartition of energy in the wave train, Fritz et al. [24] observe that between 8 and 100% of the energy is located in the leading wave crest.

1.5.3 Evaluation of the energy transfer

The range of energy conversion rate found in literature is very broad. Furthermore, the conversion is evaluated considering different slide energy.

For instance, for subaerial slide, Fritz et al. [24] and Ataie-Ashtiani & Nik-Khah [5] evaluate the conversion of kinetic slide impact energy to the wave train between 4 and 50%.

For submarine slide, Ruff [80] estimates the transfer of slide potential energy to wave energy between 0 to 50% quantitatively from reasonable geologic and hydrodynamic parameters. From laboratory experiments, Watts [91] evaluates the energy conversion from solid block kinetic energy to water wave energy per unit width between 3 and 7%. Between 1 and 14% of energy is transferred to waves for Ataie-Ashtiani & Najafi-Jilani [4] with the same expression. For Sue et al. [84], conversion of landslide kinetic energy to wave potential energy is between 2.8% and 13.8%. In numerical simulations of Jiang & LeBlond [47], the maximum value of ratio of wave energy and slide potential energy is between 2 and 4%.

These observations highlight the parameters which control the energy transfer between slide and waves. For subaerial slide, the energy transfer decreases for increasing Froude number (Ataie-Ashtiani & Nik-Khah [5]). For submarine slide, the energy conversion increases when the initial slide submergence decreases (Ataie-Ashtiani & Najafi-Jilani [4], Sue et al. [84]).

1.6 Conclusion

Wave generation involves complex processes which must be correctly modelled. Although different numerical models of landslide and flow are avalaible, some grey areas are still present in the litterature,especially on the energy transfer from slide to water and the importance of slide parameters.

In this thesis, a model of landslide composed of several rigid blocks in a Navier-Stokes code is proposed. The originality of this model is the development of a routine inside the code which manages the collision between the blocks composed of penalised fluid (Section 1.2.1). This method enables to solve fluid/solid and solid/solid interactions without the addtion of any external code.

Then, we propose to simulate two cases of granular flow using a Newtonian fluid model and a $\mu(I)$ formulation (Section 2.5). The $\mu(I)$-rheology models dense granular flow and have not yet been found in litterature for wave generation study. Moreover, this model can help calibrate the Newtonian fluid viscosity. Additionnaly to these models, energy transfers from slide to waves is studied computing both kinetic and potential energies as only realised in a few studies. An energy conversion rate which takes viscous dissipation into account is proposed.

The last chapter deals with wave generation by pyroclastic flow. Only a few numerical studies addressed this subject. In the framework of the RAVEX project, experiments with fluidized granular beds will be carried out. In order to prepare simulations on these experiments, computations are performed on fluid/fluid experiments. This work is an overview of what is intended for the project in terms of energy transfer study and parameters influence.

CHAPTER

TWO

NUMERICAL TOOL PRESENTATION: THETIS

Contents

2.1 THETIS presentation

THETIS is a numerical model developed by the I2M Laboratory in Bordeaux. It enables to resolve various problems encompassing fluid flows, thermal transfers or porous media. The approach is Eulerian with a fixed cartesian mesh. For this chapter, only the solving of the Navier-Stokes equations that govern the incompressible flows of Newtonian fluids are presented:

$$\begin{cases} \nabla \cdot \underline{v} = 0 \\ \rho \left(\dfrac{\partial \underline{v}}{\partial t} + (\underline{v} \cdot \nabla) \underline{v} \right) + \nabla p - \nabla \cdot \left[\mu (\nabla \underline{v} + \nabla^t \underline{v}) \right] = \rho \underline{b} \end{cases} \tag{2.1}$$

One of the particularity of the code is that to propose a 1-fluid formulation (Kataoka [50]) to solve multiphase flow of immiscible fluids. In this model, in the Navier-Stokes equations one equivalent fluid intervenes whose physical characteristics, ρ and μ, vary in space and time. In order to determine the interface position between phases and the local physical properties of the flow, a function called the colour function or Volume-Of-Fluid function defines the presence rate of each phase in the cells.

2.2 Boundary conditions and obstacles

Boundary conditions at the domain limits or solid element included in the domain are treated with a method consisting in the addition of a penalty term in the momentum equation.

2.2.1 Boundary conditions

The method is only presented here for boundary conditions on velocity but it can also be applied on scalar variables like pressure. For instance, the addition of a penalty term in momentum equation is based on the work of Angot [3] and Khadra [52]. This method consists in writing the boundary conditions as surface flux directed outward the computation domain:

$$-\left(\frac{\partial \underline{v}}{\partial n} \right)_S = \underline{\underline{B_u}} (\underline{v} - \underline{v}_\infty) \tag{2.2}$$

where $\underline{\underline{B_u}}$ is a matrix whose coefficients determine the type of boundary conditions to impose. The boundary condition is a Neumann condition if the diagonal coefficients are zero and therefore the flux is null. On the contrary, if the diagonal terms are infinite, it follows $\underline{v} = \underline{v}_\infty$ and the boundary condition is a Dirichlet condition. In this case, the velocity to impose can be chosen by setting the value of $\underline{v}_\infty$. Mixed conditions can be imposed by changing the value of the matrix coefficients. For computation of waves generated by landslides, the following boundary conditions have been considered:

i. slip condition (or symmetry) which imposes a Neumann condition to the tangential component on the boundary and zero normal velocity. The fluid can only move parallel to the boundary.

ii. no-slip condition (or wall) imposing zero velocity on all the boundaries. The fluid is blocked on all directions.

Considering the penalty term, the system (2.1) becomes:

$$\begin{cases} \nabla \cdot \underline{v} = 0 \\ \rho \left(\dfrac{\partial \underline{v}}{\partial t} + (\underline{v} \cdot \nabla) \underline{v} \right) + \underline{\underline{B_u}} (\underline{v} - \underline{v}_\infty) = \rho \underline{b} - \nabla p + \nabla \cdot [\mu (\nabla \underline{v} + \nabla^t \underline{v})] \end{cases} \tag{2.3}$$

2.2.2 Obstacles

For an obstacle situated inside the computation domain, three numerical methods are possible:

i. The first method consists in penalised the velocity by using the penalty terms added in the previous subsection. By changing coefficients in the matrix $\underline{\underline{B_u}}$, it is possible to impose a velocity at points anywhere in the domain. To obtain an obstacle, it is only necessary to impose a zero velocity at the location of the intended obstacle.

ii. The second method is inspired from Brinkman theory. It consists in considering each phase as a porous media of varying permeability K. By adding a new term (Brinkman term) in momentum equation, it is possible to distinguish a fluid phase from a solid phase by varying the value of K:

$$\rho \left(\frac{\partial \underline{v}}{\partial t} + (\underline{v} \cdot \nabla) \underline{v} \right) + \underline{\underline{B_u}} (\underline{v} - \underline{v}_\infty) + \boxed{\frac{\mu \underline{v}}{K}} = \rho \underline{b} - \nabla p + \nabla \cdot [\mu (\nabla \underline{v} + \nabla^t \underline{v})] \tag{2.4}$$

For $K \to +\infty$, the Brinkman term disappears from equation (2.4) and the media is considered as fluid. For $K \to 0$, the Brinkman term becomes preponderant over the other terms of the equation. At considerated nodes, the imposed velocity is null in all directions and the media is treated as an obstacle. In practice, the values of K are set to 10^{-40} for a solid and 10^{40} for a fluid.

iii. The third method consists in considering the obstacle as a fluid of infinite viscosity. This method has been used in this work to model solid/fluid interaction and extended to solid/solid interaction. It will be detailed in Section 3.3.4.

2.3 Navier-Stokes solving method

2.3.1 Temporal discretisation

The simulations are divided into time steps Δt. These time steps are either fixed at a given value or evaluated by a dynamic Courant-Friedrichs-Levy (CFL) condition. The CFL condition controls the maximal distance travelled by a particle during one time step. The implicit temporal discretisation of equations is realised by a Euler scheme of first order (GEAR1):

$$\frac{\partial \underline{v}}{\partial t} = \frac{\underline{v}^{n+1} - \underline{v}^n}{\Delta t^n} \tag{2.5}$$

Applied to the Navier-Stokes equations (2.1), with the convective term $(v^{n+1} \cdot \nabla)v^{n+1}$ linearised as $(v^n \cdot \nabla)v^{n+1}$ to give a linear formulation of the problem, this leads to the following system:

$$\begin{cases} \nabla \cdot \underline{v}^{n+1} = 0 \\ \rho^n\left(\frac{\underline{v}^{n+1}}{\Delta t^n} + (\underline{v}^n \cdot \nabla)\underline{v}^{n+1}\right) + \underline{\underline{B_u}}(\underline{v}^{n+1} - \underline{v}_\infty) + \frac{\mu \underline{v}^{n+1}}{K} \\ \qquad + \nabla p^{n+1} - \nabla \cdot [\mu^n(\nabla \underline{v}^{n+1} + \nabla^t \underline{v}^{n+1})] - \rho^n \underline{b} = \rho^n \frac{\underline{v}^n}{\Delta t^n} \end{cases} \tag{2.6}$$

2.3.2 Spatial discretisation

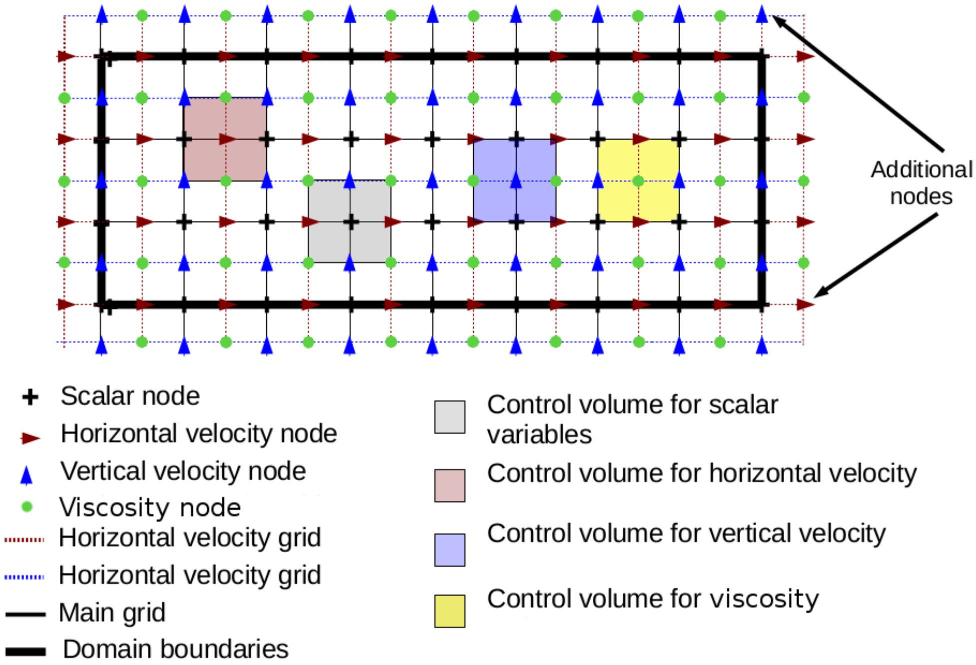

Figure 2.1: Presentation of offset grids and control volumes in THETIS

The spatial discretisation of equations uses the finite volume method. The computation domain is discretised in control volumes for each variable of the problem. The equations are integrated on these control volumes, in which each variable is supposed constant during a time step Δt. The terms of the equations are expressed by a conservative form in order to use the Stokes formula on the control volume (V_Ω):

$$\frac{1}{V_\Omega} \int_\Omega (\nabla . F)\, dv = \frac{1}{V_\Omega} \int_\Gamma F.\underline{n}\, ds \tag{2.7}$$

$$\text{with} \quad \int_\Gamma F.\mathbf{n}\, ds = \int_{\Gamma_N} F.\underline{n}_N\, ds + \int_{\Gamma_S} F.\underline{n}_S\, ds + \int_{\Gamma_E} F.\underline{n}_E\, ds + \int_{\Gamma_W} F.\underline{n}_W\, ds \tag{2.8}$$

F is the considered variable, Γ_i the interface of the volume V_Ω with the neighbour volume oriented along i (i.e. North, South, East or West) and n_i the normal to the interface Γ_i.

Patankar [71] showed that the use of offset grids between the different variables as on Figure 2.1 allows to improve the accuracy of pressure gradient and velocity divergence computation. This method is also called Marker And Cells (MAC) method (Harlow & Welch [37]).

With this method, scalar variables (pressure, density and colour function) are given on mesh nodes composing the main grid. They are evaluated by integration on control volumes centred on mesh nodes represented by a green surface on Figure 2.1. Velocity components are evaluated on offsets grids represented by red and blue surfaces on Figure 2.1. The viscosity is also evaluated on offset grid whose control volume is yellow on Figure 2.1.

2.3.3 Velocity-pressure coupling resolution

Augmented Lagrangian method

The Lagrangian Augmented method has been developed a few years ago in order to solve the velocity-pressure coupling presented by the system (2.6). The pressure term is made explicit and the problem is reformulated. The new problem consists of optimising the search of the saddle point associated to Augmented Lagrangian. The method is iterative (Uzawa algorithm) whith iterations intern to time iterations. With k iteration, the system becomes:

$$\begin{cases} \rho^n(\frac{\underline{v}^{n,k+1}}{\Delta t^n} + (\underline{v}^{n,k}\nabla)\underline{v}^{n,k+1}) + \underline{\underline{B_u}}(\underline{v}^{n,k+1} - \underline{v}_\infty) + \dfrac{\mu^n \underline{v}^{n,k+1}}{K} - \rho^n \underline{b} - \nabla p^{n,k} \\ -\nabla[\mu^n(\nabla \underline{v}^{n,k+1} + \nabla^t \underline{v}^{n,k+1})] - r_u \nabla(\nabla \cdot \underline{v}^{n,k+1}) = \rho^n \frac{\underline{v}^n}{\Delta t^n} \\ \\ p^{n,k+1} = p^{n,k} - r_p \nabla \cdot \underline{v}^{n,k+1} \end{cases} \tag{2.9}$$

with n the temporal iteration

and r_u and r_p two strictly positive convergence parameters

The algorithm convergence is reached when $(\underline{v}^{n,k+1}, p^{n,k+1}) = (\underline{v}^{n,k}, p^{n,k})$. The advantage of this method is the explicit computation of the pressure where no limit condition on its value is required.

Pressure correction

The pressure correction introduced by Chorin [13] and Goda [29] is composed of two steps:

i. From the couple ($\underline{v}^n$,p^n), a velocity field $\bar{\underline{v}}$ is computed by the following expression:

$$\bar{\underline{v}} - \underline{v}^n = \frac{\Delta t^n}{\rho^n}\Big(\rho^n \underline{b} - \nabla p^n + \nabla \cdot (\mu^n[\nabla \underline{v}^n + \nabla^t \underline{v}^n]) - \nabla \cdot (\rho^n \underline{v}^n \otimes \underline{v}^n)\Big) \tag{2.10}$$

This field satisfies the momentum equation but not the incompressibility condition.

ii. Velocity $\underline{v}$ is computed by projection of $\bar{\underline{v}}$ on a field of zero divergence:

$$\underline{v}^{n+1} = \bar{\underline{v}} - \frac{\Delta t^n}{\rho^n}\nabla(p^{n+1} - p^n) \tag{2.11}$$

The second step (projection step) imply the determination of the pressure p^{n+1}. In order to achieve that, the Poisson's equation:

$$\nabla \cdot \left(\frac{\Delta t^n}{\rho^n}\Delta(p^{n+1} - p^n)\right) = \nabla \cdot \bar{\underline{v}} \tag{2.12}$$

is implicitly solved beforehand.

2.4 Interface tracking methods

2.4.1 Volume Of Fluid method

As presented earlier, the 1-fluid model of Navier-Stokes equations requires knowing the physical properties of the equivalent fluid in the domain. In order to achieve that, the position of the interface between the phases must be determined. A colour function ϕ_{F_i} for each phase defines the volume fraction of a phase F_i in each cell, namely:

$$\begin{cases} \phi_{F_i} = 1 \quad \text{if the fluid } F_i \text{ occupies all the cell} \\ \\ \phi_{F_i} = 0 \quad \text{if the fluid } F_i \text{ is not present in the cell} \\ \\ 0 < \phi_{F_i} < 1 \quad \text{if the fluid } F_i \text{ partially occupies the cell} \end{cases} \tag{2.13}$$

The temporal evolution of the colour function during the computation is determined by solving the following advection equation:

$$\frac{\partial \phi_{F_i}}{\partial t} + \underline{v} \cdot \nabla \phi_{F_i} = 0 \tag{2.14}$$

where $\underline{v}$ is the fluid velocity. The evolution of the interface is represented by the iso-contour $\phi_{F_i} = 0.5$ and is modelled by the interface transport methods presented in the subsections 2.4.2 and 2.4.3.

Determination of physical properties The physical properties of the equivalent fluid, i.e. the density ρ and the dynamic viscosity μ, are expressed according to the colour functions ϕ_{F_i}. If the cell is occupied only by a fluid F_i, the density and dynamic viscosity are equal to those of fluid F_i. Otherwise in mixed cells, in order to take into account the weight of each present fluid, the equivalent properties are computed by an arithmetic mean even if this method can not be physically justified for the viscosity, namely:

$$\rho = \sum_i \phi_{F_i} \cdot \rho_{F_i} \tag{2.15}$$

$$\mu = \sum_i \phi_{F_i} \cdot \mu_{F_i} \tag{2.16}$$

2.4.2 VOF-TVD

The so-called TVD (Total Variation Diminishing) method consists in simply transporting the colour function by solving algebrically the advection function (2.14) using an appropriate numerical scheme. When using a classic upwind scheme, an excessive numerical diffusion is generated at the interface. However, solving the advection equation with a higher order scheme, a Lax-Wendroff scheme for instance, induces large numerical oscillations to appear at the interface. In order to avoid these problems, a TVD numerical scheme is used (Vincent & Caltagirone [85]). A TVD scheme is equivalent to a high order scheme in domain part where the solution is regular, namely where only one fluid is present, avoiding the diffusion. At the interface between fluids, where the colour is highly discontinue, the scheme is first order, limiting oscillations. In this method, the interface is not reconstructed conversly to the so-called geometrical VOF methods (see next section).

2.4.3 VOF-PLIC

The PLIC (Picewise Linear Interface Construction) method uses an interface reconstruction method into straight segments based on the colour function.

The method consists in three steps:

i. Reconstruction of the interface:

   - The segment is oriented by computed the normal directed outward. This is realised by approaching the gradient of the colour function in the neighbour cells by a 9 points finite difference. It follows:

$$\underline{n} = -\nabla\phi \tag{2.17}$$

   - The segment is positioned in the cell according to the value of the colour function in the cell.

ii. Advection of the segment by linearly interpolating the velocity components previously computed on the offset grids.

iii. Determination of the new field of colour function by computed the area ratios delimited by the new position of the segments.

Phase regularisation It may occur that the PLIC method does not allow the flow to be correctly solved and generates a cloud of drops in particular during interface reconnection. This phenomenon can be avoided by using the method SVOF (for Smooth VOF) developed by Pianet et al. [76]. The idea is to introduce a controled diffusion zone in order to smooth the interface. This smoothed colour function ϕ^S is obtained by analogy with the thermal diffusion equation:

$$\frac{\partial T}{\partial t} - \nabla a_T \nabla T = 0 \tag{2.18}$$

where a_T is the thermal diffusion coefficient and T the temperature. The characteristic length of diffusion in this case is $\delta = \sqrt{a_T \tau_d}$ where τ_d is the characteristic time of diffusion.

The function ϕ^S is built from the time discretised equation (2.18):

$$- \nabla a_T \nabla \phi^{S,n+1} + \phi^{S,n+1} = \phi^{S,n} \tag{2.19}$$

The equivalent diffusion coefficient a_T is expressed in function of the interface thickness L_i and the local cell dimensions Δh as:

$$a_T = L_i \Delta h^2 \tag{2.20}$$

This equation is then discretised in space by a finite volume method and a centred scheme. The function ϕ^S is iteratively obtained by the following algorithm:

$$L^1 = \phi \tag{2.21}$$

$$\text{For } k = 1 \ldots N-1, \text{ solve}$$

$$-\nabla.\tau_d^* \nabla \phi^{S,k+1} + \phi^{S,k+1} = L^k \tag{2.22}$$

$$L^{k+1} = \phi^{S,k+1} \tag{2.23}$$

where τ_d^* is defined by $\tau_d^* = \frac{L_i \Delta h^2}{N}$. After the solving of equations (2.21)-(2.23), the condition $\phi^S = \phi^{S,N}$ is verified.

The function ϕ^S has a thin zone of diffusion which allows to represent the interface in a more regular way. In practice, parameters L_1 and N are chosen arbitrarily in order to limit the interface splitting while keeping an accurate description of the interface.

2.5 Granular media modelling: $\mu(I)$-Rheology

In the simulations presented here, three phases are present: air, water and slide. Air and water are modelled by a classic Newtonian fluid. The slide will be modelled differently according to the cases. In order to model granular slide, two fluid models are used: Newtonian fluid and $\mu(I)$-rheology.

The $\mu(I)$-rheology has been developed to model dense granular flow. The $\mu(I)$-rheology implemented in THETIS during the thesis has the form described by Lagrée et al. [53] and implemented in the CFD software Gerris. The viscosity η, the friction coefficient $\mu(I)$ and the inertial coefficient I are defined as follows:

$$\eta = max\left(\frac{\mu(I)}{\sqrt{2}D_2} p, 0\right) \tag{2.24}$$

$$\mu(I) = \mu_s + \frac{\Delta\mu}{I_0/I + 1} \tag{2.25}$$

$$I = \frac{d\sqrt{2}D_2}{\sqrt{|p|/\rho}} \tag{2.26}$$

with

- D_2 the second invariant of the strain rate tensor
- p the pressure
- μ_s, $\Delta\mu$ and I_0 three material-dependent coefficients
- d the diameter of the grain
- ρ the density of the grain

This rheology has been developed for dry granular flow. In the case of granular flow in a viscous fluid, Cassar et al. [12] distinguished different regimes and adapted the expression of the inertial coefficient depending on of the regime. Three regimes are classified according to the values of two dimensionless numbers, the Stokes number St and the density ratio r:

$$St = \left(\frac{2}{3}\right)^{1/2} \frac{\alpha_p d \sqrt{\rho_p P_g}}{\eta_f} \tag{2.27}$$

$$r = \sqrt{\frac{\rho_p}{\rho_f C_d}} \tag{2.28}$$

with

- α_p a coefficient depending on the permeability of the porous medium
- ρ_p the density of the grain
- P_g the confining pressure
- η_f the kinematic viscosity of the fluid
- ρ_f the density of the fluid
- C_d the drag coefficient

The following scheme shows the regime in a (St, r) plane:

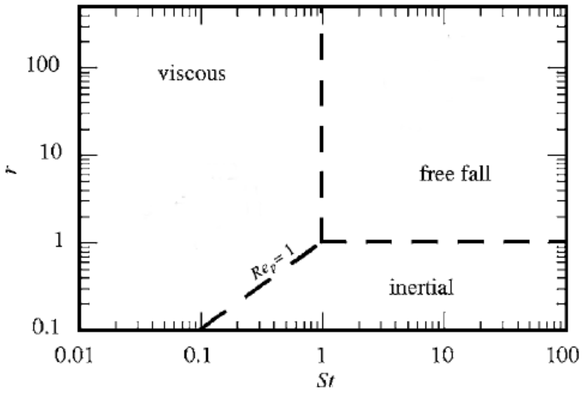

Figure 2.2: Different flow regimes in (St, r) plane based on the fall of one grain, from Cassar et al. [12] and [17]

The inertial coefficients for the different regimes are:

- Free-fall regime for $St \gg 1$ and $r \gg 1$:

$$I_{ff} = \dot{\gamma} d \sqrt{\frac{2\rho_p}{3P_g}} \tag{2.29}$$

- Viscous regime for $St \ll 1$ and $r \gg St$:

$$I_v = \frac{\dot{\gamma}\eta_f}{\alpha P_g} \tag{2.30}$$

- Inertial regime for $St \gg r$ and $r \ll 1$:

$$I_i = \dot{\gamma} d \sqrt{\frac{2\rho_f C_d}{3P_g}} \tag{2.31}$$

Cassar et al. [12] showed that the friction coefficient followed the same curve for both free-fall and viscous regime, the inertial regime having not been experimented.

2.5.1 Validation simulation

Case

The model implemented in THETIS had to be validated. The validation case chosen is a 2D granular column collapse. The data were obtained from discrete simulation (Lagrée et al. [53]), and also used for the validation of the $\mu(I)$-rheology implemented in Gerris. The column has an aspect ratio $a = 6.26$. The parameters of the rheology are set to $\mu_s = 0.32$, $\Delta\mu = 0.28$ and $I_0 = 0.4$ in Gerris simulation. The data are dimensionless, in particular time is adimensionalised by $\sqrt{H_0/g}$. The viscosity in the fluid column is computed at each time step and then the Navier-Stokes equations are solved.

Results

A comparison between the discrete and the continuum models is made at several times of the computation on Figure 2.3. The results from THETIS reproduced accurately the discrete simulation data at all time steps except for the last one where THETIS simulation shows a more flattened media at the middle and thicker on the sides.

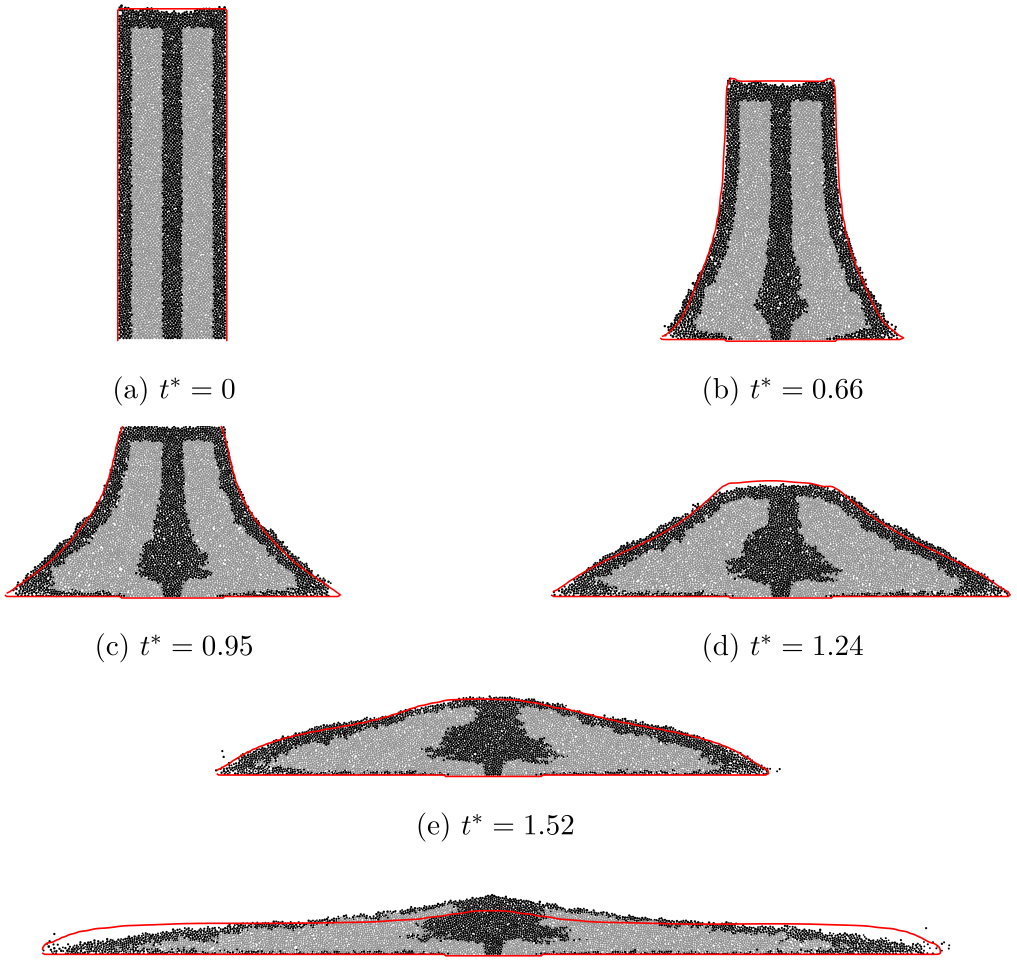

(a) $t^* = 0$

(b) $t^* = 0.66$

(c) $t^* = 0.95$

(d) $t^* = 1.24$

(e) $t^* = 1.52$

(f) $t^* = 2.28$

Figure 2.3: Comparison between continuum (THETIS, red line) and discrete (from Lagrée et al. [53], grey and black points) models for the granular column collapse

CHAPTER

THREE

DEBRIS AVALANCHE: A DISCONTINUOUS APPROACH

Contents

3.1 Principle

A landslide is composed of grains in a very broad size range from decametres to particles much smaller than micrometres (Davies & McSaveney [14]) due to the fragmentation of the slide. This phenomenon makes landslides difficult to model as a discontinuous media composed of solid blocks. Moreover, the landslides are observed to have great mobility and to travel in a manner similar to fluids (Legros [54]). For this reason, most of the studies quoted in the Chapter 1 model the slide as a fluid.

However, the fluid model does not take into account the behaviour of solid blocks. The exception is the $\mu(I)$-rheology which models the interactions between grains (GDR MiDi [28]) but it does not solve all the problems caused by fluid modelling as presented in Chapter 4. For the modelling of wave generation by landslides, the slide can be modelled as a set of solid spheres but this generally imposes a coupling between a CFD code and an external code solving the solid/solid interactions, for example a CFD-DEM coupling (Zhao et al. [100]).

The approach presented herein consists in using only a CFD code to solve both the solid/fluid and solid/solid interactions. The slide is modelled as a set of discs in a 2D domain (Figure 3.1). The discs consist of penalised fluid based on the method presented in Section 3.3.4 and described in Ducassou et al. [19]. The discs behave as solid except that because of their high viscosity and the specificity of the VOF method, they merge when they collide mimicking a perfectly plastic shock. For this reason, a Fortran routine has been developed in the code THETIS in order to manage the collisions between the discs during the simulation.

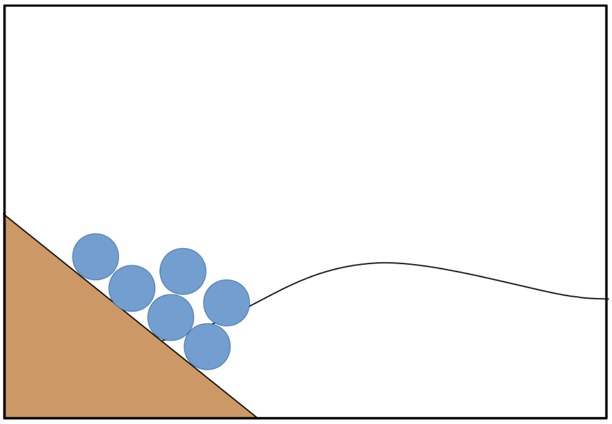

Figure 3.1: Generation of wave by a landslide modelled as a set of discs

The routine works as follows:

- a first function predicts the possible collisions between the discs by first detecting the neighbour discs and then evaluating their possible collision using their velocities and relative distance. The method is presented in the first section.
- after the detection of collision, a function computes the time of the collisions and the velocity of the discs after the impact. The trajectory of the disc is then managed by the routine. The second section presents this model.

Two validation cases are carried out and presented in the third section.

3.2 Collision detection

3.2.1 Neighbour disc detection

The neighbour disc detection is mainly inspired by methods used in DEM. In the latter, simulations involve a large number of bodies and therefore numerous impacts can happen at each time step. Therefore, algorithms for contact detection of bodies of different shapes and sizes have been developed (Munjiza & Andrews [68], Perkins & Williams [74], G. Nezami et al. [27], Mio et al. [64]). For the routine developed here, the aim is to manage a reasonable number of discs (less than 20). Therefore, the algorithm has not been optimised and may not be efficient for a larger number of discs. Moreover, the only geometry considered is a disc which facilitates the resolution as only one contact point is possible between two discs.

In the litterature, algorithms of contact detection are divided in two categories: the space-based search and the body-based search (Munjiza & Andrews [68]). The two approaches have been adapted in THETIS.

Disc identification array

For N_D discs in the simulation, they are all assigned an identification number i in $\{1, 2, \ldots, N_D\}$, a radius r_i, a centre C_i of coordinates $\underline{X_i}$ and velocity $\underline{V_i}$, and a mass m_i.

The space-based method uses one or several grids to divide the space. The advantage of THETIS is that the space is already partitioned by the mesh. Therefore, the grid can be used for neighbour detection.

At each time step, the position of the disc centres are computed using the coordinates of the centre at the previous time step and its velocity. An array `DiscID` of the size of the pressure grid is created. For each pressure point P, its distance to the centres of the discs is computed. If the distance if less than the radius of the disc i, the array value corresponding to the index of pressure point P is set to i.

An example is given in Figure 3.2. Two discs 1,2 whose centres are respectively C_1 and C_2 have the same radius R. The grid represented here is coarser than the real mesh for clarity sake. The distances between the pressure point P and the centres C_1 and C_2 are d_1 and d_2 respectively. d_1 is greater than the radius R while the distance d_2 is less than R. Therefore, the array value corresponding to P is set to 2, the identification number of the disc present at the pressure point P.

This array allows to locate the entire disc in space and not only its centre.

Neighbour detection using the cell array

In the same way as the conventional cell model (Mio et al. [64]), the neighbour points of the pressure points belonging to a disc are tested for the presence of disc. This is

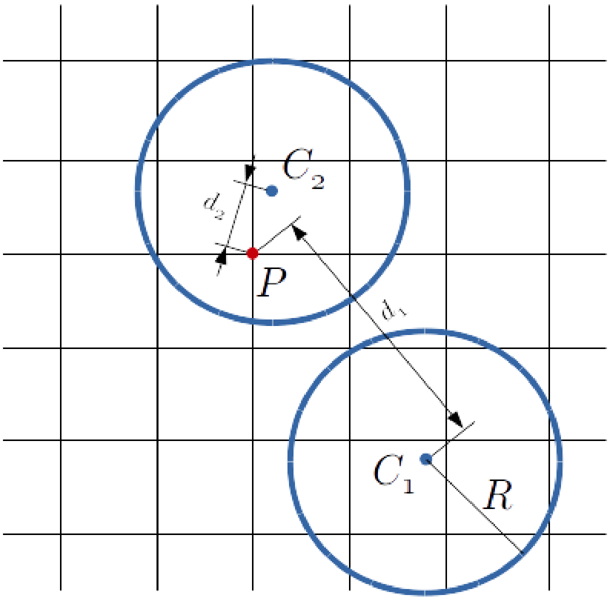

Figure 3.2: Computation of the distances between a pressure point and the disc centres

realised thanks to the disc identification array `DiscID`. The presence of disc neighbouring a pressure point could have been achieved using the colour function. However, all the discs are the same fluid, therefore they have the same colour and the routine is unable to know to which disc the pressure point belongs in contrast to using the disc identification array. The size of the neighbour zone can be then adjusted by controlling the number of cells in all directions.

For instance, on the Figure 3.3, the size of the zone is one cell in each direction. The point P belongs to the disc 2, one neighbour is detected as the south-east neighbour pressure point belongs to the disc 1.

Neighbour detection using the distance to the centre

The previous method is dependent on the cell size. By relying more on a body-based search, a second method is developed by looking for neighbour in an annulus zone around the disc whose size is independent of the mesh size. The zone has for centre the centre of the disc C_i, and has an inner and outer radius equal to the disc radius r_i and $r_i + \delta$ ($\delta > 0$) respectively. In a similar way to the previous method, the distance between the pressure points and the centres of the discs is computed. If the pressure point is located in the neighbouring zone of a disc i, the value in the array `DiscID` is read. If this value corresponds to a disc j, this disc is considered to be a neighbour of the disc i.

For instance, on the Figure 3.4, the disc 1 is considered a neighbour of the disc 2 because the point P is at a distance lower than $R + \delta$ from C_1 and belongs to the disc 2.

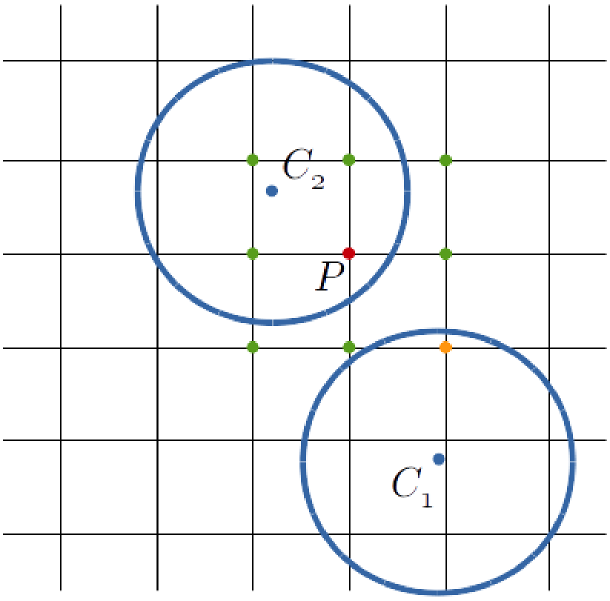

Figure 3.3: Neighbour disc detection using the array `DiscID`: one neighbour detected at the orange point

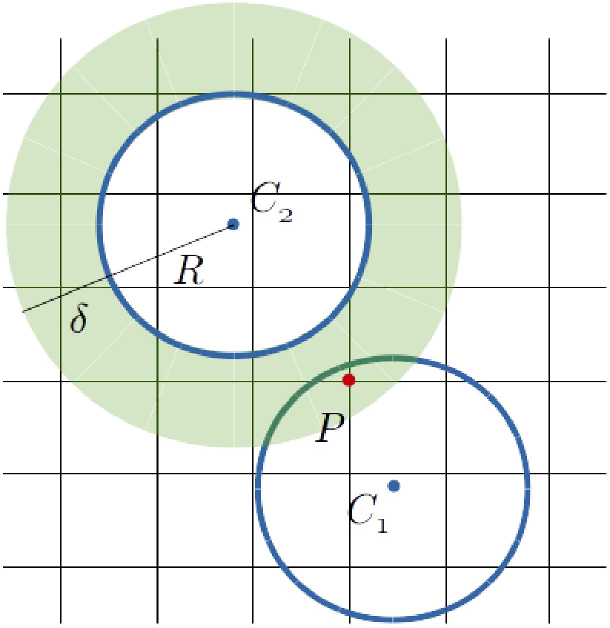

Figure 3.4: Neighbour disc detection using the distance to the centre

3.2.2 Collision test

The previous methods generate list of neighbours. We now have to dtermine whether they are likely to collide or not. A routine has been developed to test the collision between two neighbours. If the test is positive, namely they are going to collide, this routine predicts the time and distance to the collision.

The distance vector between the two centres is as follows:

$$\underline{d_{ij}} = \underline{X_j}(0) - \underline{X_i}(0) + (\underline{V_j} + \underline{V_i})t \tag{3.1}$$

Two discs collide if the distance between their centres is the sum of the two radii, namely if $\underline{d_{ij}} \cdot \underline{d_{ij}} = (r_i + r_j)^2$. Using the equation (3.1), it leads to the resolution of a quadratic equation:

$$\begin{aligned} & at^2 + 2bt + c = 0 \\ \text{with} \quad & a = (V_{ix} - V_{jx})^2 + (V_{iy} + V_{jy})^2 \\ & b = (X_{jx} - X_{ix})(V_{jx} - V_{ix}) + (X_{jy} - X_{iy})(V_{jy} - V_{iy}) \\ & c = (X_{jx} - X_{ix})^2 + (X_{jy} - X_{jy})^2 - (r_i + r_j)^2 \end{aligned} \tag{3.2}$$

The reduced discriminant $\Delta = b^2 - ac$ is calculated. Depending on its value, several cases are distinguished:

- $\Delta < 0$: there is no real solution, hence no collision
- $\Delta \geq 0$: there are one or two real solutions: $t_1 = \frac{-b-\sqrt{\Delta}}{a}$ and $t_2 = \frac{-b+\sqrt{\Delta}}{a}$
    - if $t_1 < 0$ and/or $t_2 < 0$: there is no collision
    - if $t_1 > 0$ and $t_2 > 0$: *there is a collision at time* $t_c = \min(t_1, t_2)$

3.2.3 Groups of collision

The collision test gives pairs of discs (i, j) that will collide at the time and distance computed by the function. The next step is to compute the disc velocity after the collision. This is done by solving a system on groups of discs involved in a collision. For now, only pairs of discs are defined by the collision test. However, it is likely that the collisions are quasi-simultaneous between more than two discs. For this reason, a criteria on time is added to decide whether the collisions are simultaneous or not. Based on this criteria, the groups of collision are created, i.e. the pairs of discs which are going to collide in a time lower than τ are merged in one group if they have one disc in common.

For example, if the initial collision pairs are (i, j), (k, l), (i, m) and (m, n), considering they all collide under a time τ, the final groups of collision are (i, j, m, n) and (k, l). The time τ is for now arbitrarily chosen.

3.3 Model the collision

It is recalled that the objective of the routine is to avoid the collision and the merging of the penalised discs while keeping their physical trajectories. In order to do this, the routine only manages the trajectories of the discs during a few time steps around the collision time.

This section presents the collision model that first computes the velocity of the discs after the impact and second manages the discs accordingly. Moreover, the chosen model is very simple in order to give an idea of the practicality of a solid/solid interaction model using only THETIS. To begin with, the model for the velocity computation is introduced for two discs and then extended for a larger number N.

The velocities of a disc i before and after the collision are respectively $\underline{V_i^-}$ and $\underline{V_i^+}$.

3.3.1 Collision between two discs

The impact between two discs 1 and 2 leads to four unknows, namely the components of the velocities after the impact $\underline{V_1^+}$ and $\underline{V_2^+}$.

For this simple model, the assumptions are that following: the momentum is conserved, there is no friction between two discs and a Newton's restitution law is considered for the normal impact velocity.

Momentum conservation

The momentum is conserved in the system composed by both discs leading to two equations:

$$m_1(\underline{V_1^+} - \underline{V_1^-}) = \underline{p_{12}} \tag{3.3}$$

$$m_2(\underline{V_2^+} - \underline{V_2^-}) = -\underline{p_{12}} \tag{3.4}$$

$$\text{with} \quad \underline{p_{12}} \quad \text{the exchanged momentum.}$$

The sum of these equations leads to one vectorial equation, namely two scalar equations:

$$m_1\underline{V_1^+} + m_2\underline{V_2^+} = m_1\underline{V_1^-} + m_2\underline{V_2^-} \tag{3.5}$$

No friction

As no friction is considered, the force due to the impact is collinear to the normal of the contact point leading to the following scalar equation:

$$(\underline{V_1^+} - \underline{V_1^-}) \cdot \underline{T} = 0 \tag{3.6}$$

$$\text{with} \quad \underline{T} \quad \text{a vector tangent to the contact point}$$

Newton's restitution law

The Newton's restitution law directly links the velocities normal to the contact point while the second well known model based on the Poisson's hypothesis, prescribes the normal forces. The choice of this model can lead to a violation of energy principle, however it works in most of the cases (Wang & Mason [89]).

This leads to the last equation given by the Newton's restitution law:

$$(\underline{V_1^+} - \underline{V_2^+}) \cdot \underline{N} = -e(\underline{V_1^-} - \underline{V_2^-}) \cdot \underline{N} \tag{3.7}$$

with e the restitution coefficient

and N a normal vector at the contact point

The coefficient of restitution e has values between 0 and 1 where values 0 and 1 respectively represent an impact perfectly plastic and perfectly elastic.

Solving the equation system

The equation system is:

$$\begin{cases} m_1 V_{1x}^+ + m_2 V_{2x}^+ = m_1 V_{1x}^- + m_2 V_{2x}^- \\ m_1 V_{1y}^+ + m_2 V_{2y}^+ = m_1 V_{1y}^- + m_2 V_{2y}^- \\ V_{1x}^+ T_x + V_{1y}^+ T_y = \underline{V_1^-} \cdot \underline{T} \\ V_{1x}^+ N_x + V_{1y}^+ N_y - V_{2x}^+ N_x - V_{2y}^+ N_y = -e(\underline{V_1^-} - \underline{V_2^-}) \cdot \underline{N} \end{cases} \tag{3.8}$$

This linear system can be written in a matrix way $AU = B$ with:

$$A = \begin{pmatrix} m_1 & 0 & m_2 & 0 \\ 0 & m_1 & 0 & m_2 \\ T_x & T_y & 0 & 0 \\ N_x & N_y & -N_x & -N_y \end{pmatrix} \tag{3.9}$$

$$U = \begin{pmatrix} V_{1x}^+ \\ V_{1y}^+ \\ V_{2x}^+ \\ V_{2y}^+ \end{pmatrix} \tag{3.10}$$

$$B = \begin{pmatrix} m_1 V_{1x}^- + m_2 V_{2x}^- \\ m_1 V_{1y}^- + m_2 V_{2y}^- \\ \underline{V_1^-} \cdot \underline{T} \\ -e(\underline{V_1^-} - \underline{V_2^-}) \cdot \underline{N} \end{pmatrix} \tag{3.11}$$

This system can easily be solved using a Gaussian elimination.

3.3.2 Collision between N discs

The same assumptions are taken in the case with N discs as in the case of 2 discs. Hence, it leads to a similar set of equations. In contrast to the previous case, a disc i receives an impulse p_{ij} from each disc j with which it is in contact. Therefore, there is one impulse by pairs of discs (defined by a positive collision test) present in the group of collision (using the example of the section 3.2.3, it is the pairs (i, j), (k, l), (i, m) in the collision group (i, j, m, n)).

In the equation system, the unknowns are the impulses and the velocities. Thus, if N is the number of discs in collision and N_p is the number of pairs in collision, the unknowns are N discs velocity components and N_p impulses.

Momentum conservation

A disc i receives an impulse from each disc with which it collides, namely all the discs j in pair with it. This set of pairs is named $P(i)$ leading to the following vectorial equations.

$$m_i(\underline{V_i^+} - \underline{V_i^-}) = \sum_{j \in P(i)} \underline{p_{ij}} \tag{3.12}$$

To ensure momentum conservation, we have:

$$\underline{p_{ij}} = -\underline{p_{ji}} \tag{3.13}$$

No friction

There is no friction at the contact point, so the impulse has no tangential component. Hence the following equation:

$$\begin{aligned} &\underline{p_{ij}} \cdot \underline{T_{ij}} = 0 \\ &\quad \text{with} \quad \underline{T} \quad \text{a vector tangent to the contact point between the disc } i \text{ and } j \end{aligned} \tag{3.14}$$

Newton's law of restitution

In the same way as for two discs, the Newton's coefficient of restitution is used.

$$\begin{aligned} &(\underline{V_i^+} - \underline{V_j^+}) \cdot \underline{N_{ij}} = -e(\underline{V_i^-} - \underline{V_j^-}) \cdot \underline{N_{ij}} \\ &\qquad \text{with} \quad e \quad \text{the restitution coefficient} \\ &\qquad \text{and} \quad N \quad \text{a normal vector at the contact point between the disc } i \text{ and } j \end{aligned} \tag{3.15}$$

Equation system

$$\begin{cases} m_i V_{ix}^+ - \sum\limits_{j \in P(i)} p_{ijx} = m_i V_{ix}^- \\ m_i V_{iy}^+ - \sum\limits_{j \in P(i)} p_{ijy} = m_i V_{iy}^- \\ p_{ij} T_{ijx} + p_{ijy} T_{ijy} = 0 \\ (V_{ix}^+ - V_{jx}^+) N_x + (V_{iy}^+ - V_{jy}^+) N_y = -e[(V_{ix}^- - V_{jx}^-) N_x + (V_{iy}^- - V_{jy}^-) N_y] \end{cases} \tag{3.16}$$

The first two equations are for each disc, namely N equations, the last two equations are for each pair, namely N_p equations. As in the previous case with two discs, the system is solved using a Gaussian elimination.

3.3.3 Manage the discs

Now that the time of collision and the velocities after the impact are known, the routine has to manage the discs in order to impose the correct trajectories while avoiding the collisions. After some tests with penalised discs, it has been established that two discs merge if they are at a distance lower than two cells. Thus, the routine manages the discs if the collision test is positive and they reach the critical distance of two cells.

In order to avoid the collision, a transitional velocity V_{ti} for a disc i is introduced. This velocity is computed based on the initial position of the disc and the final position where the disc resumes its correct trajectory. The time and coordinates of the final position relatively to the initial position can be known thanks to the previous computation of the time of collision and the velocity after the impact.

The trajectory imposed by the routine is illustrated by the Figure 3.5. The routine has predicted that the disc i collides at the collision point P_c and the velocity V_i^+ is computed. Knowing the collision time t_c, the velocities V_i^- and V_i^+, the position of a point C_i^+ in the theoretical course of the disc i after the impact can be predicted as well as the time it is reached. Therefore, the trajectory of the disc i is diverted from C_i^- to C_i^+ directly. During the diversion, the transitional velocity is imposed on the disc i. As soon as the disc reaches the point C_i^+, its theoretical velocity after impact V_i^+ is imposed and the disc is no longer managed by the routine (i.e. its velocity is back again obtained by solving the Navier-Stokes equations).

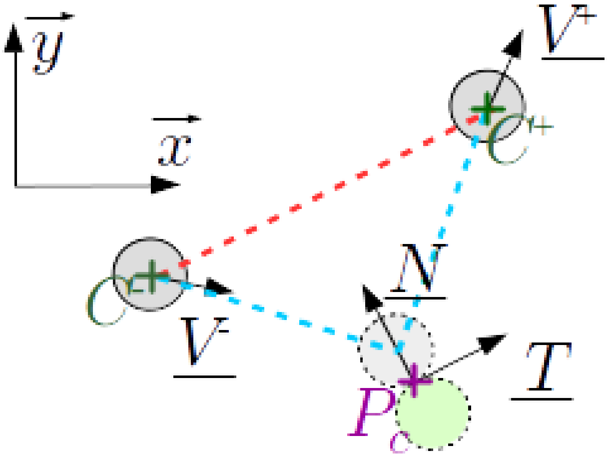

Figure 3.5: Trajectories of the disc between its position before (centre C^-, velocity V^-) and after (centre C^-, velocity V^-) the collision: theoretical in *blue*, simulated in *red*, $\underline{N}$ and $\underline{T}$ are normal and tangential vectors to the collision point P_c.

The distance from the point C_i^- to the position at impact is defined as d_c. The point C_i^+, to which the disc is diverted, is defined to be at a distance d_c from the impact position. Hence, the theoretical time of travel from C_i^- to C_i^+ is $t_c + \frac{d_c}{V_i^+}$ and the vectorial distance from C_i^- to C_i^+ is $t_c\underline{V_i^-} + \frac{d}{V_i^+}\underline{V_i^+}$. It leads to the expression of the transitional velocity V_t

to apply on the disc during the diversion from C_i^- to C_i^+:

$$\underline{V_t} = \frac{t_c \underline{V^-} + \frac{d_c}{V^+} \underline{V^+}}{t_c + \frac{d_c}{V^+}} \tag{3.17}$$

3.3.4 Solid modelling: penalty method

Principle

In this section, the landslide is composed by a set of solids for which displacement is computed by THETIS. In section 2.2, three methods have been presented to silumate solid obstacles inside the computation domain. Among these methods, the velocity penalty method or the use of the Brinkman term do not permit the obstacle to move freely because the location of the solid is imposed by the user. The third method, namely the viscosity penalty method, that consists in creating a phase with infinite viscosity, is used here and adapted to our needs.

In the momentum equation (2.4), the local deformation term $\nabla \underline{v} + \nabla^t \underline{v}$ is in factor of the dynamic viscosity μ. By making this viscosity tends to infinity, the only solution is for the local deformation term to be null. For this reason, the fluid phase with an infinite viscosity behaves as a solid. In practice, an infinite viscosity is not possible and viscosity is set to a very high value. This value has been setup by Ducassou [18] by studying the deformation of the penalised fluid as a function of viscosity. It was remarked that the computation time increases with the viscosity. As a compromise between deformation and computation time, the viscosity value of 5.10^7 $Pa.s$ has been chosen by Ducassou [18]. If not otherwise specified, this value is set as viscosity value of penalised fluid in simulations presented in this work.

Kinematic data

For the discontinuous method, some kinematic data have to be known to compute the interaction between solid blocks. The solid blocks are so far only discs, they are referred as such hereafter.

Velocity The velocity of the disc is computed by averaging the velocity in each point of penalised fluid in the disc defined by the radius R and its known centre.

Position The initial position of the gravity centre is known. After getting the velocity, the new position can be computed as follows:

$$\begin{cases} \underline{X}(0) = \underline{X}_0 \\ \underline{X}(t_{n+1}) = \underline{X}(t_n) + \underline{V}(t_n)dt \end{cases} \tag{3.18}$$

Acceleration The acceleration is approximated using the velocities of the current and previous times :

$$\underline{a}(t_n) = \frac{\underline{V}(t_n) - \underline{V}(t_{n-1})}{t_n - t_{n-1}} \tag{3.19}$$

Controlling the velocity It is possible to control the velocity of the disc by changing the acceleration in the disc. When it is needed to change the velocity of the disc (discussed in the last part of the report), the gravitational acceleration is replaced for a few time steps only by the following acceleration.

$$\underline{g} = \frac{\underline{V}_{target} - \underline{V}_{current}}{\delta t} \tag{3.20}$$

3.3.5 Comparison with a python routine

To ensure the resolution of the velocities after the collision by the routine in THETIS, simulations are performed with two discs. The positioning of the discs is shown on the Figure 3.6. The two discs have the same radius $R = 0.1\,m$. The disc D_1 is accelerated to a velocity $\underline{V_1} = V_1^- \underline{x}$ with $V_1^- = 1\,m.s^{-1}$, the velocity of the disc D_2 is null. The distance x is fixed for all computations to $0.5\,m$ and the distance y varies from 0 to $2R$. Velocities results after the collision computed by the subroutine and compared with the ones computed with the python routine can be found on Figure 3.7. All velocities computed and imposed by the routine are in agreement with the values computed by the python routine.

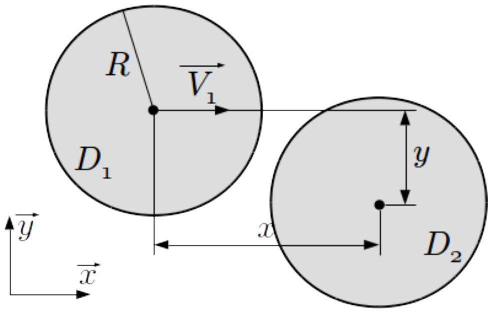

Figure 3.6: Sketch of the simulation

3.4 Validation cases

3.4.1 Floating cylinder

The first simulation case is an oscillating floating cylinder. Only the interaction solid/fluid is validated here.

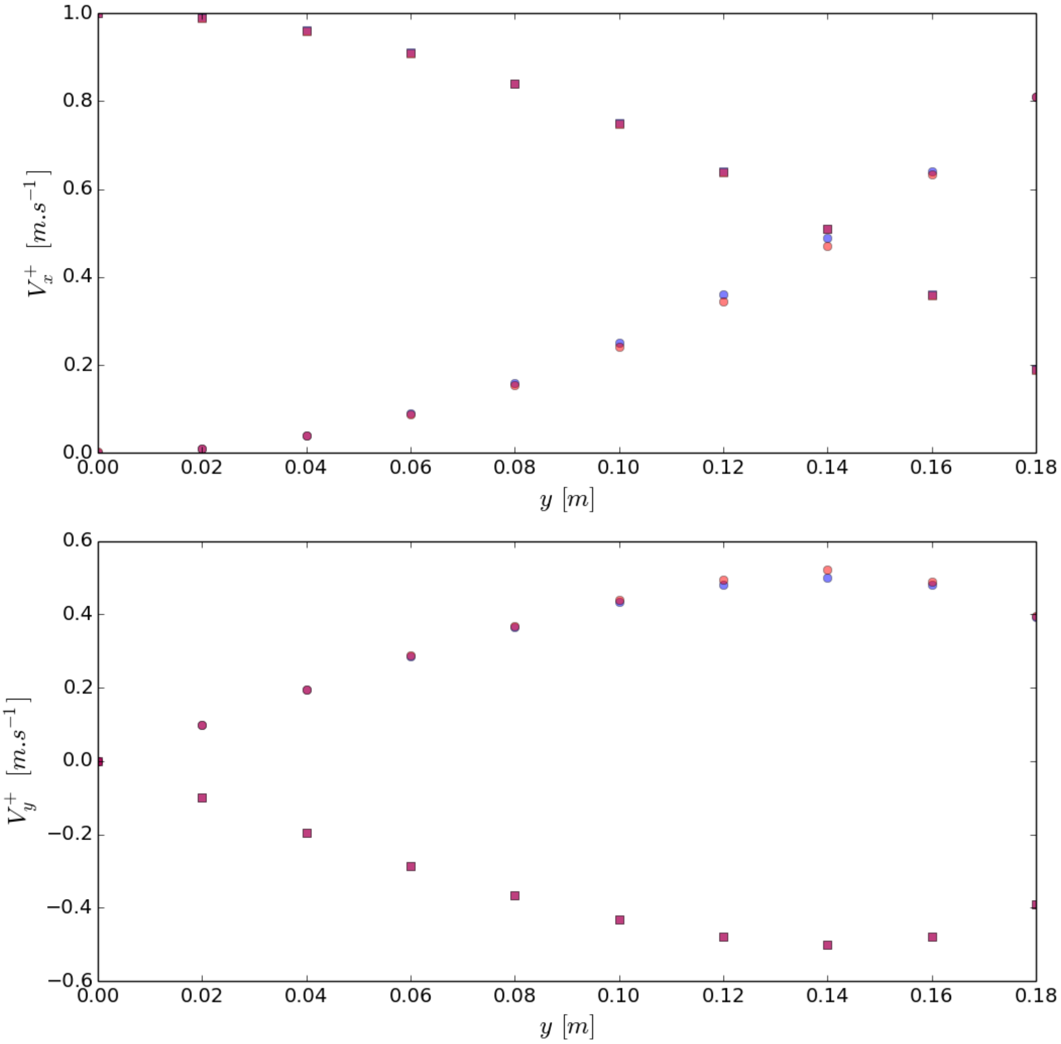

Figure 3.7: Comparison of the velocities after the collision computed by the python routine and Thetis simulation. In blue: analytical results, in red: thetis results; circle: disc D_1, square: disc D_2

Set-up

Following the experiments of Itō [45], the cylinder is initially displaced along the y axis of a distance $y_{ini} = R/3$ (Figure 3.8). The simulation is 2D and the radius R of the cylinder is fixed to the value of the experiment, namely $R = 0.0762\,m$. The water depth is also defined based on the experiment (i.e. $1.2192\,m$). The density of the cylinder is chosen in order to have an equilibrium position where the centre of the disc is at the level of the water surface at rest, namely $y = 0$. Three meshes are considered with $\Delta x = \Delta y$ near the cylinder (Figure 3.9). The time step is fixed according to the space resolution. The space and time resolution are summarised in the following table:

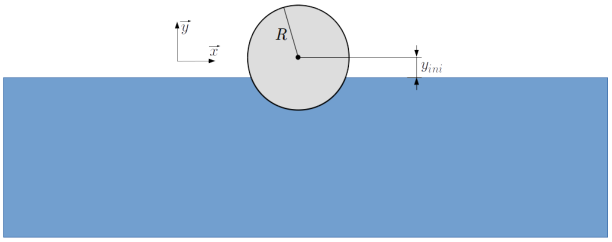

Figure 3.8: Sketch of the floating cylinder simulation

	$\Delta x\,(m)$	$\Delta t\,(s)$
mesh 1	0.004	0.001
mesh 2	0.002	0.0005
mesh 3	0.001	0.00025

Table 3.1: Simulations space and time resolutions

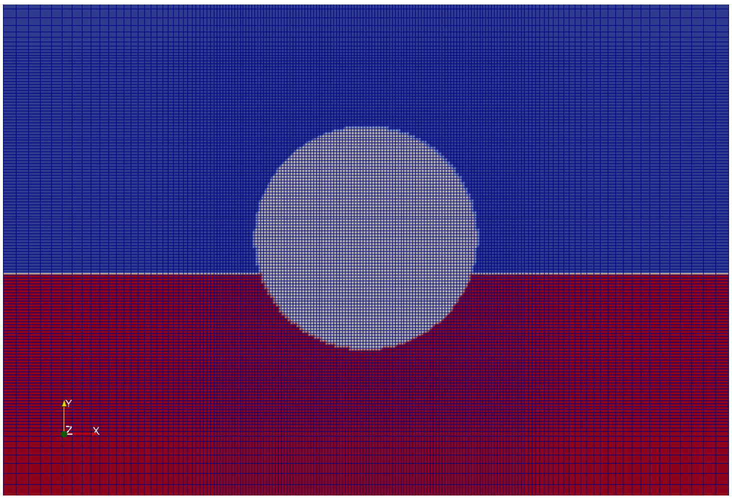

Figure 3.9: Mesh 2 of oscillating cylinder simulations, water in red, air in blue and penalised fluid in grey

Viscosity computation in mixed cells Using the equivalent viscosity in Navier-Stokes with an arithmetic mean as presented in subsection 2.4.1 in the presence of fluid with very high viscosity, can generate problems at the interface and particularly at triple points (Ducassou [18]). By computing the arithmetic mean between a small viscosity ($1.85e^{-5}\,Pa.s$ or $1e^{-3}\,Pa.s$ for air and water respectively) and a high viscosity ($5e^{7}\,Pa.s$) in mixed cells, the equivalent viscosity increases quickly as it can be seen on Figure 3.10

and all mixed cells have high viscosity. Therefore their deformation is highly reduced and this phenomenon is not physical. THETIS proposes other methods of averaging: harmonic, geometric and discontinuous mean. The distribution of viscosity computed by harmonic and geometric mean is illustrated on Figure 3.10. With these two methods, the equivalent viscosity in mixed cells where the colour function of penalised fluid ϕ_{PF} is lower than 0.5 is low enough for a fluid to flow ($< 10^2\, Pa.s$). However, for $\phi_{PF} > 0.5$, the viscosity is still low enough for the penalised fluid to flow as observed by Ducassou [18]. The discontinuous mean consists in setting the viscosity in mixed cell to the value of the fluid the most present in the cell. Same problems as with harmonic and geometric means appear and the penalised fluid can deform, particularly in shear zones (Ducassou [18]). In the case studied here, velocities are low enough for this problem not to appear and the discontinuous mean is chosen.

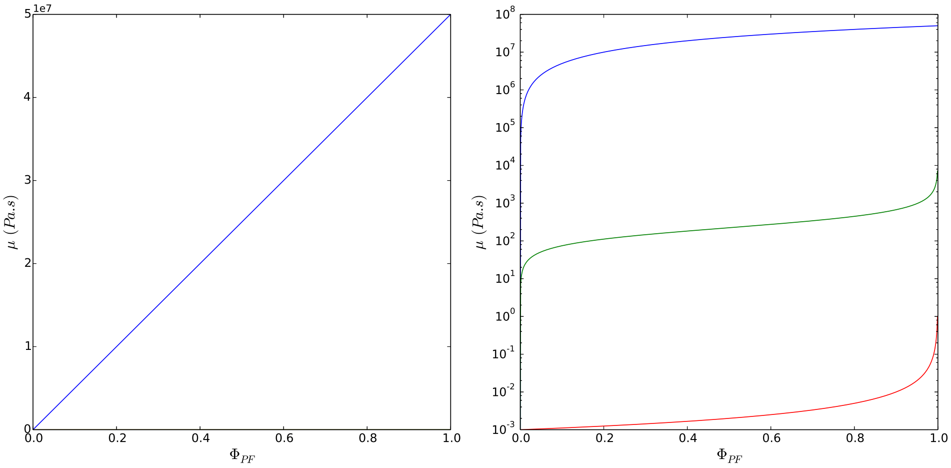

Figure 3.10: Example of computation of equivalent viscosity μ as a function of the colour function of penalised fluid ϕ_{PF} using three methods: arithmetic mean in blue, harmonic mean in red and geometric mean in green

Results

In addition to experimental results from Itō [45], the oscillations of the cylinder from THETIS simulations can also be compared with analytical results computed by Maskell & Ursell [62]. The analytical model assumes no viscosity and no surface tension.

The cylinder has first a damped harmonic oscillatory motion (Maskell & Ursell [62]). These oscillations are observed in the simulations and the amplitudes are compared with experimental and analytical results on Figure 3.11. The Table 3.2 summarises the first two peaks and troughs amplitude and time. Analytical results have greater oscillations amplitude than experimental ones (Figure 3.11 and Table 3.2), probably because the viscosity damping is not taken into account by Maskell & Ursell [62], but the oscillations are in phase. For the simulations, except for the first trough where all meshes give similar amplitudes, the mesh 1 gives slightly lower amplitudes than mesh 2 and 3. The very two give very close amplitudes and are in agreement with the experimental results. In term of oscillation phase, the thinner the mesh, the closer the amplitudes are to the experimental results.

The mass loss of penalised fluid has been evaluated on Figure 3.11. During the simulation, the maximum surface loss is of about 1% for the coarser mesh. The thinner the mesh, the less loss is observed. This is explained by the reduction of mixed cell surface with the size of the mesh inducing therefore less problems with equivalent viscosity. It can also be remarked that in THETIS, the geometry follows the mesh grid. For this reason, the disc is not completely circular (Figure 3.9). However, comparing THETIS simulations with OpenFOAM simulations carried out by Monroy et al. [66] using the same initial cylinder position, meshes and time steps but with a solid cylinder and a mesh adjusted to the cylinder, results are quite similar with for example an error of 5% and 4.3% with the mesh 3 for OpenFOAM and THETIS respectively on the first trough amplitude.

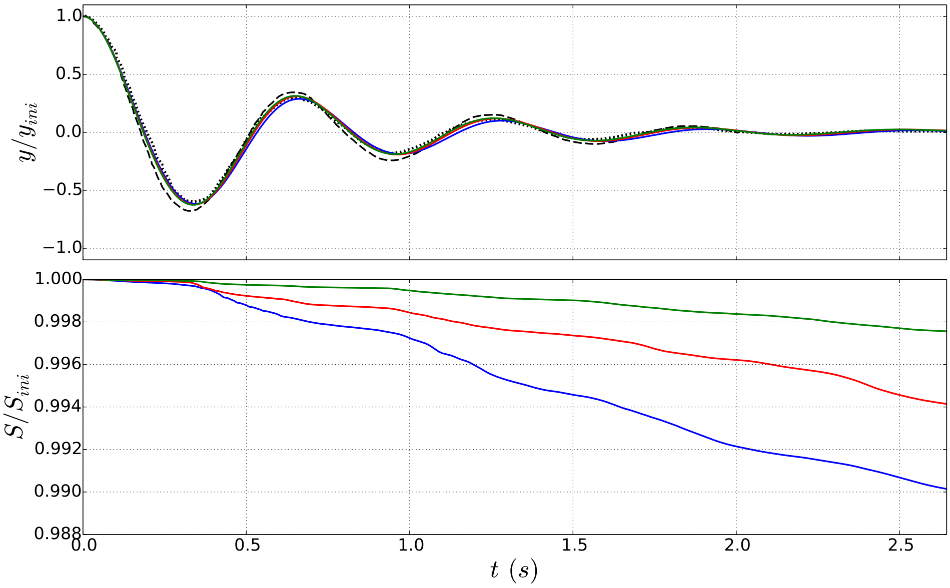

Figure 3.11: Vertical movement of the cylinder: comparison between three meshes (mesh 1 in blue, mesh 2 in red, mesh 3 in green), experimental results from Itō [45] in black dotted line and analytical results from Maskell & Ursell [62] in black dashed line (top). Evolution of the surface of penalised fluid during the simulation: comparison of three meshes (same colour) (bottom).

3.4.2 Cylinders on slope

The routine added to THETIS is validated thanks to experiments of cylinders sliding down an incline. Experiments were realised with and without water in the tank. These

	Trough 1		Peak 1		Trough 2		Peak 2	
	y/y_{ini}	$t(s)$	y/y_{ini}	$t(s)$	y/y_{ini}	$t(s)$	y/y_{ini}	$t(s)$
Maskell & Ursell [62]	-0.677	0.322	0.345	0.646	-0.242	0.934	0.151	1.250
Itō [45]	-0.599	0.339	0.301	0.659	-0.180	0.942	0.111	1.243
mesh 1	-0.616	0.344	0.298	0.663	-0.186	0.974	0.101	1.282
mesh 2	-0.624	0.340	0.310	0.655	-0.192	0.962	0.112	1.268
mesh 3	-0.625	0.337	0.315	0.650	-0.188	0.955	0.122	1.257

Table 3.2: First two throughs and peaks amplitude and time from the analytical, experimental and numerical results

simulations were intended to validate the management of the collisions by the routine and the interaction solid/fluid.

Set-up

To limit the rotation of cylinders on the incline which so far cannot be managed by our method, experiments with half-cylinders, cut lengthwise, placed on the slope have been carried out by our colleague Yves Le Guer and his students in a tank of dimensions $3.31\,m \times 0.6\,m \times 0.08\,m$ (Figure 3.12).

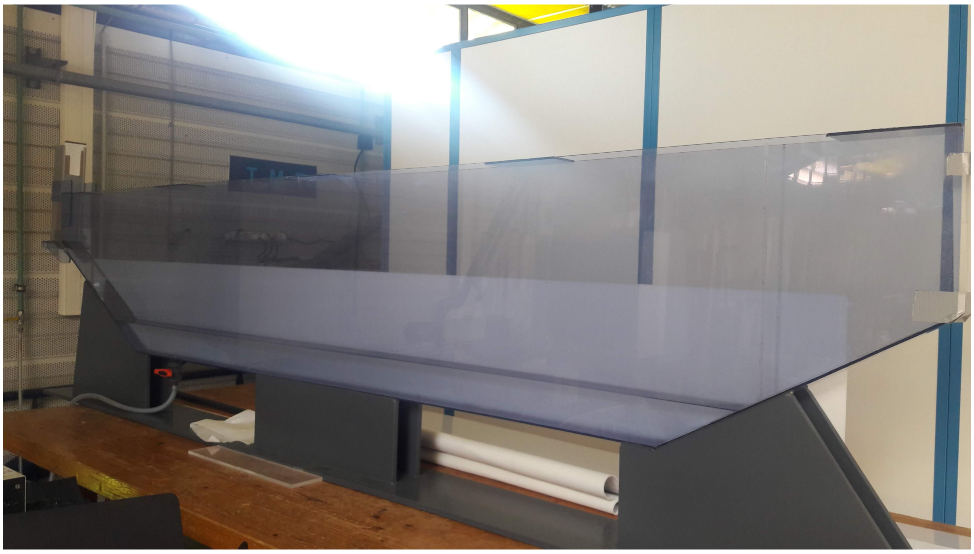

Figure 3.12: Picture of the experimental tank with two inclines and a reservoir on the left incline

The other limitations of the code is that the half-cylinders can not pass from the incline to the bottom of the tank because only no-slip condition is possible on obstacles.

The cylinders and half-cylinders are placed on the 30° incline, above water at the limit of the free surface (Figure 3.13). The water depth is $10\,cm$, the cylinders are in aluminium (density $\rho = 2700\,kg.m^{-3}$) and have a radius of $3\,cm$. In the experiment, half of the disc surface of the cylinders are painted in black in order to observe their rotation. The cylinders are initially held by a stick (Figure 3.15 for example).

The numerical domain is inclined to have the slope as a domain boundary so slip condition can be imposed (Figure 3.14). Therefore, the gravity vector is also inclined of 30°. In this configuration, the incline has slip condition but the bottom of the tank is an obstacle and has a no-slip condition. The mesh is particularly fine near the cylinders with $dx = dy = 0.001\,m$. During the experiments, a lot of drops are generated when the cylinders fall into water. For this reason, a VOF-TVD scheme is used for water interface. However, the routine seems to have problems of neighbour detection with this method so a VOF-PLIC scheme is used for penalised fluid interfaces. Moreover, the viscosity of water and air is multiply by 100 in order to reduce the turbulence during wave generation and the difference between fluid penalised, water and air viscosities which make the resolution of equations more complex. Time steps are adjusted to have the CFL number equals to 0.3. Cylinders are initially placed at a distance of four cells between them, namely $0.004\,m$. This distance enables to have a little margin on the minimum of two cells for the cylinders not to merge.

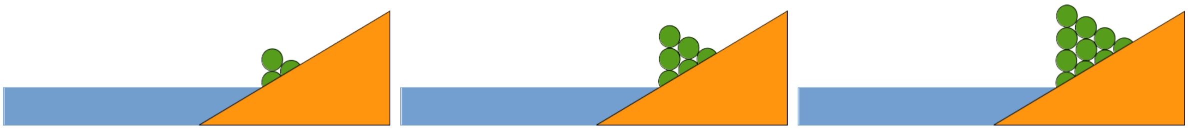

Figure 3.13: Sketches of the cylinder experiments with two half-cylinders and one cylinder, three half-cylinders and three cylinders, four half-cylinders and six cylinders with water

Without water

A first case with two half-cylinders, one cylinder and without water is presented. Cylinders are initially $10\,cm$ above the bottom of the tank, namely the same distance as in cases with water. Figure 3.15 compares experimental and numerical results. In both, the half cylinders split apart and the full cylinder falls between them. Numerical cylinders are delayed first, then catch up the experimental ones on the sixth picture, namely around $t = 0.31\,s$, because of the lowest friction during simulation due to the slip condition. The three numerical solids are then blocked at the bottom of the incline as the lower half cylinder can not pass the change of angle with the tank bottom, whereas experimentally they continue their trajectory and stop around $x = -0.36\,m$ for the first half cylinder.

With water

The same experiment is performed with water. First with the same number of cylinders and then in the two configurations showed on Figure 3.13.

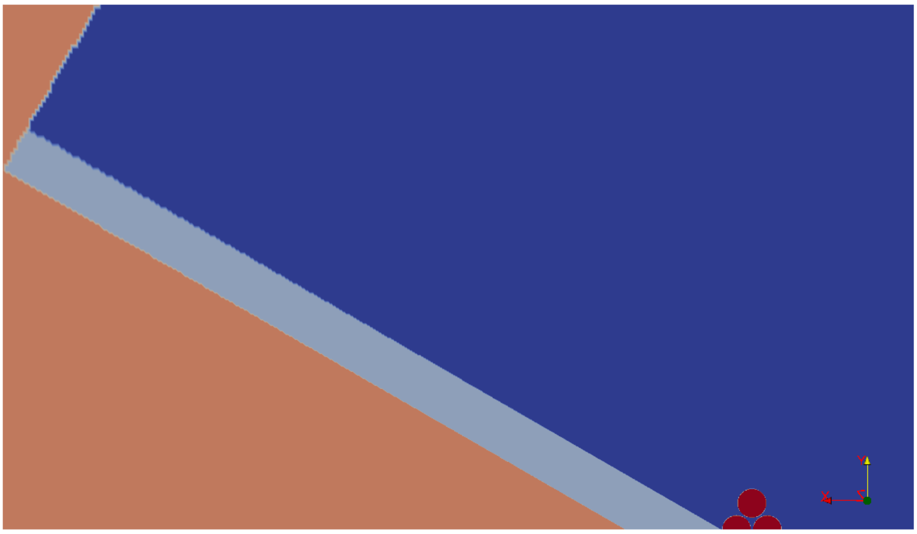

Figure 3.14: Numerical domain of the simulations with cylinders and half-cylinders on slope

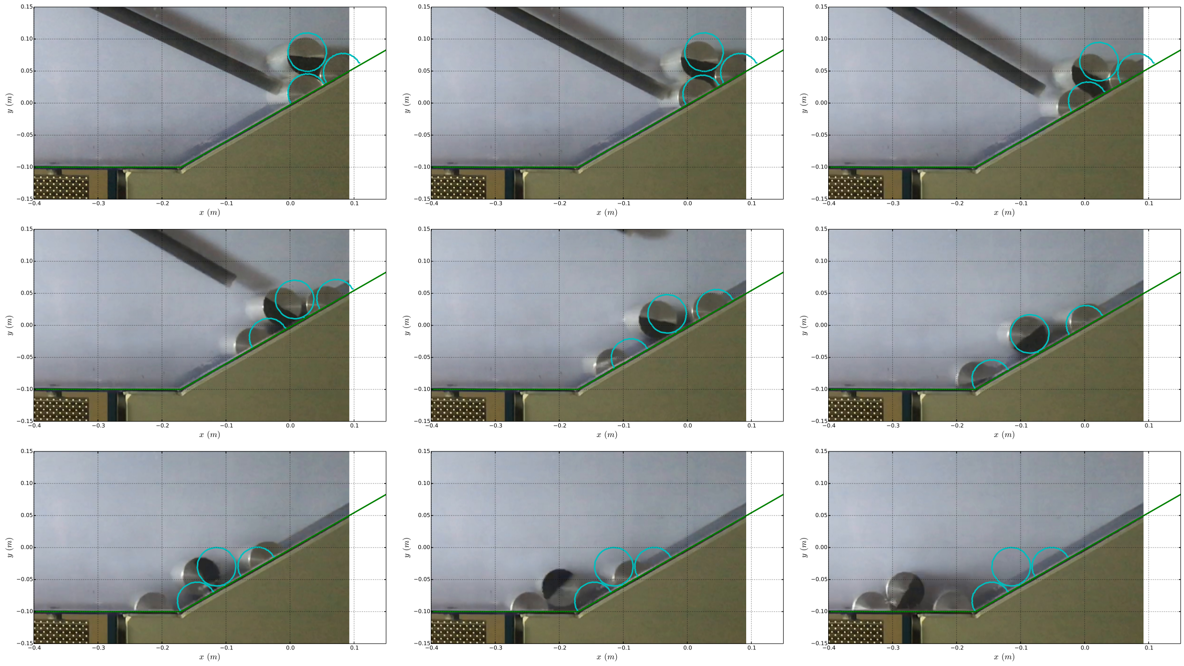

Figure 3.15: Pictures of the experiment with two half-cylinders and one cylinder, 0.0625 s time difference between two pictures, in cyan numerical cylinder contours.

Two half-cylinders, one cylinder Results for two half cylinders and one full cylinder are illustrated on Figure 3.16. The motion of the cylinders in the experiment is similar to the experiment without water, the two half cylinders split apart and the full cylinder fall between them. The lower half cylinder takes twice the time to reach the bottom of the tank. The splitting is not observed in the simulation. The numerical lower half cylinder reaches the tank bottom a little earlier than in the experiment due to the slip condition on the incline. The numerical full cylinder passes above the lower half cylinder and fall on the bottom of the tank, its movement is stopped due to the no-slip condition on the obstacle.

As for wave generation, for both experiment and simulation water is lifted by the cylinders. From this a first wave is generated and propagates in the tank. This wave amplitude is more important in the simulation, propably because of the position of the full cylinder that seems to lift a greater water volume. In addition to wave generation, a run-up on the incline is observed in the simulation and is absent in the experiment. This run up seems to be induced by a water jet caused by the fall of the full cylinder in front of the half cylinder.

Three half-cylinders, three cylinders Figure 3.17 shows experimental and numerical results for the setup with three half cylinders and three full cylinders. In both experiment and simulation, the cylinder stack begins to collapse from the lower part. Motion of cylinders during the simulation is close to what is observed in the experiment except that half cylinders reach the bottom of the tank.

The wave generation is quite similar between experiment and simulation with an amplitude slightly greater for the latter.

Four half-cylinders, six cylinders Illustrations of numerical and experimental resuts are presented on Figure 3.18. In this case, cylinder motion is quite different between simulation and experiment. The stack does not collapse from the front but two full cylinders are pushed above the lower half cylinder. This difference is due to the initial distance between the cylinders which makes the stack unstable. A $t = 0\,s$, the cylinders are released and because of this distance, they fall and the routine detects these collisions and the more cylinders, the more chaotic the reaction. After some time, a few cylinders merge despite the routine and the stack reaches an equilibrium state.

Because of the angle formed by the three cylinders at the front of the stack, a jet of water is generated which is not observed in the experiment.

3.4.3 About these simulations

Some remarks can be drawn from these simulations.

- Contrary to experiments where water passes between the sides of the tank and cylinders, water does not penetrates between cylinders.
- It would be interesting to make experiments where cylinders are blocked at the bottom of the incline.

Figure 3.16: Pictures of the experiment with two half-cylinders and one cylinder, 0.0625 s time difference between two pictures

- The more cylinders, the more difficult the simulation because of the initial distance between cylinders that makes the computation more complex.

3.5 Conclusion and perspectives

This chapter proposes to model a slide with several solid discs. The routine succeeds in managing the collision but still shows some instabilities growing with the number of discs.

However, this simple model has showed that solid/solid interactions can be managed by a Navier-Stokes code. Simulations can not be realised at a granular scale due to high

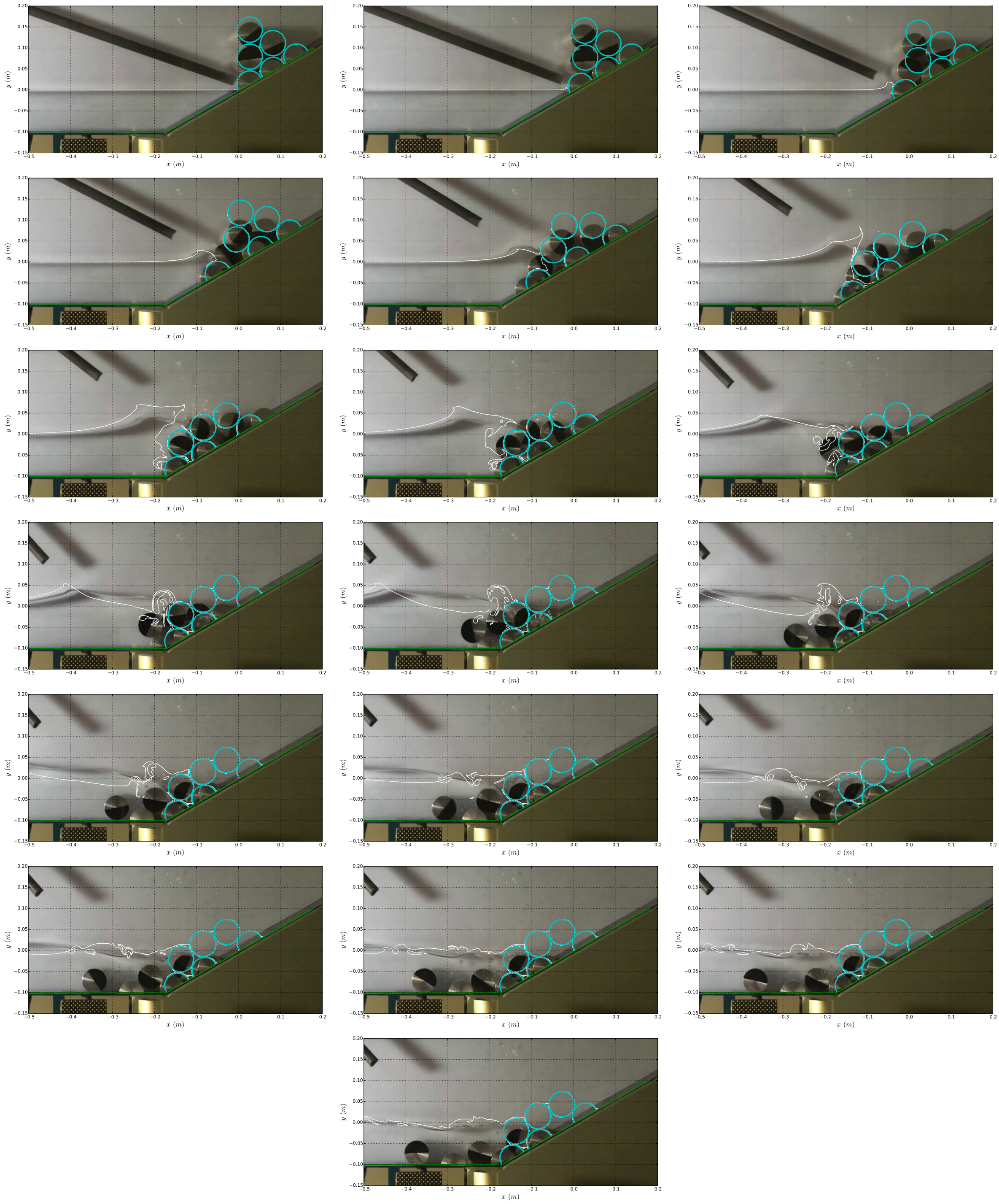

Figure 3.17: Pictures of the experiment with three half-cylinders and three cylinders, $0.0625\,s$ time difference between two pictures

computational cost associated to this approach but this can open new opportunities for simulations with a few solid blocks not only for wave generation. For instance, it could be applied on wave impact on a dike composed of solid blocks.

The main difficulty experienced is to find experiments for the model validation because of the limitations of the code (no slip and no rotation on the boundaries). New experiments with the cylinders stopped at the bottom of the incline could be easier to reproduce.

To go further on this model, improvements can be added. For instance, it would be possible to:

- add friction between solids.
- manage other geometry of solids.
- manage interaction with fixed obstacles.

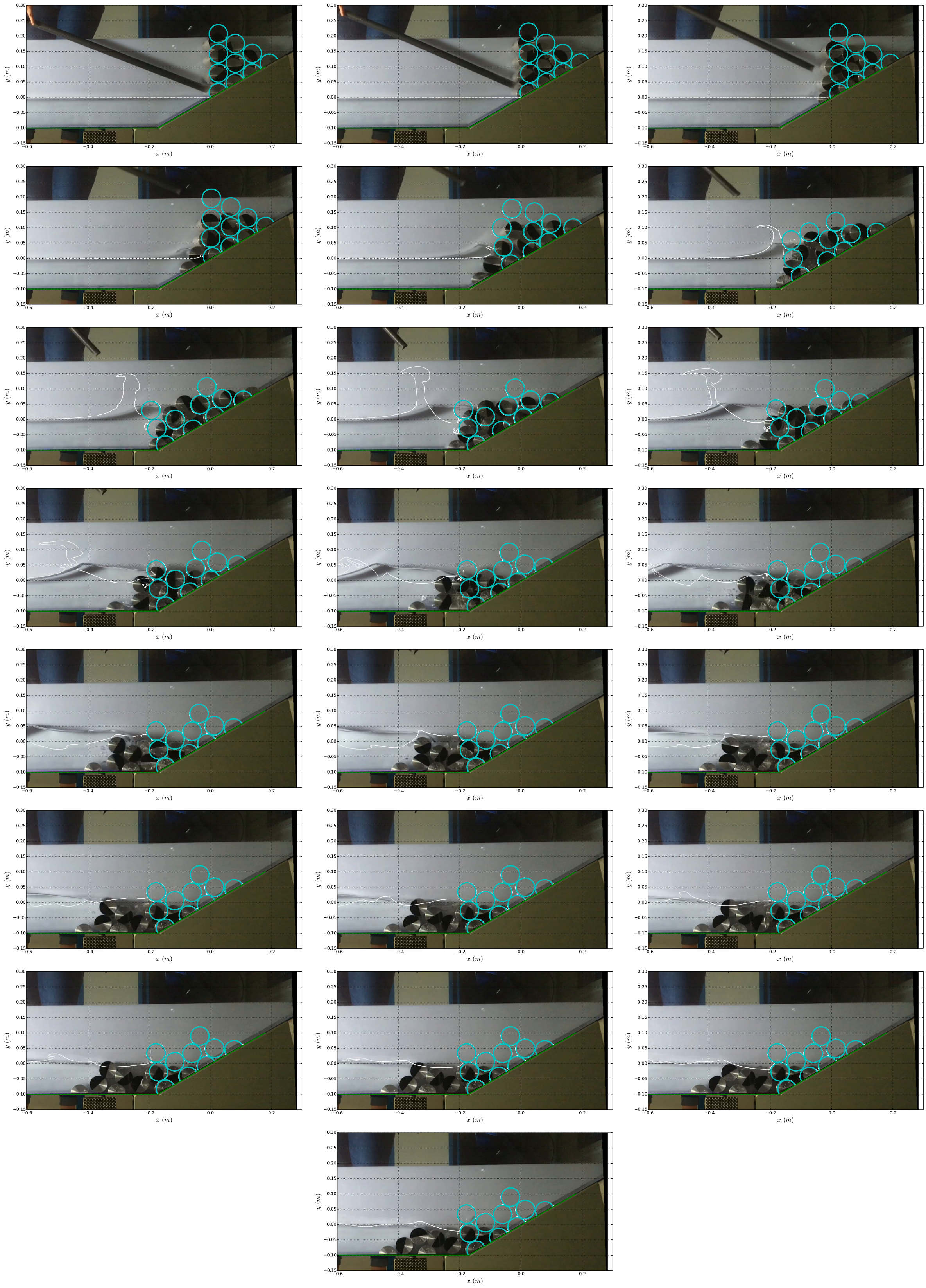

Figure 3.18: Pictures of the experiment with four half-cylinders and six cylinders, 0.0625 s time difference between two pictures

CHAPTER

FOUR

GRANULAR FLOW: A CONTINUOUS APPROACH

Contents

4.1 Introduction

In the present section, the wave generation process is simulated for two cases of granular slide (subaerial and submarine). The granular slide is modelled as a fluid either based on a simple viscous Newtonian approximation or a more elaborated non-Newtonian $\mu(I)$-rheology. The potential, kinematic and dissipated energies are computed at each time step in the water and the slide, giving the whole process of energy transfers from the slide to the waves. Finally, the wave generation process is discussed.

4.2 Method

4.2.1 Benchmark test presentation

The numerical model was tested using two series of available experimental data involving the wave generation by granular slides. The first one (Viroulet et al. [87]), is a subaerial case, initially retained by a gate just a the level of the water free surface with no initial velocity when it impacts water. It is therefore very different from the experiments of impulse waves generated by granular slides presented by Fritz et al. [24] and Heller & Hager [42] where the slide has an impact velocity of 2.06-8.77 m/s (Heller & Hager [43])). The second one (Grilli et al. [31]) is a submarine landslide case, similar to the subaerial case of Viroulet et al. [87] in terms of its initial dimensions.

Case 1 : Subaerial case Viroulet et al. [87] conducted an experiment in a tank of dimension 220 cm in length, 40 cm in height and 20 cm in width with a water depth of 148 cm (Figure 4.1(a)). A mass of 2 kg of spherical glass beads of 1.5 mm of diameter and density of 2500 $kg.m^{-3}$ was placed on a slope of 45° at the limit with the water free surface. Four gauges of water elevation were disposed at 0.45 m, 0.75 m, 1.05 m and 1.35 m from the gate.

A $t = 0\,s$, the granular material is released. The glass beads slide down the slope toward the bottom of the tank and finally stop under the action of the different dissipative forces (Figure 4.1(b)). When the slide penetrates into water, the free surface is lifted up and forms the first wave that propagates in the tank followed by the trailing waves, in which the second appears to be the largest.

Submarine case The submarine case (Grilli et al. [31]) is similar to the subaerial experiment except that the granular media is released underwater. A sketch of the 6.27 m long flume is presented on Figure 4.2 (a). A 2 kg mass of glass beads of diameter 4 mm is released on a slope of 35° (Figure 4.2(b)). The water depth is 0.330 m. Four gauges are placed at $600, 1600, 2600, 3600\,mm$ from the gate to record the water surface fluctuations. Two larger waves followed by a wave train are generated. Contrary to the subaerial case, the second wave is larger that the first one. Moreover, there is no impact as the slide is initiated underwater and with the same mass of glass beads, the wave is smaller than for the subaerial case (maximum elevation for the subaerial case: 2 cm, and for the submarine case: 0.6 cm.

4.2.2 Numerical model

A free slip conditions are imposed on the velocities on the left, right and top domain faces while a wall condition is imposed on the bottom boundary. The slope is obtained by positioning a porous body [15] with a nil porosity. The computational mesh follows the

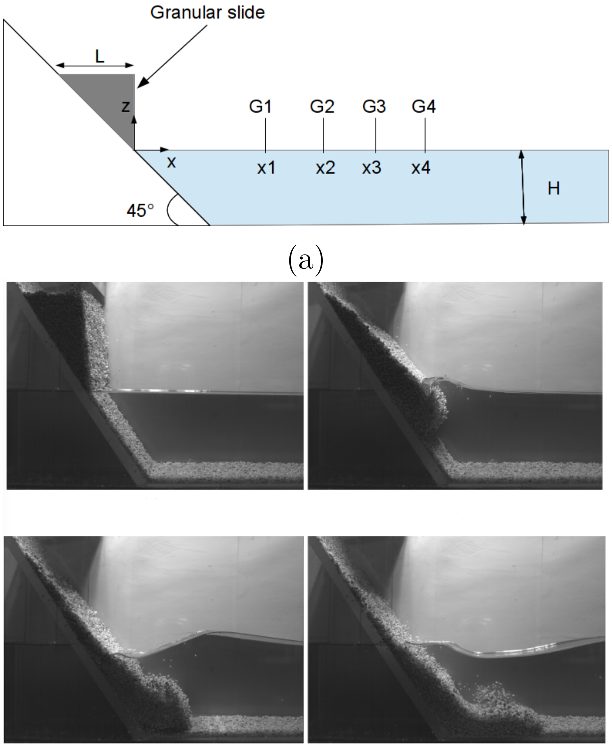

(a)

(b)

Figure 4.1: Subaerial test case. (a) Sketch of the experimental set-up and (b) snapshots of the generation area at different times ($0.2\,s$ between pictures), from Viroulet et al. [87]

geometry of each solid part of the domain with a stair-like slope. According to the simulations we performed, the mesh resolution ($\Delta x = 5\,mm$, $\Delta y = 2\,mm$ and $\Delta x = 2.85\,mm$, $\Delta y = 1.25\,mm$ in the subaerial and submarine case respectively) used is sufficient to limit the effects of the slope irregularities on water and slide flows.

The water, the air and the slide are firstly modelled as Newtonian fluids, giving one parameter, namely viscosity, for the slide to be calibrated. Then, the slide is modelled as a fluid with a $\mu(I)$-rheology (Section 2.5).

4.2.3 Energy transfers

The slide potential energy is maximum at the initial time. During the landslide motion, a part of the potential energy is converted into kinetic energy, lost due to the viscous dissipation, and converted into the water kinetic and potential energies including wave energy which is of interest here.

During the simulations, the different energy components are computed in the slide and water in order to better understand the energy transfer process and in particular determine the time duration of energy transfer from the slide to waves and the ratio or efficiency of this energy transfer.

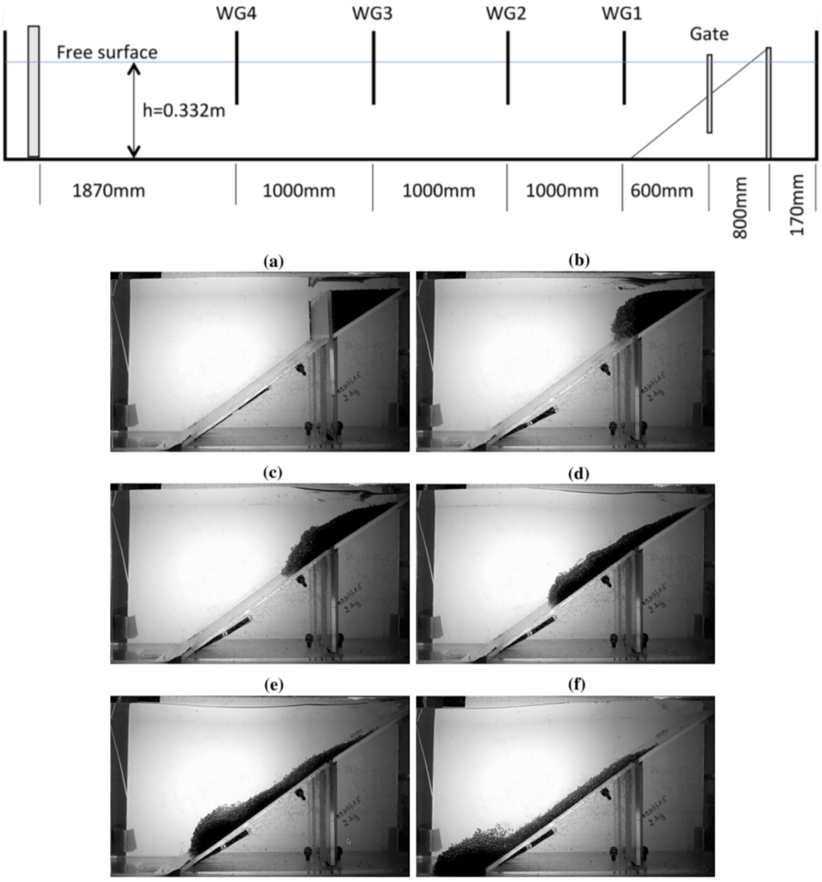

Figure 4.2: Submarine landslide test case. (a) Sketch of the experimental set-up and (b) snapshots of the generation area at different times $t = -0.125, 0.02, 0.17, 0.32, 0.47, 0.62\,s$, from Grilli et al. [31].

The local formulation of the kinetic energy theorem gives (with gravity as the only volume force):

$$\frac{\partial}{\partial t}\left(\frac{1}{2}\rho v^2\right) + \nabla\cdot\left(\frac{1}{2}\rho v^2\underline{v}\right) = \rho\underline{v}\cdot\underline{g} + \nabla\cdot\underline{\underline{\tau}}\cdot\underline{v} - \nabla\cdot p\underline{v} + p\nabla\cdot\underline{v} - \underline{\underline{\tau}}:\underline{\underline{D}} \tag{4.1}$$

By integrating this equation over the fluid volume (i.e., either the slide ,water or air volume), it leads to:

$$\begin{aligned}&\iiint_\Omega \frac{\partial}{\partial t}\left(\frac{1}{2}\rho v^2\right)d\Omega + \iint_{\partial\Omega}\frac{1}{2}\rho v^2\underline{v}\cdot\underline{n}dS = \\ &\qquad\iiint_\Omega \rho\underline{v}\cdot\underline{g}d\Omega + \iint_{\partial\Omega}(\underline{\underline{\tau}}\cdot\underline{v})\cdot\underline{n}dS - \iint_{\partial\Omega}p\underline{v}\cdot\underline{n}dS + \iiint_\Omega p\nabla\cdot\underline{v}d\Omega - \iiint_\Omega \underline{\underline{\tau}}:\underline{\underline{D}}d\Omega\end{aligned} \tag{4.2}$$

Using the transport and the continuity equations, it can be written as:

$$\overbrace{\frac{d}{dt}\iiint_{\Omega}\left(\frac{1}{2}\rho v^2\right)d\Omega}^{\text{a}}+\overbrace{\frac{d}{dt}\iiint_{\Omega}(\rho g z)d\Omega}^{\text{b}}+\overbrace{\iint_{\partial\Omega}\left(\frac{1}{2}\rho v^2+\rho g z\right)(\underline{v}-\underline{v}_a)\cdot\underline{n}dS}^{\text{c}}+\overbrace{\iint_{\partial\Omega}p\underline{v}\cdot\underline{n}dS}^{\text{d}}=$$
$$\overbrace{\iint_{\partial\Omega}\underline{\underline{\tau}}\cdot\underline{v}dS}^{\text{e}}+\overbrace{\iiint_{\Omega}p\nabla\cdot\underline{v}d\Omega}^{\text{f}}-\overbrace{\iiint_{\Omega}\underline{\underline{\tau}}:\underline{\underline{D}}d\Omega}^{\text{g}} \tag{4.3}$$

including kinetic energy variation (a), potential energy variation (b), kinetic and potential fluxes through the envelope (c), power of the pressure force on the envelope (d), power of the viscous stress on the envelope (e), power of the pressure force in the volume (f) and rate of the viscous dissipation (g).

(f) vanishes assuming incompressible fluids. In our case, the envelope velocity is equal to the fluid velocity, therefore (c) is also nil. In the following equation, the left-hand side contains the terms that are calculated while the terms on the right-hand side are deduced from the numerical computation.

$$\frac{d}{dt}(E_k+E_p)+\Phi=\iint_{\partial\Omega}\underline{\underline{\tau}}\cdot\underline{v}dS-\iint_{\partial\Omega}p\underline{v}\cdot\underline{n}dS \tag{4.4}$$

Where $E_k=\iiint_{\Omega}\left(\frac{1}{2}\rho v^2\right)d\Omega$, $E_p=\iiint_{\Omega}(\rho g z)d\Omega$, $\Phi=\iiint_{\Omega}\underline{\underline{\tau}}:\underline{\underline{D}}d\Omega$

Equation 4.4 shows that changes in the mechanical energy within the fluid volume is due to the total power of pressure force and shear stress on the fluid envelope. Hence, for water, changes in the total mechanical energy is through the pressure and the shear forces induced by the slide along the slide/water interface and vice versa. The balance equation (4.4) can be written for all three considered fluids, namely the slide, water and air volumes. By computing the air energy, it is remarked that its value does not change significantly during the simulation (section 4.3.2). Therefore, only the variation of energy in the slide and the water portions are considered. Based on the Newton's third law, the right hand sides of the energy balanced equations written for the slide and the water are equal (action-reaction) in each control volume. For this reason, the integrated left hand terms of this equation computed for one phase represents the energy transferred to the other phase.

The dissipation term $\underline{\underline{\tau}}:\underline{\underline{D}}$ is numerically computed for an incompressible Newtonian fluid, namely:

$$\underline{\underline{\tau}}:\underline{\underline{D}}=2\mu D_{ij}D_{ij} \tag{4.5}$$

By integrating equation (4.4) between times 0 and t, the transferred energy can be expressed as:

$$E_t(t)=E_k(t)+E_p(t)-E_k(0)-E_p(0)+\int_0^t\Phi dt' \tag{4.6}$$

The total mechanical energy can be defined as $E_m=E_k+E_p$, therefore :

$$E_t(t) = E_m(t) - E_m(0) + \int_0^t \Phi dt' \tag{4.7}$$

This transferred energy is positive if the fluid studied (i.e., slide or water) gains energy, negative in case of a loss of energy.

Following the previous set of equation, the computation of the different energy components is carried out for the slide, water and air domains separately as follows:

$$E_k = \sum_{i=1}^{N_X} \sum_{j=1}^{N_Y} \phi(i,j) \frac{1}{2} \rho V(i,j)^2 \Delta x(i,j) \Delta y(i,j) \tag{4.8}$$

$$E_p = \sum_{i=1}^{N_X} \sum_{j=1}^{N_Y} \phi(i,j) \rho g y(i,j) \Delta x(i,j) \Delta y(i,j) \tag{4.9}$$

$$\Phi = \sum_{i=1}^{N_X} \sum_{j=1}^{N_Y} \phi(i,j) 2\mu D_{kl}(i,j) D_{kl}(i,j) \Delta x(i,j) \Delta y(i,j) \tag{4.10}$$

where N_X and N_Y are the number of nodes in the direction X and Y respectively, ϕ is the color function value of the phase, Δx and Δy are the cell size in the direction X and Y respectively.

To separate the wave energy from the water energy, the water domain is divided in two zones (Figure 4.3) : the generation zone (zone 1) and the propagation zone (zone 2). In the two experimental cases studied, waves propagate faster than the slide (subcritical cases), which helps defining the propagation zone as the one limited by the slide front. Additionally, one may expect zone 1 to be rotational and zone 2 irrotational. The squared vorticity is locally computed to verify this assumption. For this reason, it is considered that the water energy computed in the propagation zone is the wave energy. Kinetic and potential wave energy are computed as follows:

$$E_{k,w} = \sum_{i=X_P}^{N_X} \sum_{j=1}^{N_Y} \phi(i,j) \frac{1}{2} \rho v(i,j)^2 \Delta x(i,j) \Delta y(i,j) \tag{4.11}$$

$$E_{p,w} = \sum_{i=X_P}^{N_X} \sum_{j=1}^{N_Y} \phi(i,j) \rho g y(i,j) \Delta x(i,j) \Delta y(i,j) - \sum_{i=X_P}^{N_X} \sum_{j=1}^{Y_W} \rho g y(i,j) \Delta x(i,j) \Delta y(i,j) \tag{4.12}$$

where X_P is the abscissa limiting the propagation zone and Y_W the initial free surface elevation ordinate.

Jiang & LeBlond [47] formerly characterised the energy transfer ratio as the mechanical energy of the waves divided by the potential energy of the slide.

$$\lambda_{JLB} = \frac{E_{m,w}(t)}{E_{p,slide}(t) - E_{p,slide}(0)} \tag{4.13}$$

However, in the present study with Navier-Stokes simulations, the kinetic energy and the viscous dissipation of the slide can also be easily computed, and therefore the ratio of wave energy on the actual energy transferred to water can be accurately defined.

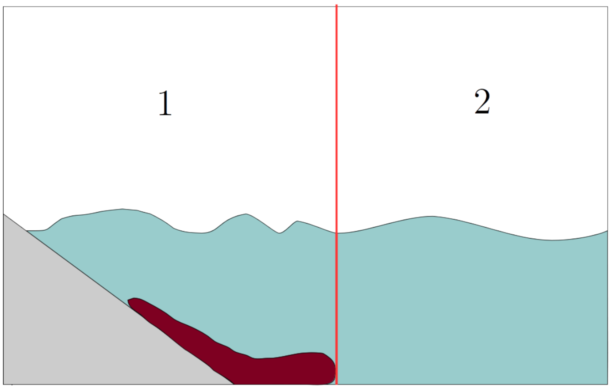

Figure 4.3: Sketch illustrating assumed generation (1) and propagation (2) zones

The instantaneous part of energy transferred to the waves that propagate offshore can then be expressed as:

$$\lambda(t) = \frac{E_{m,w}(t)}{E_{t,slide}(t)} \tag{4.14}$$

with $E_{t,slide}(t)$ the energy transferred by the slide defined by equation (4.7).

4.3 Results

4.3.1 Model validation

Subaerial landslide

The slide is first modelled as a Newtonian fluid with viscosity considered as a parameter to calibrate. The slide density value in the simulation may be questioned. At $t = 0\,s$, when the slide is at rest above water, with a random close pack, the maximum volume fraction of the beads is about 0.6, which gives a density of $1500\,kg.m^{-3}$ for the slide. However, the slide is moving beneath the water with a maximum density of $1900\,kg.m^{-3}$ for the most of the time of the experiment. Nevertheless, during the experiment, the slide volume expands (almost a 50% expansion) as the beads does not form a close pack. For this reason, the latter density is maximal and simulation were run with this density to show its influence on the wave heights. The change of density was found to have little influence on the wave heights. First and second waves are only slightly higher with the $1900\,kg.m^{-3}$ density. Therefore, in the following results, the density is set to $1500\,kg.m^{-3}$.

The focus is now on the influence of the viscosity value. With a low viscosity, the slide moves faster and a bulge shape slide front is observed similar to the experiment results (Figure 4.4(a)). The best results in terms of the slide motion are obtained with a viscosity of $2\,Pa.s$, even though in this case the slide is a bit slower than in the experiment. However, the height of the first wave at the four gauges (Figure 4.4(b)) appears to be almost twice as high as the experimental results for this viscosity. At a lower viscosity, the free surface elevation seems to be discontinuous because it is more perturbed due to wave breaking and harder to capture at the gauges. The first wave and the wave train are well reproduced for a viscosity of $10\,Pa.s$, even though the slide at this viscosity is shown to be slower than in the experiment. The same overall behaviour was observed in the second test performed in Viroulet et al. [87] with a glass beads diameter of $10\,mm$ (results not shown here), but a higher value of viscosity has to be set in order to fit the experimental wave heights.

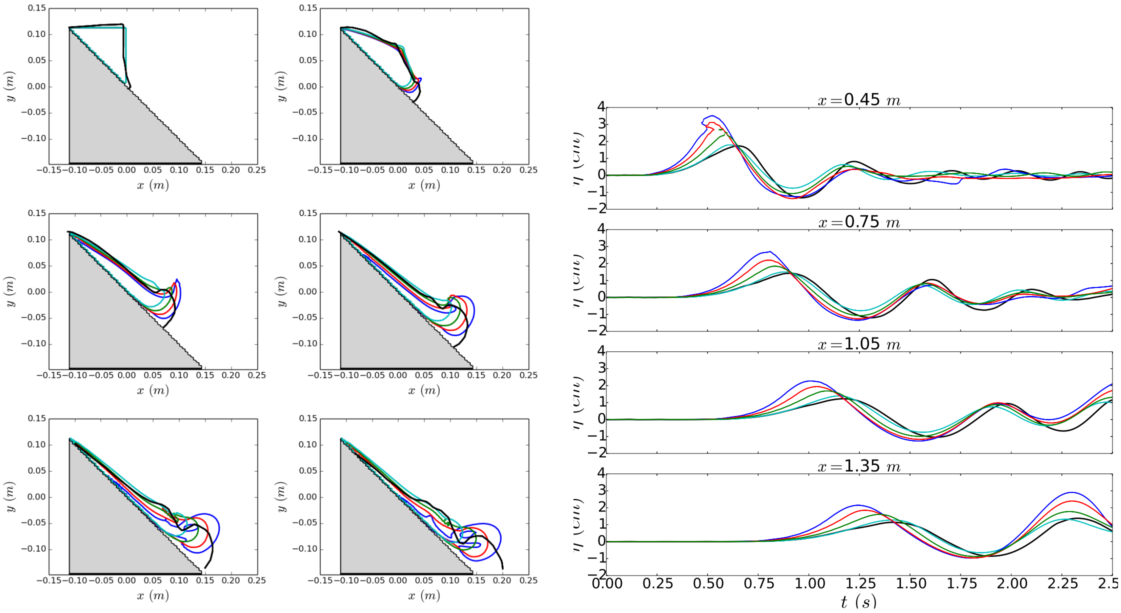

(a) (b)

Figure 4.4: Simulation results for different values of slide viscosity (Newtonian fluid). (a) : snapshots of slide contour and (b) : elevation of the free surface at the experimental gauges. Experimental results (black) line and the simulations for different viscosity values, $\eta = 1\,Pa.s$: blue, $\eta = 2\,Pa.s$: red , $\eta = 5\,Pa.s$: green and $\eta = 10\,Pa.s$: cyan; $0.1\,s$ between figures

Simulations were also performed with the $\mu(I)$-rheology for which the parameters are defined by the granular media. For the simulation, we took $I_0 = 0.279$, $\mu_s = 0.38$ and $\Delta\mu = 0.26$ from Pouliquen & Forterre [77]. From the $\mu(I)$-rheology, it is possible to approximate the viscosity of the fluid during the sliding (see Ionescu et al. [44]). It leads to:

$$\eta = \left(\mu_s + \frac{\Delta\mu}{\frac{I_0\sqrt{p/\rho_g}}{d\sqrt{2}D_2} + 1} \right) \frac{p}{\sqrt{2}D_2} \tag{4.15}$$

With $p = \rho_s g \frac{h_0}{2}$, $D_2 = \frac{\sqrt{g h_0}}{h_0/2}$, $d = 0.0015\,m$, $h_0 = 0.11\,m$, $\rho_g = 2500\,kg.m^{-3}$, $\rho_s = 1500\,kg.m^{-3}$, it leads to $\eta = 11.7\,Pa.s$ giving approximately the same value as the one finally chosen after test and error procedure for the Newtonian fluid consideration.

Figure 4.5 shows the evolution of the viscosity inside the slide during the simulation. After entering the water, the viscosity at the front part of the slide gets higher and the slide quickly stops. It seems that the water impact rapidly slows down the slide and based on the $\mu(I)$ formulation, increases the viscosity with decreasing the slide deformations which ends up stopping the slide. However, waves are generated very quickly in this experiment and we can see in Figure 4.6 (b) that the wave height is quite close to the experimental results. Comparing to the computation with the Newtonian fluid, during the first 0.5 s where the waves are generated, the deformation of the slide is very similar to the Newtonian slide (Figure 4.6 (a)).

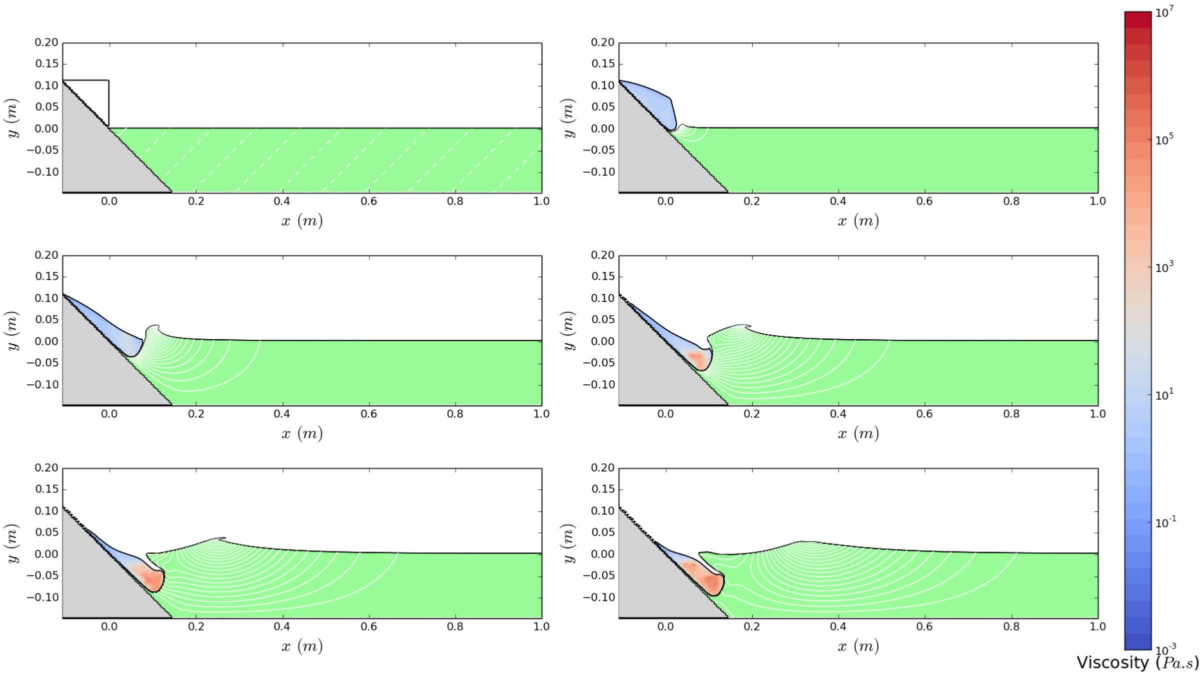

Figure 4.5: Simulation results for the $\mu(I)$ rheology. Evolution of the viscosity inside the slide, 0.1 s time difference between figures

Submarine test case

For the submarine landslide case, the numerical domain has a length of 6.27 m and a water depth of 0.33 m. The slide is modelled as a Newtonian fluid, with parameters defined in Grilli et al. [31], i.e. a viscosity of 0.01 $Pa.s$ and a density of 1951 $kg.m^{-3}$. A few other viscosity values are also considered to evaluate the sensitivity of the model to this parameter. No simulation with the $\mu(I)$-rheology are presented as the flow initiation has been proved to be difficult with the parameters from Pouliquen & Forterre [77].

Results of slide shapes and wave heights are presented in Figures 4.7 and 4.8. The slide shape evolution as well as the slide overall velocity is shown to strongly depend on the viscosity value. For the low viscosity used in Grilli et al. [31], the slide front exhibits

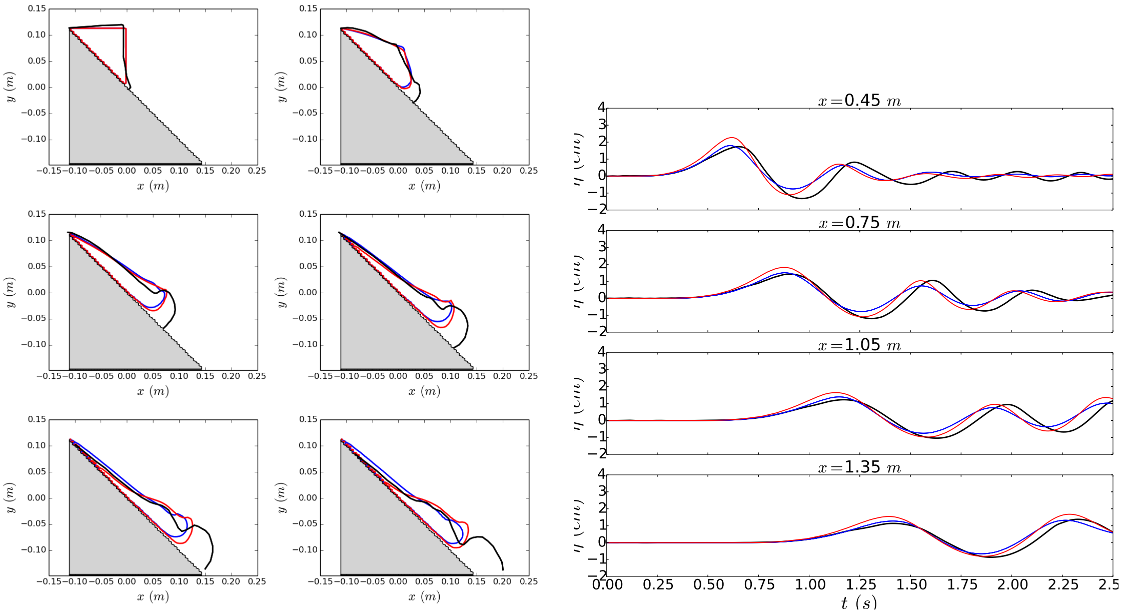

(a) (b)

Figure 4.6: Simulation results for the $\mu(I)$ rheology. (a) : snapshots of slide contour and (b) : elevation of the free surface at the experimental gauges. Experiment (black), and THETIS simulations (blue line: Newtonian fluid $\mu = 10\,Pa.s$, red line: $\mu(I)$-rheology)

a bulge head due to the presence of a strong counter-clockwise vortex generated at the water/slide interface. This vortex gets weaker and weaker with increasing the viscosity value. The experimental snapshots also show the occurrence of this vortex more or less consistent with the results corresponding to the two stronger viscosities tested in our simulations. Nevertheless, in all the cases tested, the slide motion appears to be very slow compared to the experiment. The best approximation would be with the lowest viscosity but due to the aforementioned large vortex and the subsequent additional drag induced, the slide velocity cannot reach higher values.

Figure 4.8 shows that with a slide viscosity of $0.01\,Pa.s$, the first wave is higher than the experimental value and the wave train is not correctly reproduced on the first gauge. By reducing the viscosity, the generated waves are lower. We observe that with a viscosity of $1\,Pa.s$, the first wave is close to the experimental results as well as the first waves in the train wave. Generally, the wave heights are closer to the experiment when the numerical slide moves slower than the experimental slide with having a higher viscosity.

4.3.2 Energy transfers

Simulations are now interpreted in terms of energy transfer from the slide to the generated waves.

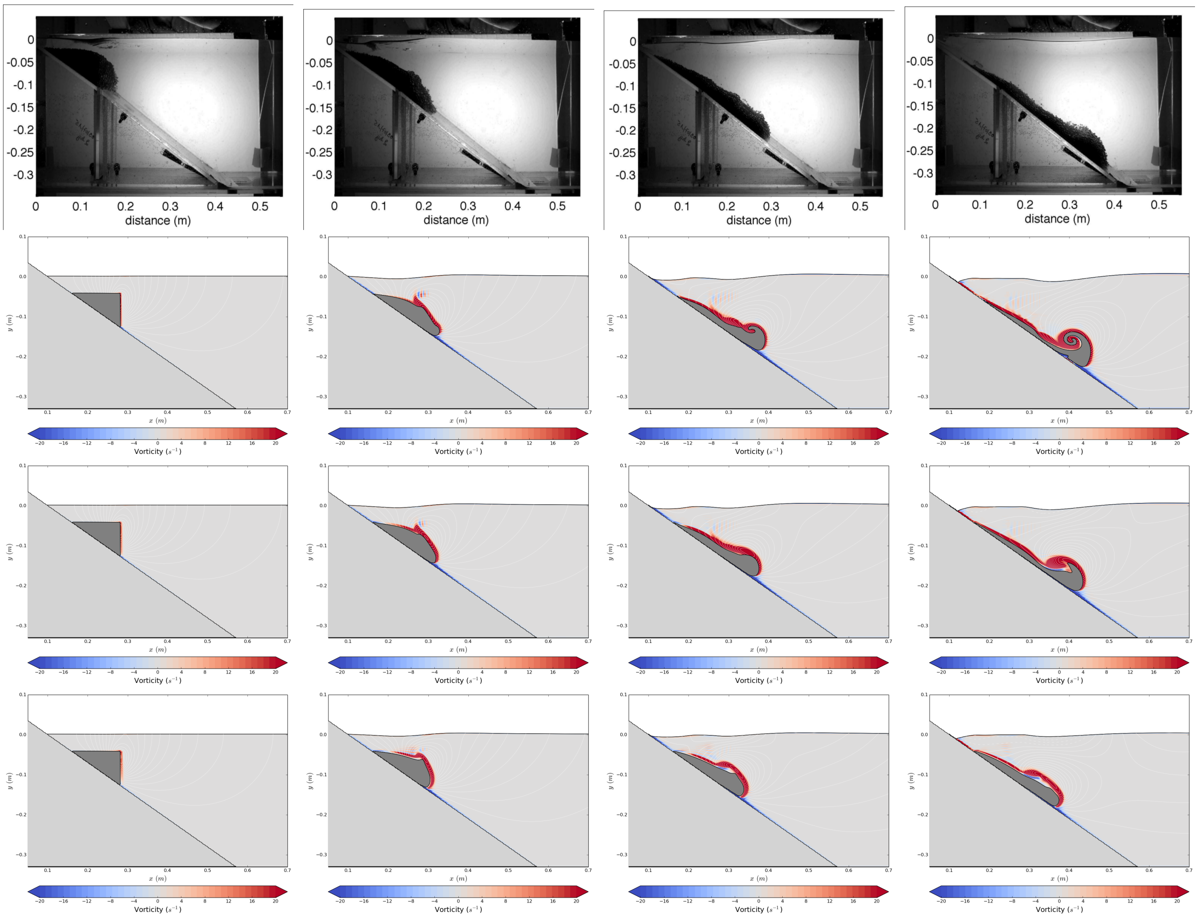

Figure 4.7: Slide colour function and vorticity contours for the submarine landslide benchmark (Grilli et al. [31]) with experiment results in the first row and simulation results (following rows) for different values of viscosity ($\eta = 0.01, 1, 10\,Pa.s$ for second, third and fourth row respectively) at times $t = 0.02, 0.17, 0.32, 0.47\,s$

Subaerial test case - Newtonian fluid

The total energy of the system {air+water+slide} should be constant in time. Figure 4.9 (a) illustrates the time evolution of the relative error of the total system energy which can be attributed to the numerical dissipation. This dissipation is very low and reaches only 0.3% at $2\,s$, the time at which, as will be shown below, most of the energy has been transferred. Therefore, the total energy is properly conserved during the simulation. Additionally, the air total energy varies only very slightly. Accordingly, only the transfer of energy between the water and the slide is considered in these simulations.

Figure 4.9 (b) illustrates the time evolution of energy components and energy dissipated at time t in the slide, with E_0 the initial slide mechanical energy. As the gate opens, the slide is released and flows over the slope. Its velocity increases and so does its kinetic energy (in red) but with fairly small amount compared to the potential energy decrease. Conversely, the total viscous dissipation, linked to the slide velocity and

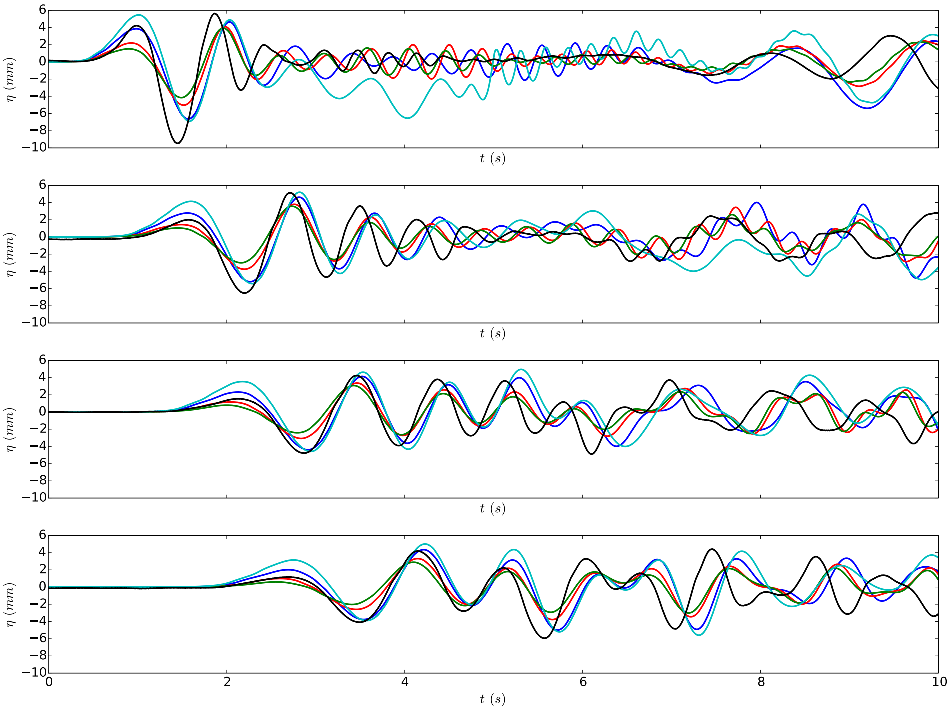

Figure 4.8: Elevation of the free surface for the submarine landslide benchmark (Grilli et al. [31]), comparison between experiment (black) and simulation results with different viscosity values (0.01 $Pa.s$: cyan, 1 $Pa.s$: blue, 5 $Pa.s$: red, 10 $Pa.s$: green)

the viscosity value, increases very significantly and reaches an asymptotic value as the slide stops. Likewise, the energy transferred to the water appears to be very significant compared to the slide kinetic energy.

Water is set in motion as the slide enters it and deforms the free surface, including kinetic and potential energies increase. The viscous dissipation in water (not shown here) is very small because of the low viscosity of water and represents less than 0.33% of the initial total water energy at $t = 2\,s$.

Regarding the distinction between wave generation and propagation, in this subaerial case, vorticity is confined near the slide and at the free surface (Figure 4.10). At the right of the slide, we observe the typical stream contours of a wave field. The limit between both zones, as defined previously, is therefore relevant. In the propagation zone, wave energy is computed. We see (Figure 4.9(c)) that the wave kinetic and potential energy increases quickly at the beginning of the simulation and stabilizes around $t = 0.5\,s$. The significant variation of energy around $t = 1.5\,s$ is explained by the reflection of the first wave on the side of the tank opposite to the slope (Figure 4.9 (d)).

The Figure 4.9 (e) shows the wave energy divided by the slide initial energy. The wave energy reaches its maximum at $t = 0.45\,s$ and then decreases slightly before stabilizing. This reduction of energy is due to the slight breaking of the first wave which may be observed on the third snapshot of the Figure 4.10. Therefore, we can conclude that the transfer to the wave field is very quick in this case and nothing more happens in terms of transfer to the free surface downstream the slide after $t = 0.45s$.

The transfer ratio is of course different considering equation 4.13 or equation 4.14, the first not considering the part of the slide energy going to kinetic energy and dissipation. These transfer ratios are plotted on Figure 4.9 (e) as soon as the wave energy has a non negligible value. Logically, the transfer ratio given by equation 4.13 has a lower value all along the simulation.

The ratio of wave to water energy shows a peak at $t = .2s$ around 0.5. When all the energy has been transferred to waves (t=.45s), the transfer ratio is about one third evidencing the efficiency of this subaerial slide to produce energetic waves. Afterwards, no more energy is transferred to the surface (and propagating off-shore) but as energy is still transferred to the water mass (Figure 4.9 (b)), the energy ratio decreases to an asymptotic value around 0.13 (0.067 with the transfer ratio of Jiang & LeBlond [47]).

Subaerial test case - $\mu(I)$ rheology

The wave generated by the $\mu(I)$-rheology slide are more energetic than in the Newtonian slide simulation (Figures 4.11). Moreover, the slide has transferred more energy during the $0.5\,s$ compared to the Newtonian slide. However, the transfer ratio at the wave maximum energy is lower because more energy is transferred to the water but not to the waves. One can remark that the slide stops around $0.6\,s$ and beyond that time no longer releases energy.

It is also observed (Figure 4.9 (d-e)) that the maximum of the waves energy is reached around $t = 0.5\,s$, namely a little before the slide stops. The final transfer ratio is 0.2, so significantly more than with the Newtonian fluid but this is only due to the fact that the slide stops in the second case, vanishing by this way, the energy transfer to water that still existed in the first case. We also noticed that the numerical dissipation appears more significant in this case (around 0.9%).

Submarine test case

Results for the submarine case are only presented with the slide modelled as a Newtonian fluid (Figure 4.12). The transfer of energy is very low, which explains the small waves observed in this case, compared to the subaerial case.

As in the subaerial case, the total energy of the system {air+water+slide} is preserved during the simulation with an error at $t = 5\,s$ of about 0.012% (Figure 4.12 (a)).

Figure 4.12 (b) illustrates the repartition of energy in the slide during the simulation. The results are very similar to the subaerial case, except that the greater water depth in this case causes more potential energy to be released. Similar to the subaerial case, the wave field potential energy (Figure 4.12) increases and then stabilizes itself to a constant value. However, in this case, the kinetic energy does not follow this pattern. It first increases faster than in the previous case, where the kinetic energy followed the potential energy (Figure 4.9 (c)). This behaviour is explained by the recirculation of the flow above the slide illustrated in Figure 4.14. When the slide is flowing over the slope, significant velocities appear just above the slide front. However, as soon as the slide reaches the bottom, this recirculation quickly moves to the back of the slide explaining the fast decrease of the kinetic energy in the propagation zone from the time $t = 0.9\,s$. It then decreases to reach the potential energy value but subsequently, increases again around $t = 2\,s$. This unexpected behaviour is explained by the presence of strong vorticity in the propagation zone (Figure 4.13). This vorticity, which was generated by the slide front, is then advected more rapidly than the slide itself. Therefore, the mechanical wave energy will be taken as twice the potential energy even if this hypothesis is known to be only approximative (Fritz et al. [24], Heller et al. [41]).

In this submarine case, the slide kinetic energy and the dissipation have low values compared to the slide potential energy so the transferred energy is almost equal to the potential energy (Figure 4.12 (a)). The difference between the ratio introduced by Jiang and LeBlond and Equation 4.14 is not very marked with a final transferred energy ratio of about 0.01 (Jiang and LeBlond) against 0.02 (Equation 4.14), with the wave mechanical energy taken as twice the potential energy until the waves are reflected on the opposite side of the tank (Figure 4.12 (d)). Moreover, the efficiency of the system, when no more energy is transferred to the waves (at t=1 s), is around 0.03, namely 10 times less than the subaerial case.

4.4 Discussion

A first observation by comparing the actual experiment and the simulations with the Newtonian fluid or the $\mu(I)$-rheology is that even if similar waves are generated, the slide shape and velocity are quite different.

We have tried several strategies to produce faster slides such as vanishing the basal friction, tuning the density, etc. but they did not have any significant effect on the slide velocity. The reason may be that the slide is simulated as an equivalent phase instead of a granular water mixed medium. The difference is important as the latter allows water to flow within, whereas the former does not. This differential flow may reduce very significantly the global drag on the slide, which could explain the final velocity reached in the experiment. A second approximation is that the volume fraction of grain is constant in the simulations, whereas, looking at the experiment, the granular slide expands significantly during the sliding and the volume fraction decreases.

The energy transfer ratio is often only based on the potential energy released by the landslides (Jiang & LeBlond [47]) or the kinetic energy (Fritz et al. [24]). The present paper shows that, at least, the slide energy dissipation should be taken into account to better understand the transfer process. Indeed, the asymptotic transfer ratio for the subaerial case is twice its value without taking the dissipation and kinetic energy into account. However, it has been highlighted, in section 4.3.2, that in the submarine case, the potential energy is predominant over the dissipation and kinematic energy. In this case, the two transfer ratios give similar values.

The energy transfer to the free surface was shown to be very quick in the subaerial case. In fact, the whole wave field seems completely determined at $t \approx 0.5s$. This time corresponds to the situation shown in Figure 4.5 (fourth and fifth panels). Because of this observation, we can say that the trailing waves are not generated by the slide. In order to evidence this further, a simulation is carried out with a slide artificially forced to stop very early in the simulation (stop time t_s respectively : $t = 0.2, 0.3, 0.4, 0.5, 0.6, 0.7\,s$) by using penalizing techniques (Ducassou et al. [19]).

For the lowest stop time value (i.e.,$t_s = 0.2,\ s$), the first wave is noticeably smaller than measured (Figure 4.15). With $t_s = 0.3\,s$, the wave train is only very slightly smaller than in the experiment and is very well reproduced for larger values of t_s. Figure 4.16 (a) illustrates the energy transferred by the slide to water in each simulation. A drop is observed in the wave total energy (Figure 4.16 (b)) due to a very quick water slowdown around the slide, but not at the free surface. This is less noticeable as the stop time is high and the flow around the slide has lower velocities. It appears clearly (Figure 4.16 (b)) that the energy released by the slide after $t = 0.5\,s$ does not contribute to the wave energy as its evolution in time is the same for the slide stopped at $t = 0.5\,s$ or after.

As a wave train is observed in each simulation even with the slide stopped very early, this support the hypothesis that the latter is not generated by energy transfer from the slide. However, it is not clear in the simulations whether the second wave is generated by the reflection on the slope or by dispersion of the first wave. Nonetheless, the wave train following the second wave is clearly generated by dispersion of the latter.

If we focus now on the first wave, the simulations with the slide stopped demonstrated that the wave can be quite accurately generated without modelling the slide flow from the release to the deposition. The slide dynamics and shapes between the Newtonian simulations of the slide stopped or not, the $\mu(I)$-rheology simulation and the experiment (Figures 4.6 (a)) are quite different. However, they succeed in generating very similar waves. This interrogates on the slide parameters that need to be respected for the generation of accurate waves.

4.5 Conclusion

Navier-Stokes simulations where the landslide is modelled by a Newtonian fluid or a $\mu(I)$-rheology have been presented on two cases: subaerial and submarine. By comparing with experimental results, we validated that the waves can be quite accurately reproduced. Moreover, the energy transfers between the slide and the wave have been studied, leading to the following conclusions:

- waves gain all their energy very quickly in the subaerial case (about $0.5\,s$) while it takes longer in the submarine case ($1\,s$).

- The process is significantly more efficient in the subaerial case than in the submarine case: about one third of the slide energy transferred to water is wave energy at the end of the transfer, 10 times less in the submarine case.
- With the simulations using the $\mu(I)$-rheology and stopping the slide on the slope, we showed that the wave train is not generated by energy transfer but is a consequence of the generation of the first wave. For this reason, for the prediction of maximum amplitude of wave generated by landslide, the whole dynamics of slide does not need to be accurately reproduced, only the first instants matter.

4.6 Application to the Cumbre Vieja Volcano

Based on these results, simulations on the CVV case already run by Løvholt et al. [57] and Abadie et al. [1] using non-viscous fluid have been carried out again with a Newtonian fluid. The characteristics of the CVV slide are scaled by respecting the Froude and Reynolds numbers between experiments and CVV scales.

$$\frac{u_{rs}}{\sqrt{gh_{rs}}} = \frac{u_{ls}}{\sqrt{gh_{ls}}} \tag{4.16}$$

$$\frac{\rho u_{rs} h_{rs}}{\mu_{rs}} = \frac{\rho u_{ls} h_{ls}}{\mu_{ls}} \tag{4.17}$$

with g earth acceleration, $u_{rs}(u_{ls})$ characteristic velocity, $h_{rs}(h_{ls})$ characteristic length scale and $\mu_{rs}(\mu_{ls})$ slide viscosity at real scale (resp. reduced scale). Combining the two equations leads to :

$$\frac{\mu_{rs}}{\mu_{ls}} = \sqrt{h_{rs}^3 h_{ls}^3} \tag{4.18}$$

Which for a viscosity $\mu_{ls} = 10\,Pa.s$ at reduced scale gives $\mu_{rs} = 4.4 * 10^7\,Pa.s$ at real scale given the length ratio. Considering that the slide considered in [1] (Figure 4.17) is partially submerged, the latter viscosity value is arbitrarily reduced to $\mu = 2 * 10^7\,Pa.s$ to take into account of the result obtained with Grilli's experiment. Based on these hypothesis, simulations were performed with three initial slide volumes corresponding to resp. 20, 40 and 80 km^3

4.6.1 Wave generation

Wave generation is computed with THETIS at a local grid around the CVV. As observed in THETIS computations presented in Abadie et al. [1], it is not necessary to model the landslide during its whole runout to obtain the wave generation but only during the supercritical period of the slide local Froude number (less than $100\,s$). Results are presented on Figure 4.18 for a volume of $80\,km^3$.

An initial phase of propagation consists in using this first computation as an initial state in the Boussinesq model FUNWAVE-TVD (Shi et al. [82]) at a local scale. This state is filtered in order to be adapted for a Boussinesq model (see Abadie et al. [1] for more details). Results of this initial phase is transferred to larger-scale simulations to predict impact on the European coastline.

4.6.2 Wave propagation

Several models are used to compute the wave propagation in Atlantic ocean. A few results are showed here comparing results on French coast for three models: Calypso (shallow water equations or Boussinesq equations following Pedersen & Løvholt [72]), FUNWAVE-TVD (Wei et al. [97]) and Telemac-2D (www.opentelemac.org).

Only wave impact in France for the $80\,km^3$ scenario is presented here. We obtain between 15 and 20 cm on the continental shelf (Figure 4.19(A)), between 30 and 40 cm in south Brittany (Figure 4.19(B)), between 15 and 25 cm in the Gironde estuary (Figure 4.19(C)), and between 30 and 40 cm in Saint-Jean-de-Luz (Figure 4.19(D)). The leading wave on Figures 4.19(A) to (D) reaches the gauges after 3 h 20 min (or 3 h 25 min since the landslide triggering), 4 h 10 min, 4 h 35 min and 3 h 40 min of propagation respectively, with periods of 30 min for the first two and 60 min for the last two. We observe a lag time of 5 to 10 minutes of the arrival times between the two slide scenarios.

All models give quite similar results except for high frequencies appearing especially for Calypso signal due to the difference of resolution between bathymetric grids.

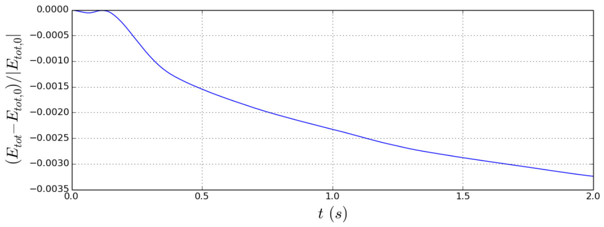

(a)

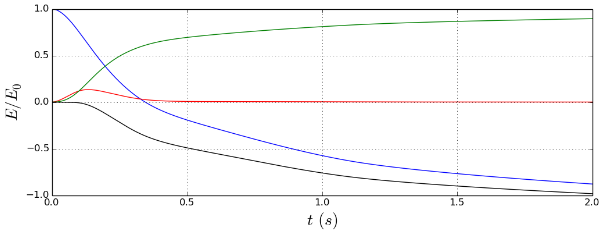

(b)

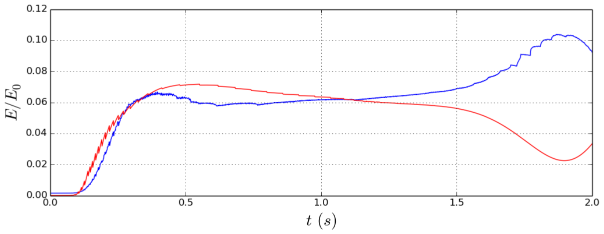

(c)

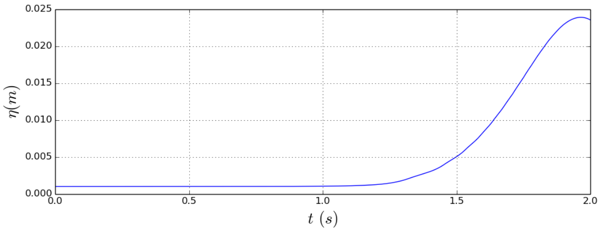

(d)

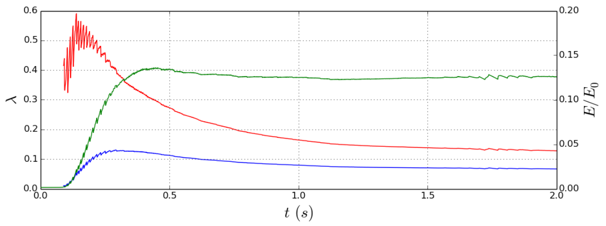

(e)

Figure 4.9: Time evolution of computed energy components in the subaerial benchmark case (Viroulet et al. [87] with Newtonian slide ($\mu = 10\,Pa.s$)). (a) Relative error on system total energy {air+water+slide} (b) Slide potential energy (blue), kinetic energy (red) and energy dissipated (green), Energy transferred to water (black), divided by the initial slide mechanical energy E_0 (c) Wave potential energy (blue), kinetic energy (red) divided by E_0, (d) Free surface elevation at $x = 2\,m$, (e) Evolution of the wave energy (green, right axis) divided by E_0, Transfer ratio (left axis) from Jiang and LeBlond from expression 4.13 (blue) and from expression 4.14 (red)

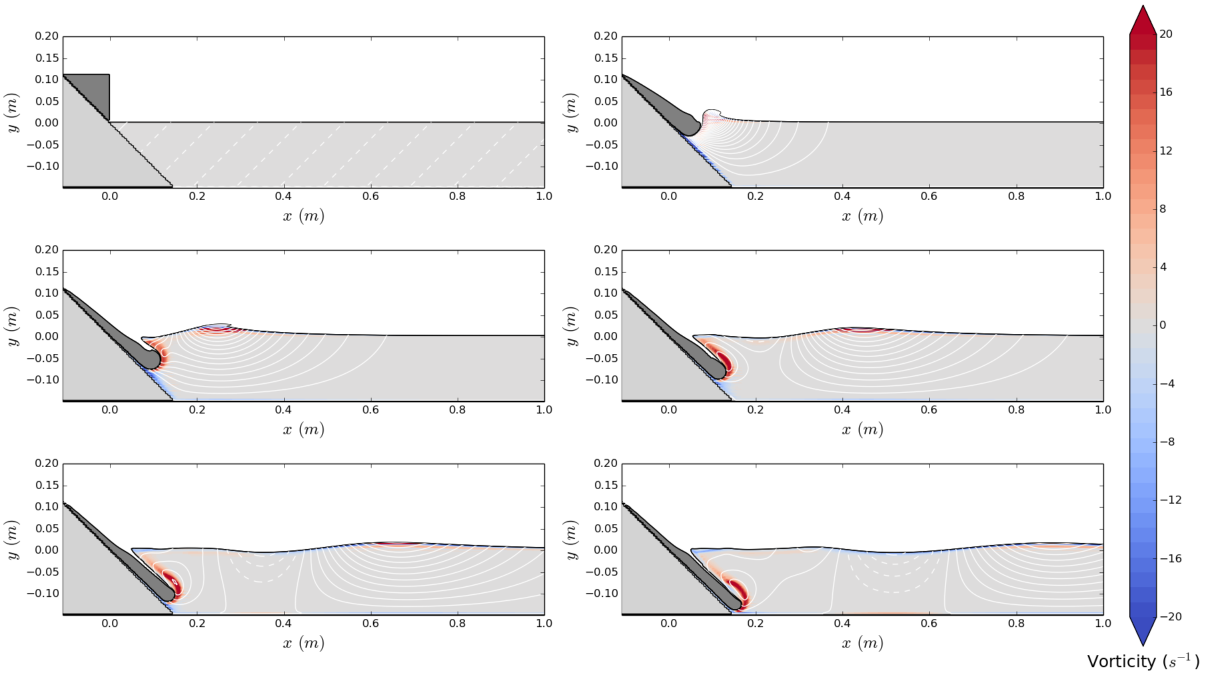

Figure 4.10: Slide snapshots with stream contour (white) and water coloured with vorticity, 0.2 s between two snapshots

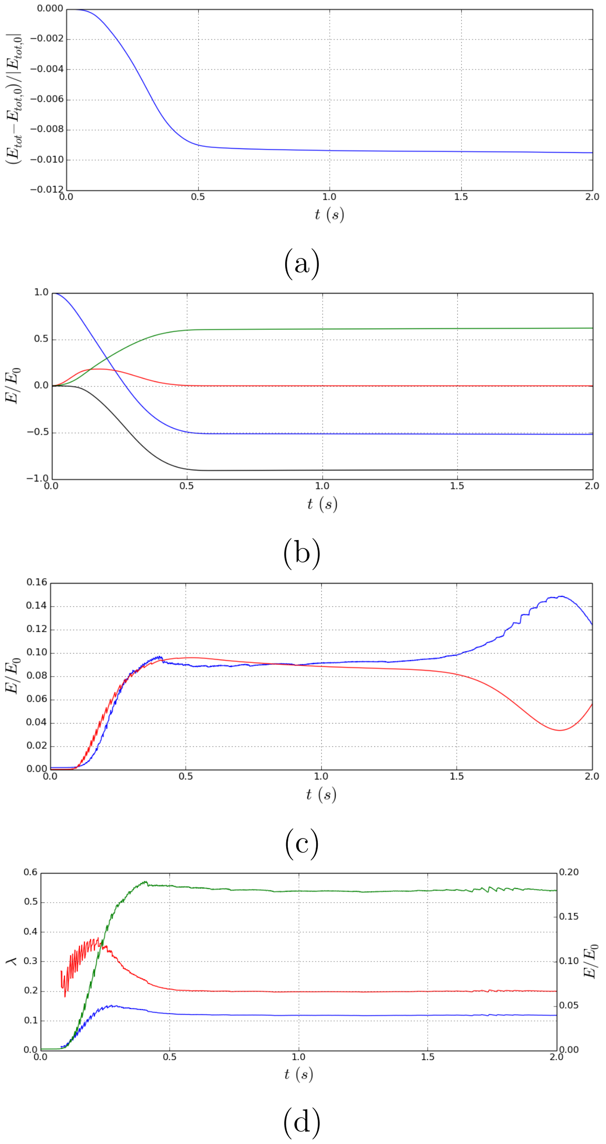

Figure 4.11: Same caption as figure 4.9 with $\mu(I)$ rheology

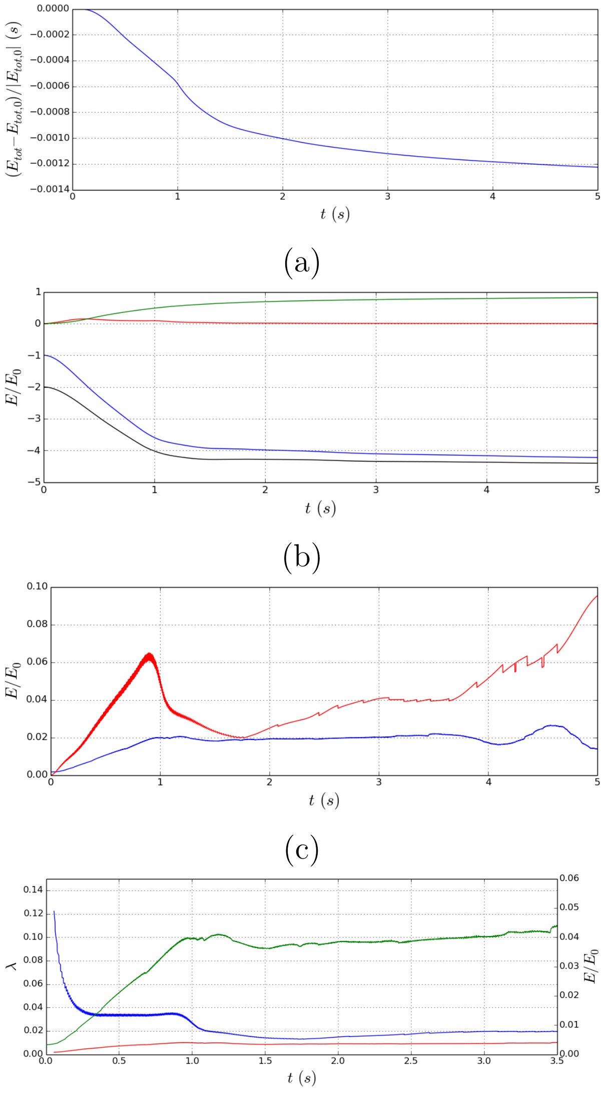

(a)

(b)

(c)

(d)

Figure 4.12: Same caption as Figure 4.9 for the submarine landslide case and a Newtonian slide with viscosity $1 Pa.s$

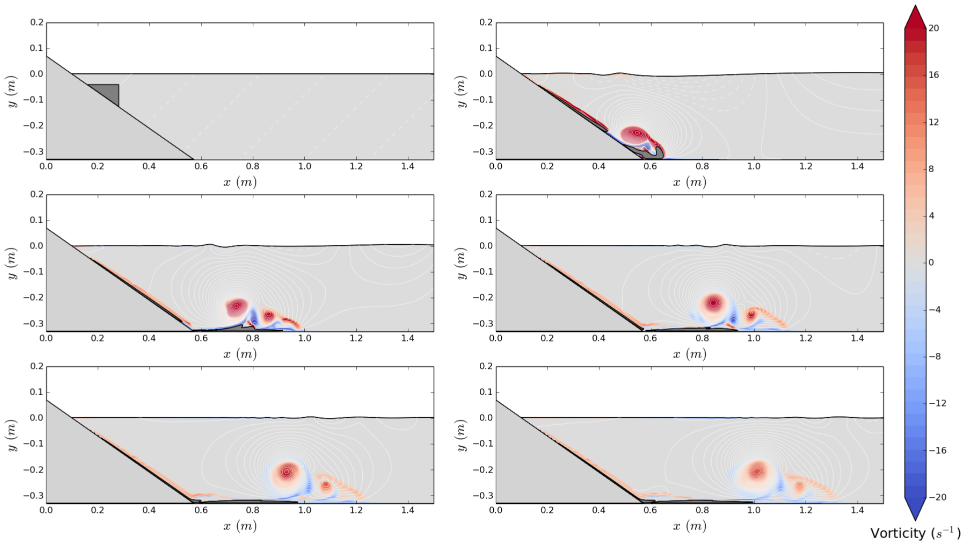

Figure 4.13: Slide snapshots with stream contour (white) and water coloured with vorticity, $1\,s$ between two snapshots

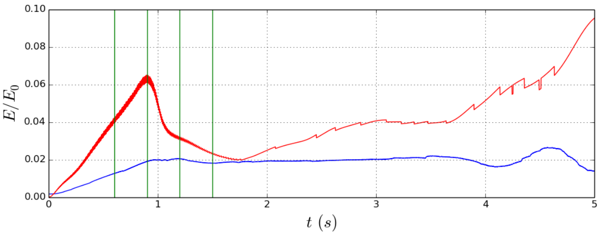

(a)

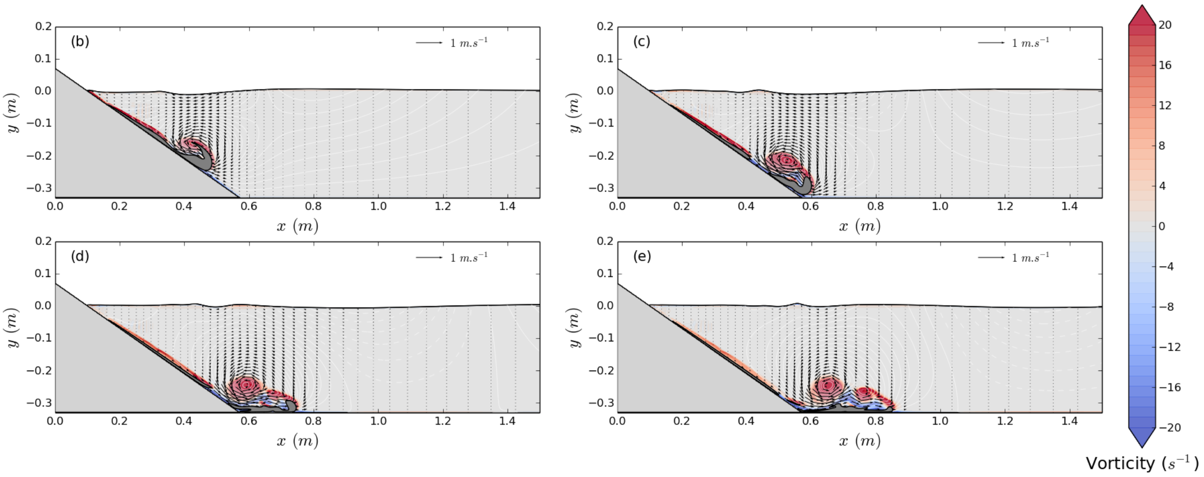

Figure 4.14: (a) Time evolution of the wave kinetic (red) and potential (blue) energy with the green lines representing the times at which the fourth following snapshots were taken. (b-e) Slide snapshots with black arrows representing the velocity field at times $t = 0.6, 0.9, 1.2, 1.5\,s$

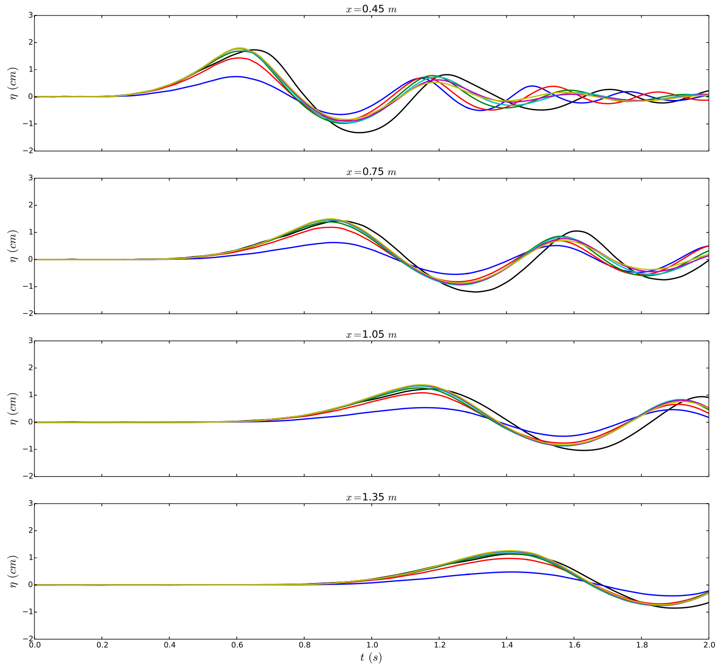

Figure 4.15: Elevation of the free surface for the Viroulet's experiment (black line), THETIS simulation with the slide viscosity at $\mu = 10\,Pa.s$ stopped at $t = 0.2\,s$ (blue line), $0.3\,s$ (red line), $0.4\,s$ (green line), $0.5\,s$ (cyan line), $0.6\,s$ (magenta line), $0.7\,s$ (yellow line)

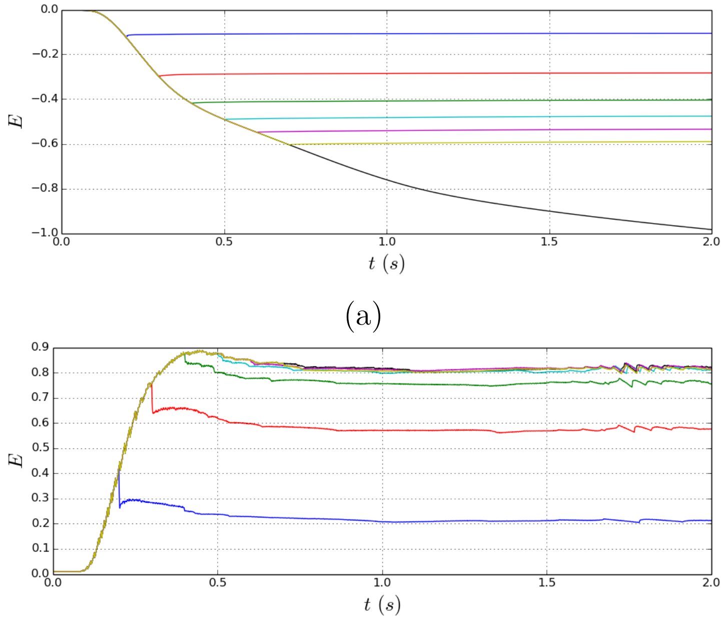

(a)

(b)

Figure 4.16: Time evolution of computed energy transferred by the slide (a) and wave energy (b) with the slide stopped at $t = 0.2\,s$ (blue line), $0.3\,s$ (red line), $0.4\,s$ (green line), $0.5\,s$ (cyan line), $0.6\,s$ (magenta line), $0.7\,s$ (yellow line) and not stopped (black line)

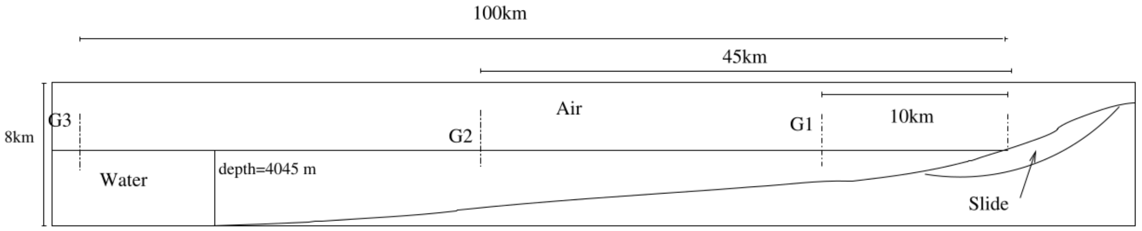

Figure 4.17: Cross section of the $80\,km^3$ La Palma slide scenario considered in Abadie et al. [1]

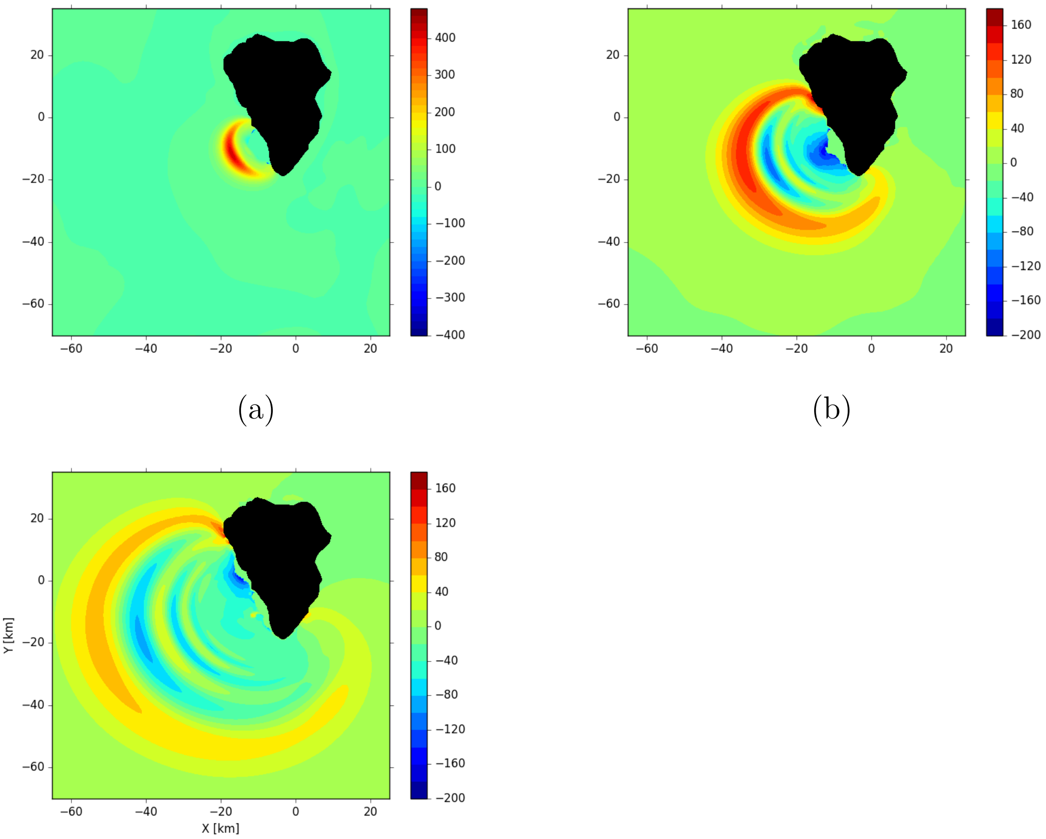

(a)

(b)

(c)

Figure 4.18: THETIS 3D computations for $80\,km^3$ slide volume. Contours of wavefield at t = (a) 102 s, (b) 230 s, (c) 342 s. Slide viscosity $2. * 10^7$ Pa.s

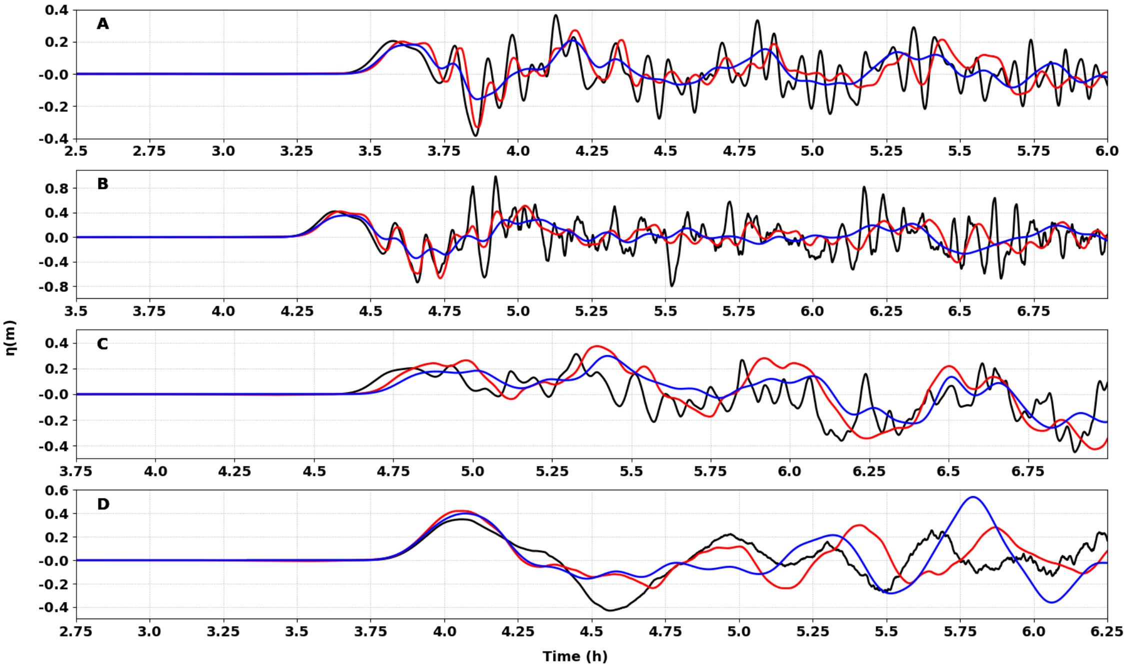

Figure 4.19: Surface elevations for the 80 km^3 scenario at Gauge 3 in the continental shelf of the Bay of Biscay (A), Gauge 4 in south Bretagne (B), Gauge 5 in the Gironde estuary (C) and Gauge 6 in Saint-Jean-de-Luz (D), computed by Calypso (black), FUNWAVE-TVD (red) and Telemac-2D (blue). The time takes into account the 20 first minutes of the slide and tsunami generation.

CHAPTER

FIVE

PYROCLASTIC FLOW: MODEL VALIDATION

Contents

5.1 Introduction

In the framework of the RAVEX project, experiments of wave generation by fluidized granular slide are intended. Following the work of Roche et al. [79] and presented in Section 1.4, the model which seems to be appropriate to pyroclastic flow is the Newtonian fluid with low viscosity.

First, in order to validate THETIS on wave generation by a fluid slide, water/water simulations based on experiments are carried out. Following these simulations, energy transfers are computed to ensure the possibility to model a pyroclastic flow as a Newtonian fluid.

This work is preliminary to further simulations on wave generation by fluidised granular flows.

5.2 Experimental and numerical setup

5.2.1 Experimental setup

The experiments consist in releasing a volume of water retained in a reservoir on an incline in a tank filled with still water up to a defined depth. These experiments have been realised in a tank by Yves Le Guer and his students in the framework of the RAVEX project. The dimension of the tank are $3.31\,m \times 0.6\,m \times 0.08\,m$ with two inclines at the left and right of the tank. The water volume in the reservoir is defined by a water height in reservoir h_r for the 2D simulations. The gate closing the reservoir is opened at a height h_g. Initially, the reservoir has been built for granular experiment and is therefore not totally waterproof. This can lead to water leak from the reservoir, hence some uncertainty on the water volume released at the gate opening and generation of ripples at the free surface before the gate opening. The slope angle is fixed to 30°.

5.2.2 Numerical setup

The 2D numerical geometry reproduces the exact geometry of the tank, namely 2 inclines and the reservoir (Figure 3.12)).

Mesh

The mesh is refined in the zone of interest, namely near the incline and the free surface. The domain is rectangular and numerical obstacles are used to define the left and right inclines as well as the wall of the reservoir (in red on Figure 5.1). The gate is not represented as it is considered to open at time $t = 0\,s$. The opening height of the gate is controlled by the size of the obstacle. The bottom part of the domain, from the top of the left incline, has a constant mesh size of $dx = 0.004\,mm$ and $dy = 0.001\,mm$. The top part keeps the same space step in x-direction but the cells are exponentially elongated in the y-direction. All the conditions on domain boundaries are set to symmetry except the bottom part, set to wall (see Section 2.2).

Figure 5.1: Picture of the numerical domain reproducing the experimental tank with two inclines and the reservoir

Numerical methods

The projection method is chosen for the resolution of pressure-velocity coupling. Because the free surface is highly perturbed at impact and droplets are generated, the VOF-TVD scheme is privileged for these simulations.

5.2.3 Studied cases

Four cases have been chosen for the validation which involve two masses of water in the reservoir and two water depths. The water mass is translated in terms of water height h_r in the reservoir (Figure 5.2). The parameters for each case is summarised in Table 5.1. The experimental system does not allow to control precisely the opening height of the gate, this height h_g have been mesured after each experiment and may vary from one case to another.

	slide mass (kg)	h_r (m)	h_w (m)	h_g (m)
expe 1	0.5	0.1	0.2	0.09
expe 2	0.5	0.1	0.1	0.10
expe 3	1	0.18	0.2	0.09
expe 4	1	0.18	0.1	0.12

Table 5.1: Parameters of the validation cases for the experiments and the numerical simulation

5.2.4 Experimental and numerical data

Experimental data

Experiments have been videotaped with an iPhone camera. A grid (dimension of a square: $0.052 \times 0.052\, m^2$) has been placed at the back of the tank in order to mesure the wave heights. Videos of the water on the incline have also been taken in order to study the dynamics of the slide (thickness and velocity). From videos of the waves and the incline, spatio-temporal pictures are made at fictitious gauges (Figure 5.2): several gauges normal to the incline mesuring the evolution of the slide thickness (SG1-3), one parallel to the incline (SG0) and several normal to the free surface at rest (WG1-3). The water in the reservoir, hereafter also called slide, has been colored with fluorescein in order to distinguish it from the water initially at rest in the tank and observe the behaviour of the slide at impact with still water. The diffusion coefficient of fluorescein is low ($0.436e^{-9}\, m^2.s^{-1}$, Petrášek & Schwille [75]), but due to quick mixing of slide and tank water after the impact, the color water does not represent the location of slide water only in the tank. This is important to precise because in the numerical simulations, the reservoir and tank fluids are considered non-miscible.

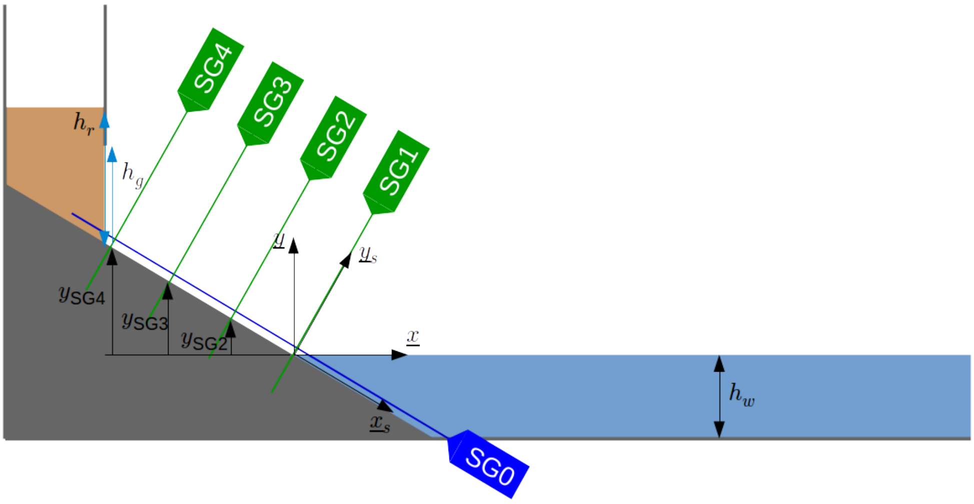

Figure 5.2: Sketch of the gauges: SG slide gauges and WG wave gauges

Numerical data

As previously mentioned, the simulations are realised with three fluids: water initially in the tank, slide fluid (initially in the reservoir) and air. These fluid are considered incompressible, Newtonian and non-miscible. The physical characteristics of slide fluid are the same as water. Same gauges as in experiments are used during the simulation (Figure 5.2). The waves gauges (WG) detects the water interface and the slide gauges (SG) detects the slide interface on the gauge lines. The positions of the gauges during the experiments and numerical simulations are summarised in Table 5.2. Two frames are defined to plot data: $(O, \underline{x}, \underline{y})$ and $(O, \underline{x_s}, \underline{y_s})$ are represented on Figure 5.2. Origin O is the position at the intersection of the free surface and the slope. The frame $(O, \underline{x}, \underline{y})$ is located so as to have the x-direction along the free surface. The frame $(O, \underline{x_s}, \underline{y_s})$ is placed with $\underline{x_s}$-vector along the slope pointing downwards.

	SG1	SG2	SG3	SG4	WG1	WG2	WG3
$y\,(m)$	0.0	0.05	0.1	0.15			
$x\,(m)$					0.5	0.8	1.1

Table 5.2: Gauges placement for water elevation (SW) and slide interface position (SG)

Numerical and experimental results are compared and analysed in the next sections.

5.3 Numerical results

5.3.1 Wave elevation

The Figures 5.3 to 5.6 show comparisons of waves generated by slide at three gauges for the four experiments presented in Table 5.1.

Measurement uncertainty due to by the video system depends on the position of the camera with respect to the free surface inducing parallax error. This uncertainty has been evaluated by measuring the thickness of the free surface on pictures and can be found in Table 5.3. For wave height measurement, the error on experimental amplitude is assessed from these values.

As in the subaerial case of Chapter 4, a first wave is generated followed by a second and a wave train that is more or less clearly defined depending on the case and the gauge.

The first wave amplitude obtained from experiments and simulations are summarized in Table 5.4. Errors are particularly important on the second experiment which corresponds to the lowest reservoir height and water depth.

	expe 1	expe 2	expe 3	expe 4
Free surface thickness (m)	0.004	0.008	0.003	0.01

Table 5.3: Evaluation of the free surface thickness on experimental pictures

5.3.2 Slide dynamics

Importance of slide thickness and slide velocity have been highlighted in wave generation process by numerous studies (Section 1.1.2). For this reason, comparison of slide dynamics between experiments and simulations have been realised on experiments 2 and 4. The slide thickness is plotted along the axis y_s normal to the slope (Figure 5.2).

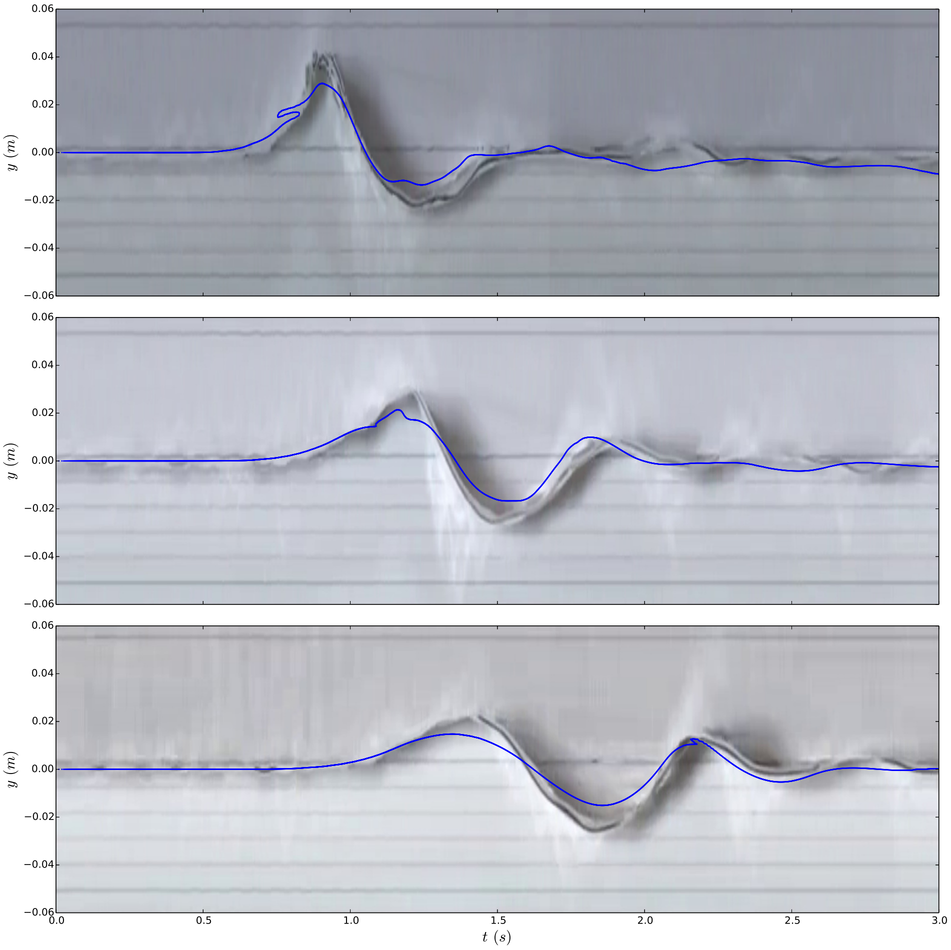

Figure 5.3: Wave elevation at gauges WG1 to WG3, experiment 1: comparison between experiment (picture) and simulation (blue points)

	WG1			WG2			WG3		
	$y_{sim}\ (m)$	$y_{exp}\ (m)$	ϵ_{rel}	$y_{sim}\ (m)$	$y_{exp}\ (m)$	ϵ_{rel}	$y_{sim}\ (m)$	$y_{exp}\ (m)$	ϵ_{rel}
Expe 1	0.029	0.036	-0.19	0.021	0.028	-0.25	0.015	0.022	-0.32
Expe 2	0.031	0.049	-0.37	0.024	0.042	-0.43	0.021	0.034	-0.38
Expe 3	0.058	0.062	-0.06	0.055	0.056	-0.02	0.045	0.051	-0.12
Expe 4	0.072	0.076	-0.05	0.057	0.067	-0.15	0.043	0.061	-0.29

Table 5.4: Error on first wave amplitude $\epsilon_{rel} = (y_{sim} - y_{exp})/y_{exp}$ with y_{sim} and y_{exp} respectively the numerical and experimental first wave amplitudes

Slide thickness

The time of gate opening in experiment is not known on experimental spatio-temporal pictures but begin all at the same time. Therefore, the numerical results on Figures 5.7 and 5.8) are superimposed on experimental results so that the slide fronts are at the same

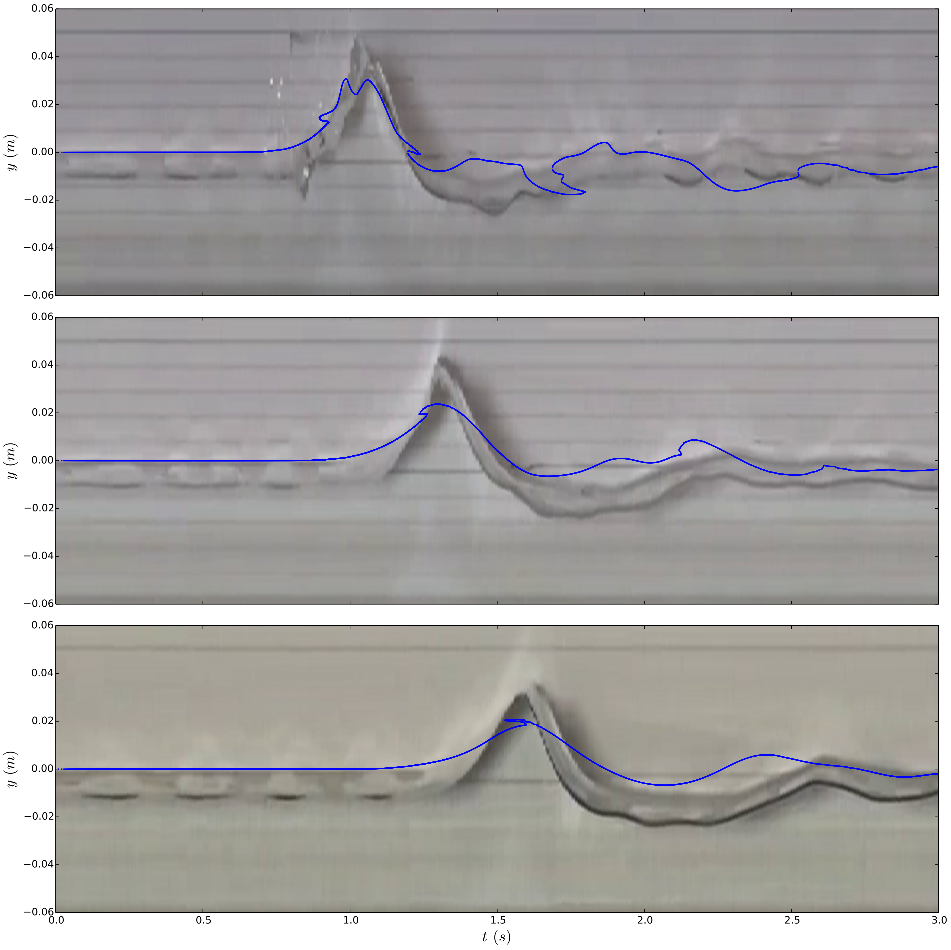

Figure 5.4: Wave elevation at gauges WG1 to WG3, experiment 2: comparison between experiment (picture) and simulation (blue points)

time at gauge SG5.

In both experiments and simulations, the evolution of slide thickness at a gauge is similar (Figures 5.7, 5.8): namely a steep slope to reach the maximum thickness and then a decrease. A thin tail is observed in simulations when the rear of the slide seems to stop more abruptly whereas the thickness is about $0.005\,m$ during experiments. The time it takes for all the slide to pass through a gauge is similar for the mass of $0.5\,kg$ (experiment 2) or $1.0\,kg$ (experiment 4) with about $0.6\,s$. The difference of volume is observed in the difference of maximum thickness with $0.02\,m$ and $0.04\,m$ for experiments 2 and 4 respectively at gauge SG4. The simulation reproduces quite well the slide thickness of experiment 2 whereas thickness is underestimated in simulation of experiment 4 with a maximum of $0.031\,m$ on gauge SG4. The delay of simulations on experiments which increases at each following gauge shows a lower velocity of the numerical slide compared to the experimental one. This difference of velocities is better highlighted by the gauge parallel to the slope and discussed in a further paragraph. However, this velocity difference

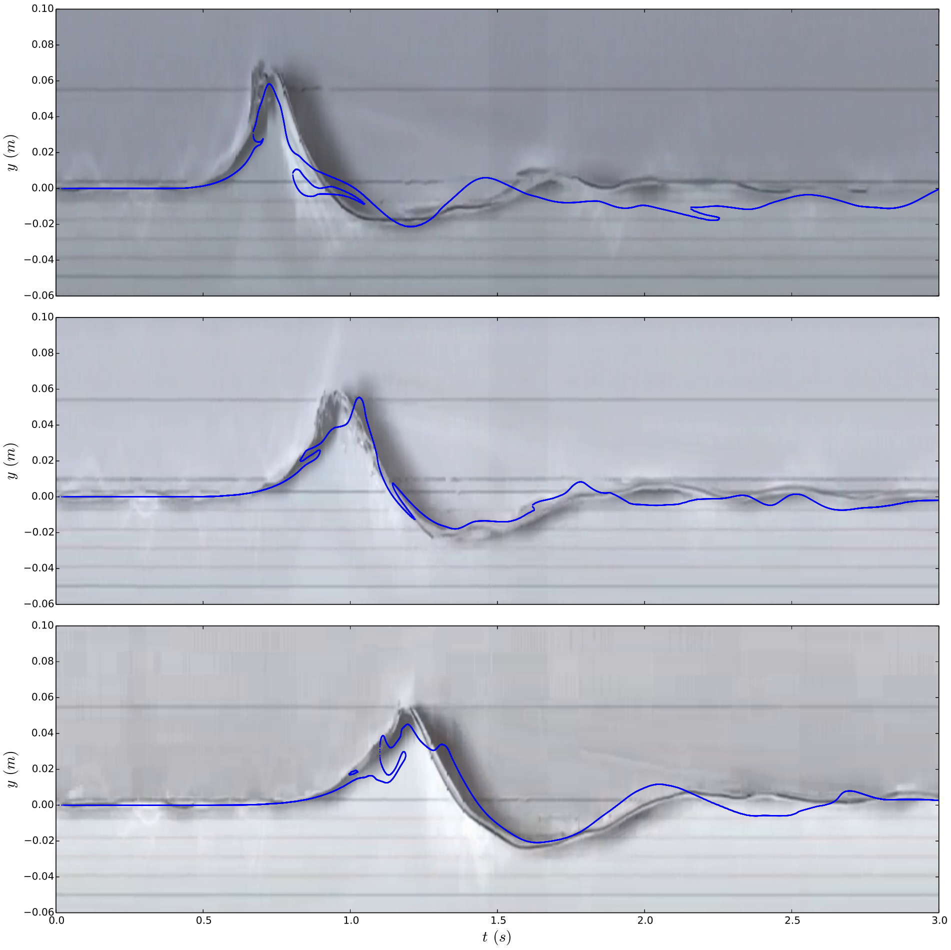

Figure 5.5: Wave elevation at gauges WG1 to WG3, experiment 3: comparison between experiment (picture) and simulation (blue points)

seems more important on experiment 2 than experiment 4.

Figure 5.9 shows the evolution of the slide thickness (i.e. the maximum distance between top and bottom part of the slide) at four gauges for simulations on the four experimental setups. Slide thickness seems maximum in the top part of the slope and then decreases to finally reach a stable value. At SG1, slides with the same initial volume reaches water with a similar thickness of about 0.02 m and 0.03 m for experiments 1-2 and 3-4 respectively. Reaching water does not seem to affect the thickness of the slide except the thin tail which tends to disappear.

Slide velocity

The gauge placed parallel to the slope allows to follow the front and rear of the slide interface. Figure 5.10 shows a comparison between experiments and simulations for setup 2 and 4. As previously mentioned, the gate opening was not precisely located in time in the experiments. Therefore, the numerical results are superimposed so that the front of

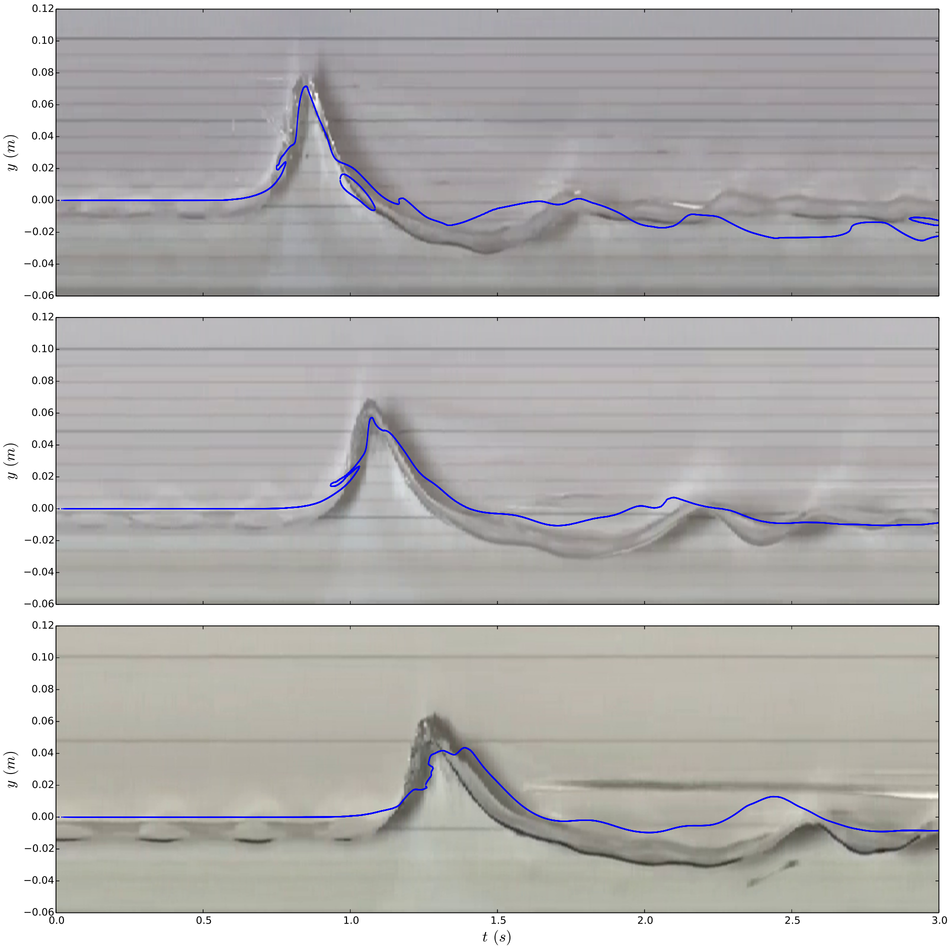

Figure 5.6: Wave elevation at gauges WG1 to WG3, experiment 4: comparison between experiment (picture) and simulation (blue points)

the slide coincides with the front of the experiment when it first appears on the picture. The difference of velocity between numerical and experimental results is also clearly seen on this figure, the numerical slide front reaching water with a delay. It is also observed that for both experiments, the slide front reaches water at about the same time when simulation of experiment 2 seems slower than for setup 4. Impact velocities have been evaluated from these plots. On Figure 5.10, the velocity at the impact for experiments 2 and 4 are evaluated by a linear fitting the slide front position near free surface. On Figure 5.11, the same have been realised before and after impact for numerical simulations on the four experiments. The velocities are summarized in Table 5.5. As observed on Figure 5.10, the velocity before impact evaluated on the experiments are similar for both volume of reservoir water, unlike velocities in simulutions which seem dependent on slide mass. The error on velocity before impact is of 34% and 52% for setup 4 and 2 respectively.

The velocity after impact in Table 5.5 corresponds to the slide velocity along the x_s-axis after entering water. The loss of velocity after impact is explained by the transfer

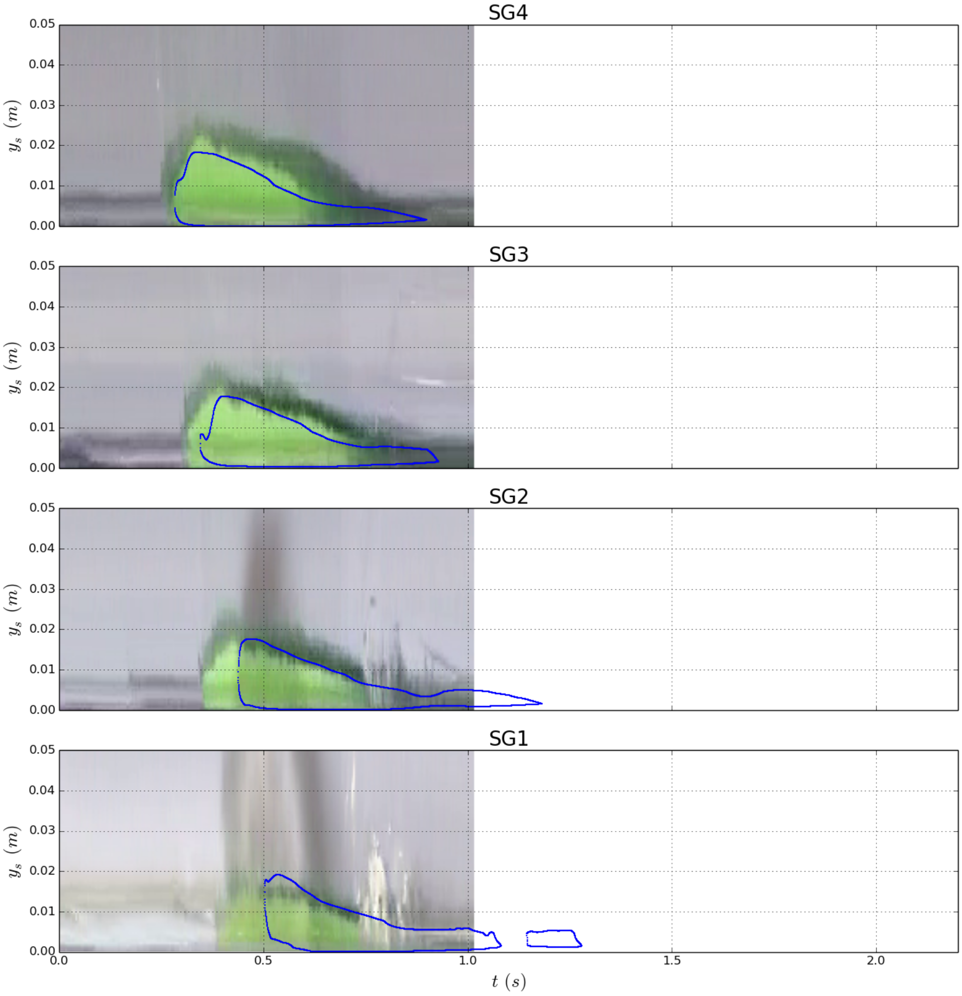

Figure 5.7: Slide contour detected by SG1 to SG4 for the setup 2, spatio-temporal picture of the experiment at the background and numerical results in blue

of kinetic energy to the tank water but also by the fact that the slide no longer moved only along the x_s axis from the moment it enters water. By comparing the four values of velocity after impact, it seems more dependent on the slide volume that on water depth. The loss of kinetic energy will be better illustrated in the next section.

From gauge SG0, the maximum distance of slide penetration into water can be evaluated. In order to be more relevant, the distance measured on the x_s-axis is converted into a minimum depth y_{min} on the principal frame (O, x, y). Minimum depth evaluation from videos of experiments 1 and 3 and from numerical gauge SG0 are summarised in Table 5.5. Numerical slide penetrates less into water than in experimental observations. This may be linked to velocity errors previously mentioned.

Despite velocity and thickness errors, numerical simulations for slide mass of $1\,kg$ are able to reproduce quite accurately the waves generated. This will be discussed after the analyse of energy transfers.

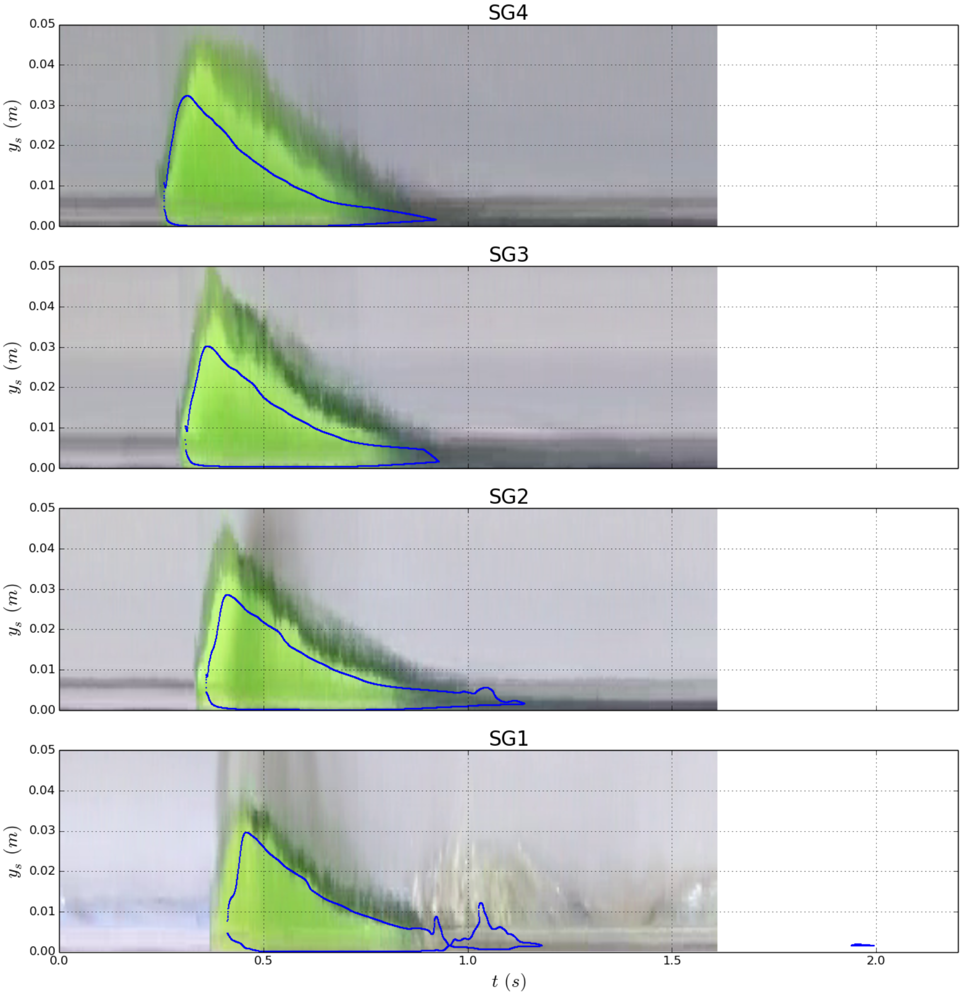

Figure 5.8: Slide contour detected by SG1 to SG4 for the setup 4, spatio-temporal picture of the experiment at the background and numerical results in blue

	$V_{s,e}^-$	$V_{s,n}^-$	$V_{s,n}^+$	$y_{min,e}$	$y_{min,n}$
expe 1		1.50	0.36	-0.11	-0.04
expe 2	2.84	1.36	0.28		-0.04
expe 3		1.80	0.50	-0.17	-0.11
expe 4	2.92	1.93	0.52		-0.09

Table 5.5: Estimated velocities of the slide front along the incline before the impact $V_{s,e}^-$ and $V_{s,n}^-$ (experimental and numerical) and after the impact $V_{s,n}^+$ (numerical) and maximum distance of slide penetration into water along x_s-axis converted to minimum depth $y_{min,e}$ and $y_{min,n}$ (experimental and numerical)

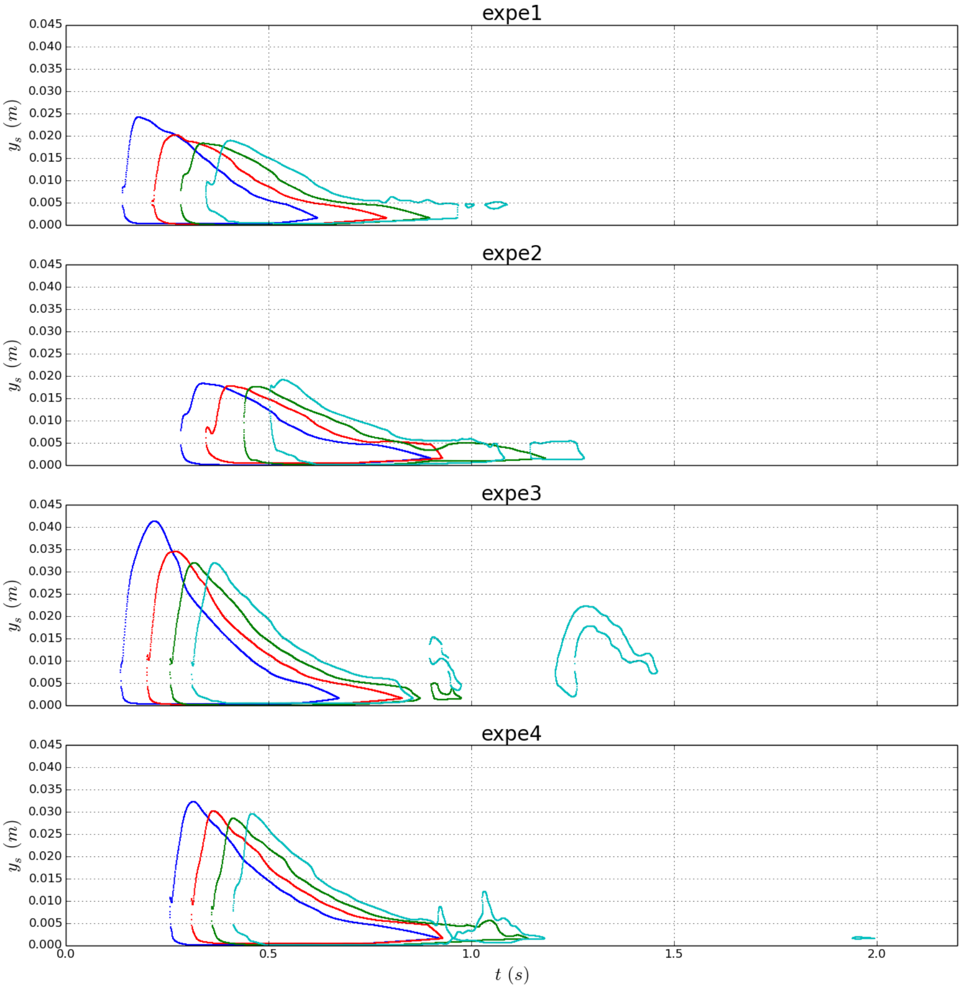

Figure 5.9: Slide contour detected by SG1 (cyan), SG2 (green), SG3 (red), SG4 (blue) for experimental setup 1 to 4

5.4 Energy transfers

Energy transfers are studied the same way as in the previous chapter (Section 4.2.3). Computation of energies are carried out on experiment 3 and plotted on Figure 4.14. Figure 4.14(a) shows energy loss in the system {air+water+slide} by numerical dissipation. With a maximum of nearly 4%, this loss is greater than in the previous studies. Figure 4.14(b) illustrates the evolution of slide energy. Unlike Viroulet's and Grilli's cases, slide kinetic energy is an important part of slide energy with a maximum of 60% of the initial slide energy. Viscous dissipation energy is very low because of the low viscosity of the fluid composing the slide, here water. Potential energy decreases until reaching an assymptotic value. This assymptotic value does not correspond to the deposition of the slide at the bottom of the tank as in subaerial and submarine cases of Chapter 4 where the slide density where greater than water density. In this case, the slide stays in motion

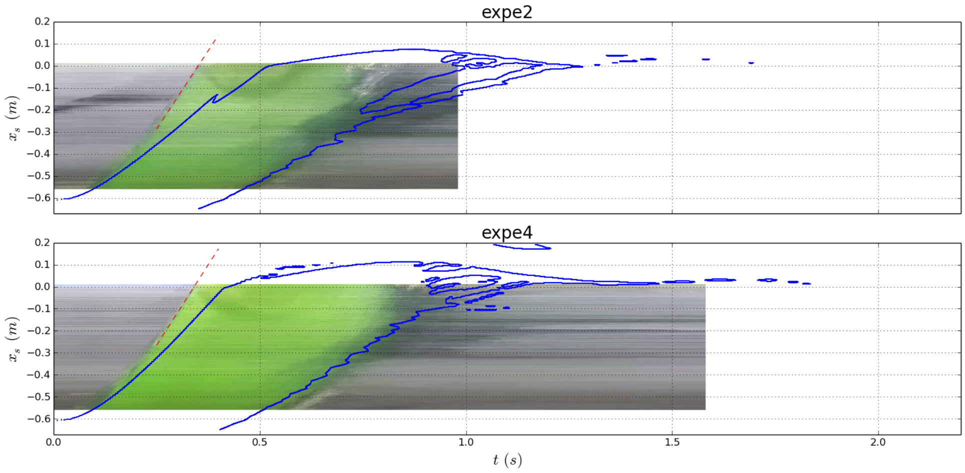

Figure 5.10: Slide contour detected by SG0 for experimental setup 2 and 4, spatio-temporal picture of the experiment at the background and in blue the numerical results, red discontinuous lines correspond to the linear fitting of the experimental slide front displacement before impact

in a zone close to the incline, explaining a kinetic energy low but not null at the end of the simulation.

Figure 4.14(c) shows the evolution of wave energy in the propagation zone as defined in Section 4.2.3. At the begining of the wave generation, this zone is difficult to define in particularly because of small slide drops which are separated from the main slide volume. For this reason, the evolution of wave energy might not be completely accurate just after the slide penetration into water. Moreover, the Froude number is around 1.3 at the impact, namely the case is supercritical. During the generation, the slide velocity is higher than the waves which explains the quick increase of wave energy after $t = 0.5\,s$ when the slide has slowed down.

Figure 4.14(d) illustrates the energy transferred from slide to wave and the total wave energy. Wave energy stabilizes around $t = 0.84\,s$, namely when all the slide is under water level (Figure 5.9). When wave energy reaches its maximum, the energy tranfer from slide to waves is about 19.4%. This value only decreases slightly to 18.5% at the end of the computation. This shows that the energy transfer from slide to wave only stops with slide energy transfer to water. However, energy transfer occurs quickly after slide penetration into water.

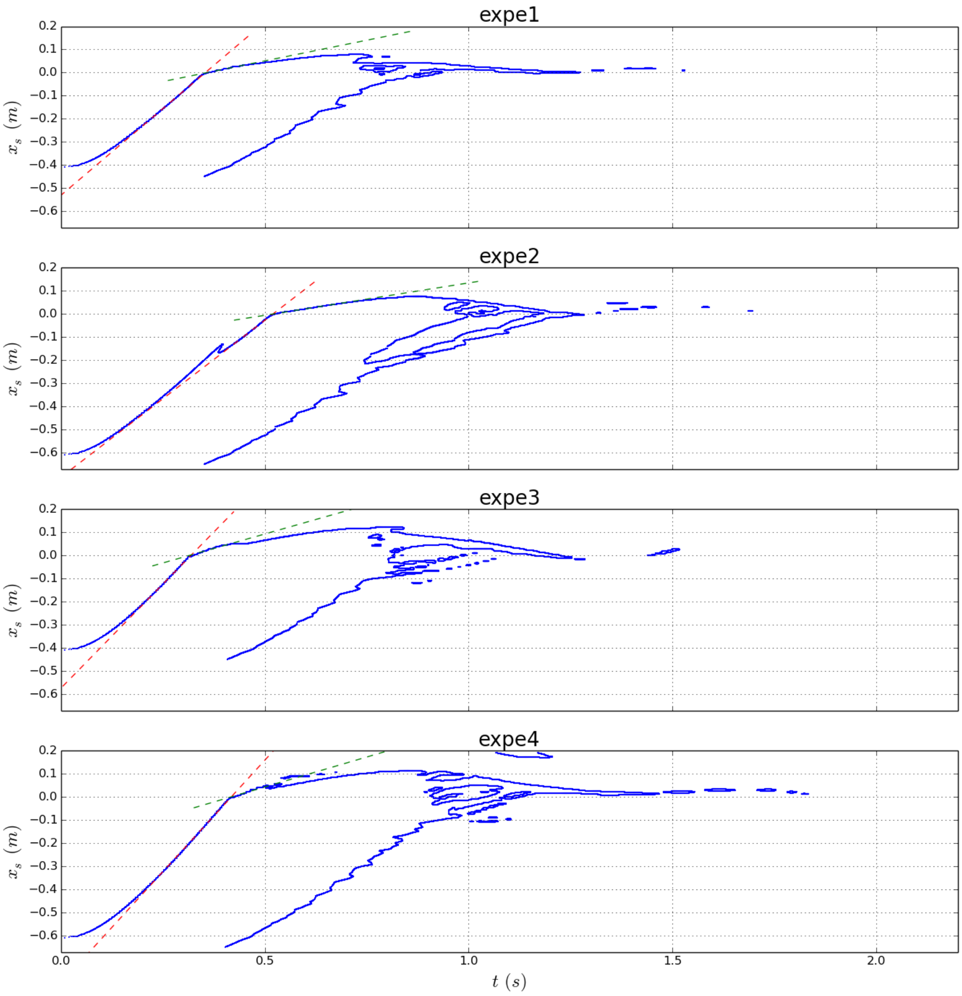

Figure 5.11: Slide contour detected by SG0 for experimental setup 1 to 4, red and green discontinuous lines correspond to the linear fitting of the slide front displacement respectively before and after the water penetration

5.5 Discussion

5.5.1 On slide velocity

The numerical results on experimental setup 1 and 2 are particularly deceiving. The first difference comes from the lower slide velocity found numerically. In order to test the influence of the obstacle resolution on slide motion, simulations have been realised with a slanted domain for which the incline is a domain boundary and is completely smooth (Figure 5.13). Contrary to Viroulet's experiment, the slide is quite thin (2 and 4 cm for cases 1-2 and 3-4 respectively) and reach a relatively high velocity (more than 2 $m.s^{-1}$) which makes the flow more difficult to solve. The slanted domain makes the slide motion easier to solve by THETIS but instabilities appear at the water free surface and highly

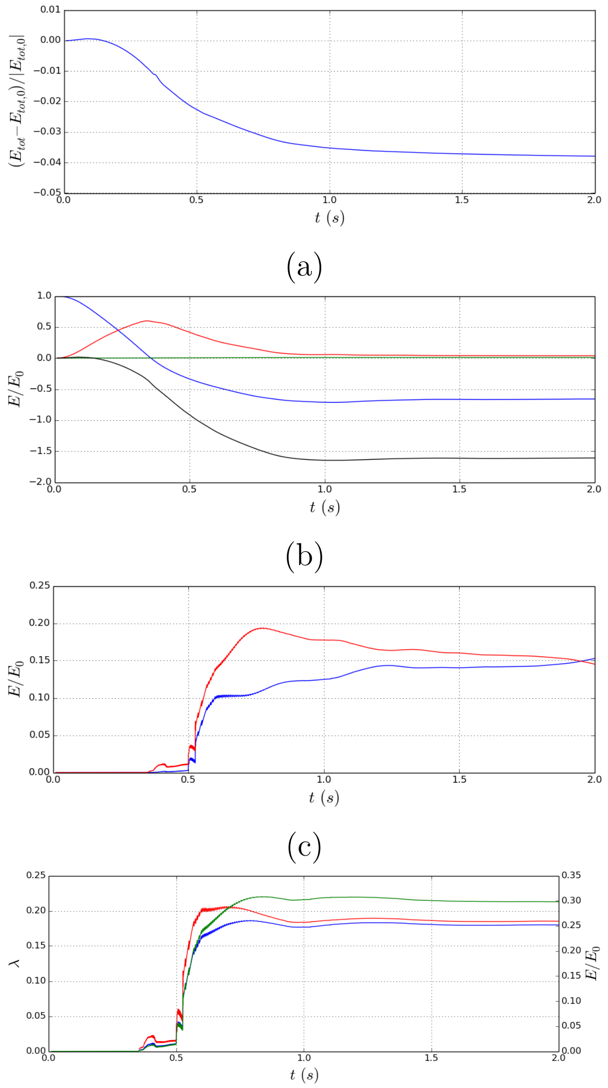

(a)

(b)

(c)

(d)

Figure 5.12: Time evolution of computed energy components in simulation of the third experiment (Viroulet et al. [87] with Newtonian slide ($\mu = 10\,Pa.s$)). (a) Relative error on system total energy {air+water+slide} (b) Slide potential energy (blue), kinetic energy (red) and energy dissipated (green), Energy transferred to water (black), divided by the initial slide mechanic energy E_0 (c) Wave potential energy (blue), kinetic energy (red) divided by E_0, (d) Evolution of the wave energy (green, right axis) divided by E_0, Transfer ratio (left axis) from Jiang and LeBlond from expression 4.13 (blue) and from expression 4.14 (red)

increase the computational time.

By comparing Figures 5.10 and 5.14, it can be remarked that the velocity before impact as been improved by the slanted domain reaching $2.17\,m.s^{-1}$ and $2.43\,m.s^{-1}$ for case 2 and 4 respectively, compared to previous numerical and experimental results in

Table 5.5. However, the slide thickness at gauges SG1 to SG4 is more important at the slide front than in previous simulations (Figure 5.15).

In terms of free surface elevation, it seems that improving the slide velocity has also enabled to reproduce more accurately the first wave amplitude (Figure 5.16). Simulations carried out with a mesh adapted to both the incline and the free surface could be a solution to improve the results and keep reasonable computational time.

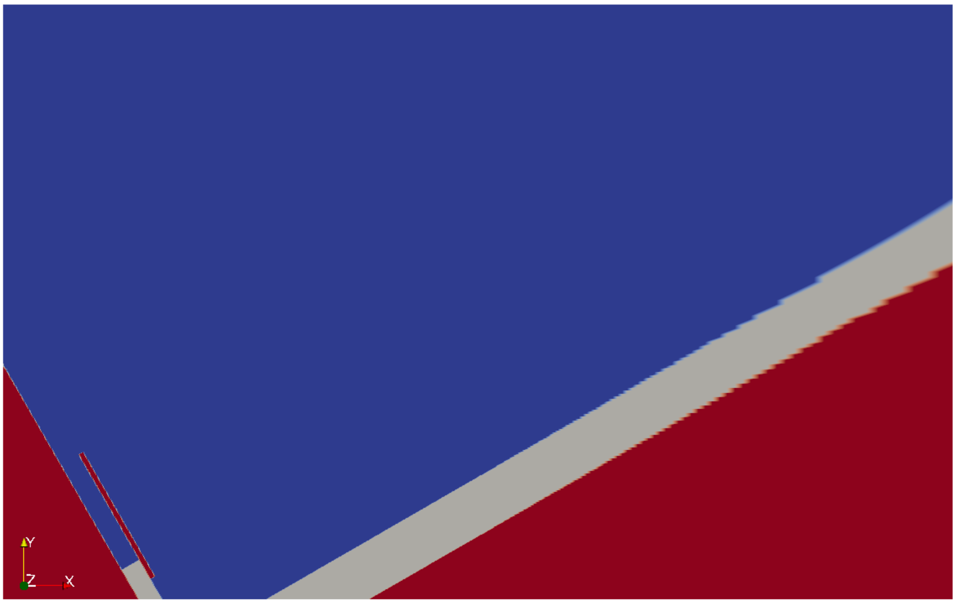

Figure 5.13: Slanted domain for fluid/fluid simulations

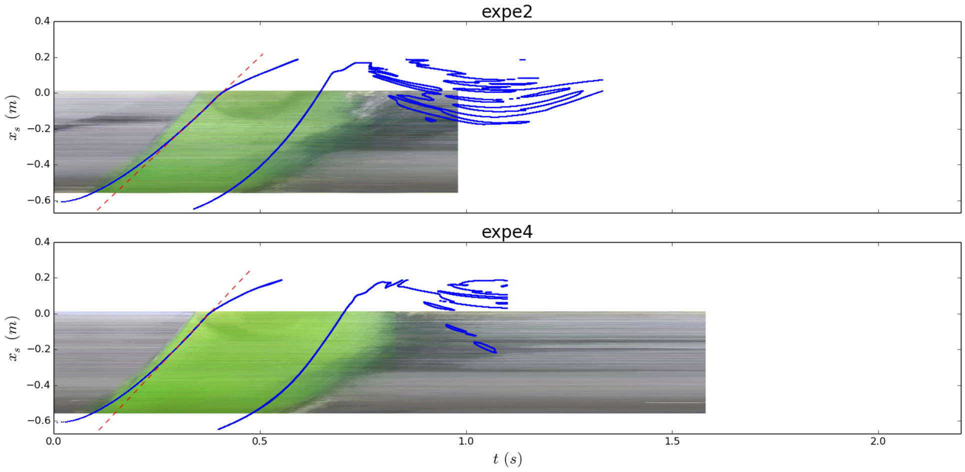

Figure 5.14: Slide contour detected by SG0 for experimental setup 2 and 4 with slanted domain, spatio-temporal picture of the experiment at the background and in blue the numerical results, red discontinuous lines correspond to the linear fitting of the numerical slide front displacement before impact

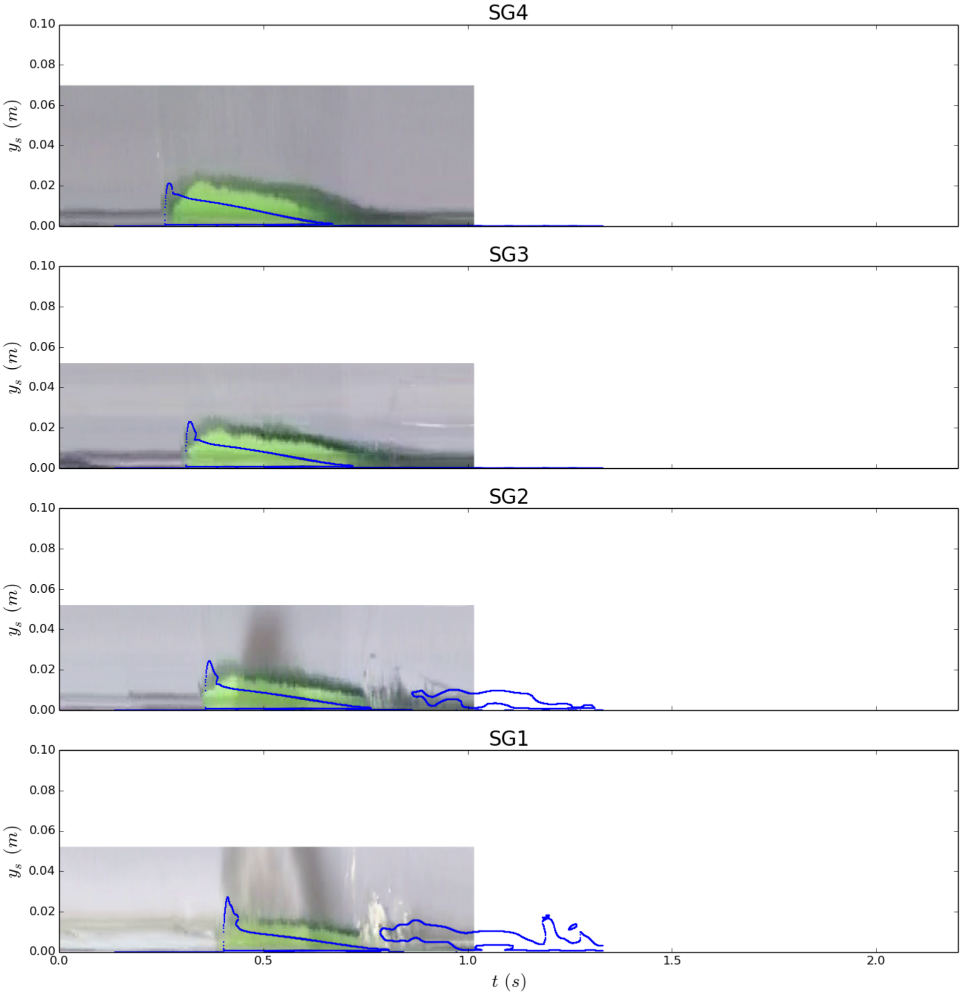

Figure 5.15: Slide contour detected by SG1 to SG4 for the setup 2 with slanted domain, spatio-temporal picture of the experiment at the background and numerical results in blue

5.5.2 Parameters influence

Simulations close to the third setup (i.e. $h_w = 0.2\,m$ and $h_r = 0.1\,m$) have been carried out in order to evaluate the influence of slide density, viscosity and gate opening height. The initial fluid is water with a gate opening height of $0.1\,m$. Three series of 5 simulations are carried out, changing one parameter at a time whose range can be found on Table 5.6.

Slide density

Slide density has an impact on wave amplitude: the denser the slide, the greater the wave amplitude (Figure 5.17). Density has a few influence on velocity before impact (Table 5.6) and no effect on slide thickness (Figure 5.18).

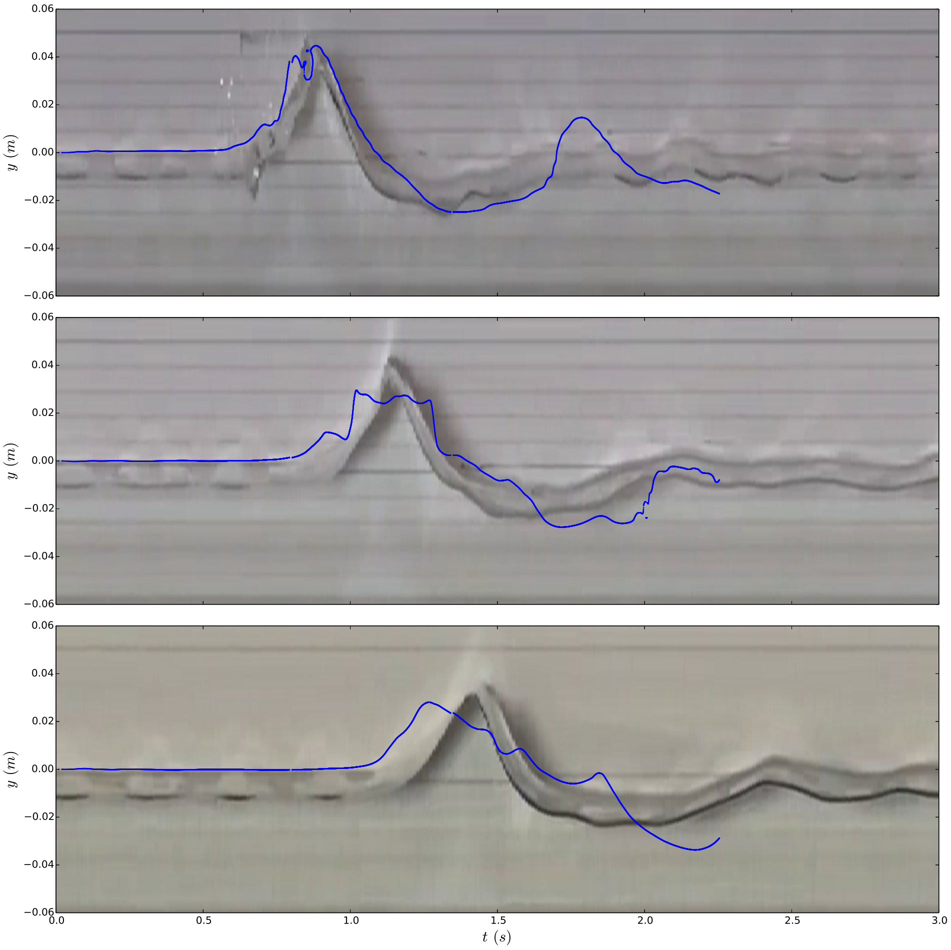

Figure 5.16: Wave elevation at gauges WG1 to WG3, experiment 2: comparison between experiment (picture) and simulation with slanted domain (blue points)

relative density d	0.6	0.8	1.0	1.2	1.4
$V_{s,n}^{-}\,(m.s^{-1})$	1.41	1.47	1.50	1.52	1.53
$\mu\,(Pa.s)$	0.001	0.01	0.1	1	10
$V_{s,n}^{-}\,(m.s^{-1})$	1.5	1.46	1.37	0.80	0.1
$h_g\,(m)$	0.02	0.04	0.06	0.08	0.1
$V_{s,n}^{-}\,(m.s^{-1})$	1.09	1.42	1.47	1.49	1.5

Table 5.6: Estimated velocities of the slide front along the incline before the impact $V_{s,n}^{-}$ for each series of simulations

Slide viscosity

For viscosity equal and greater than $1\,Pa.s$, the wave amplitude is highly reduced (Figure 5.19). Similarly to density variation, the viscosity does not seem to impact the slide thickness (Figure 5.20). However, velocity is highly reduced above a vicosity value of

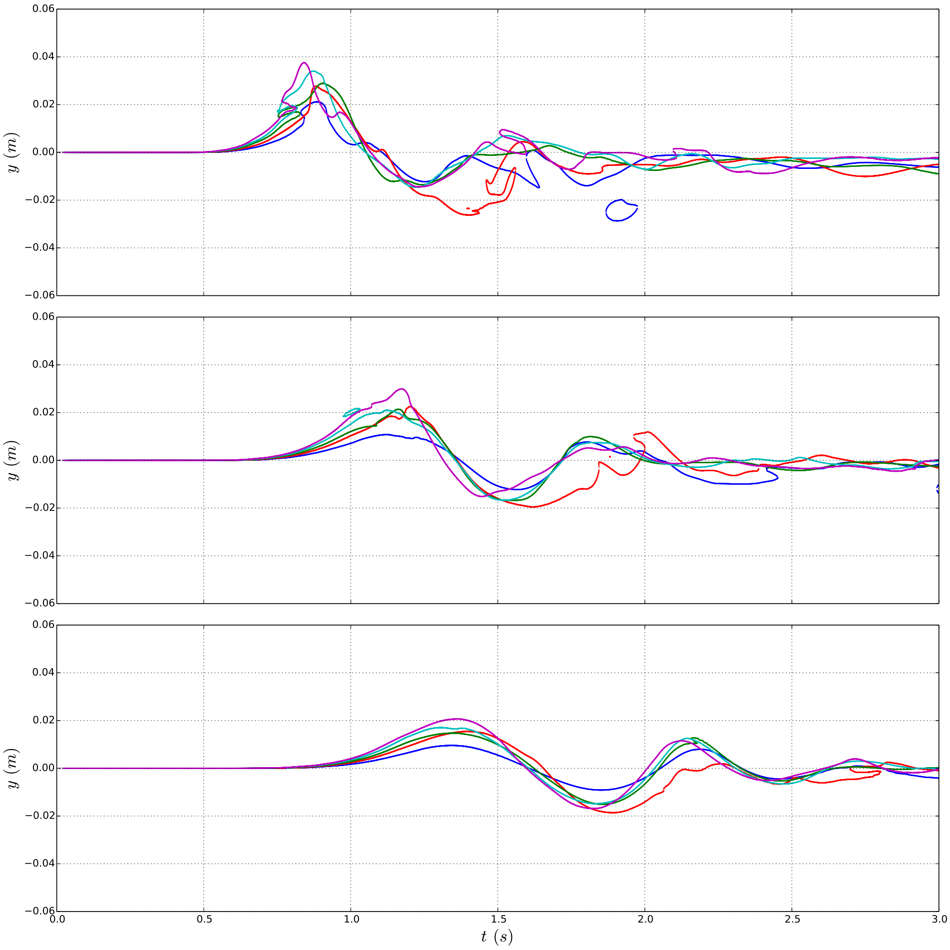

Figure 5.17: Wave elevation at gauges WG1 to WG3 for 5 relative density values: $d = 0.6$ (blue), $d = 0.8$ (red), $d = 1.0$ (green), $d = 1.2$ (cyan), $d = 1.4$ (magenta)

$1\,Pa.s$ (Table 5.6).

Gate opening height

Except for its lower value (i.e. $0.2\,m$), the gate opening height does not seem to have a large influence on wave amplitude. Indeed, only for this value, the slide thickness and impact relocity are reduced (Figure 5.22, Table 5.6).

5.5.3 Pyroclastic flow model

Following Roche et al. [79], a fluidized dense granular flow behaves like a water flow during a dam break except for the last stage. The simulations presented here are comparable to a dam break case. Energy transfer from slide to waves is achieved quite quickly after slide penetration into water. Therefore, considering that the dense granular flow stays fluidized during its motion along the incline, a pyroclastic flow could be modelled as a

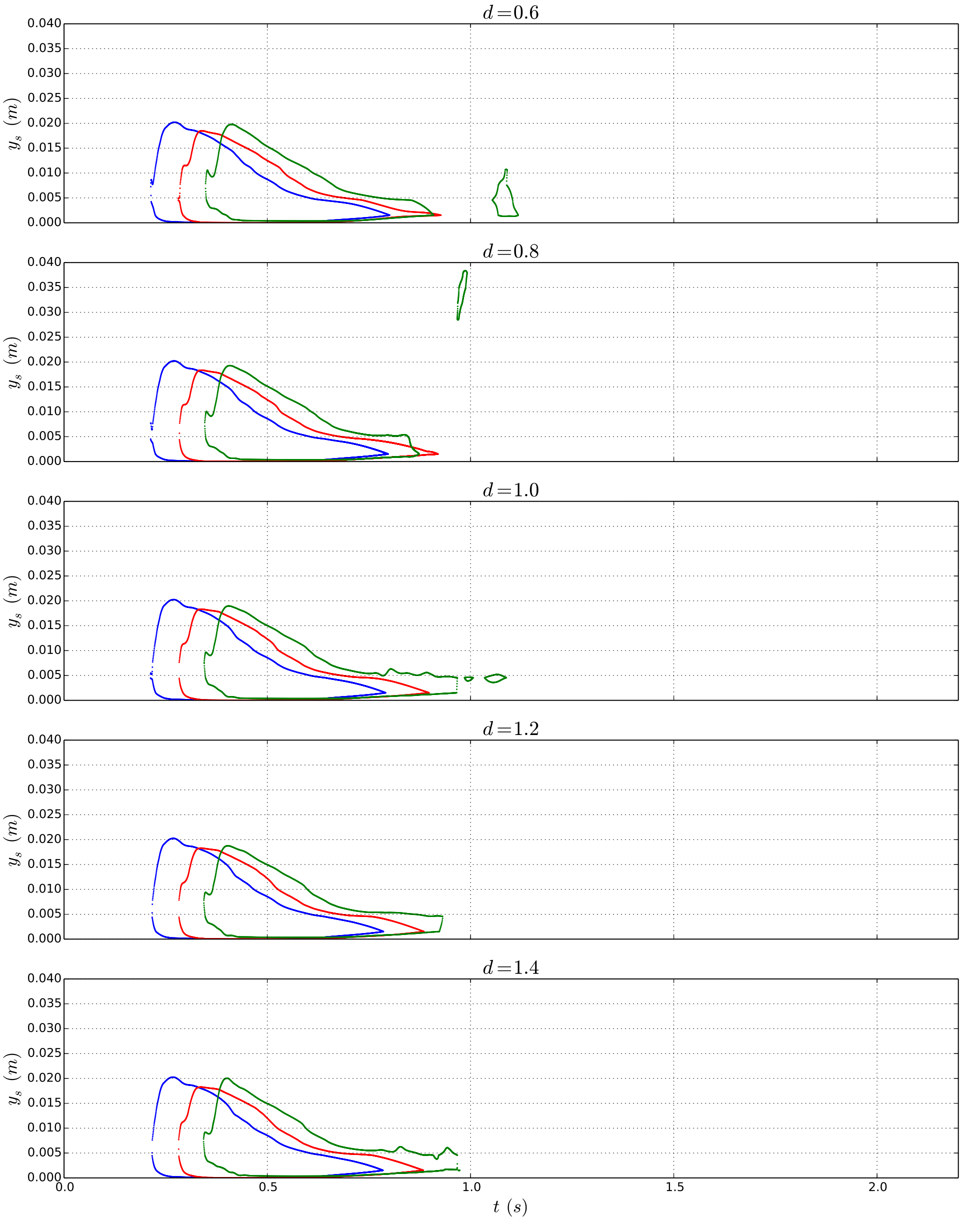

Figure 5.18: Slide contour detected by SG1 to SG3 for 5 relative density values

Newtonian fluid with low viscosity in order to reproduce wave generation.

5.6 Conclusion and perspectives

These simulations illustrate the difficulties of modelling subaerial slide impacting water with a quite high velocity, particularly for small slide volume and water depth. Using a good mesh is essential to solve accurately both the slide and the free surface elevation. THETIS mesh limitations make it more challenging to reach.

Nevertheless, based on our most accurate results, we show the quick conversion from

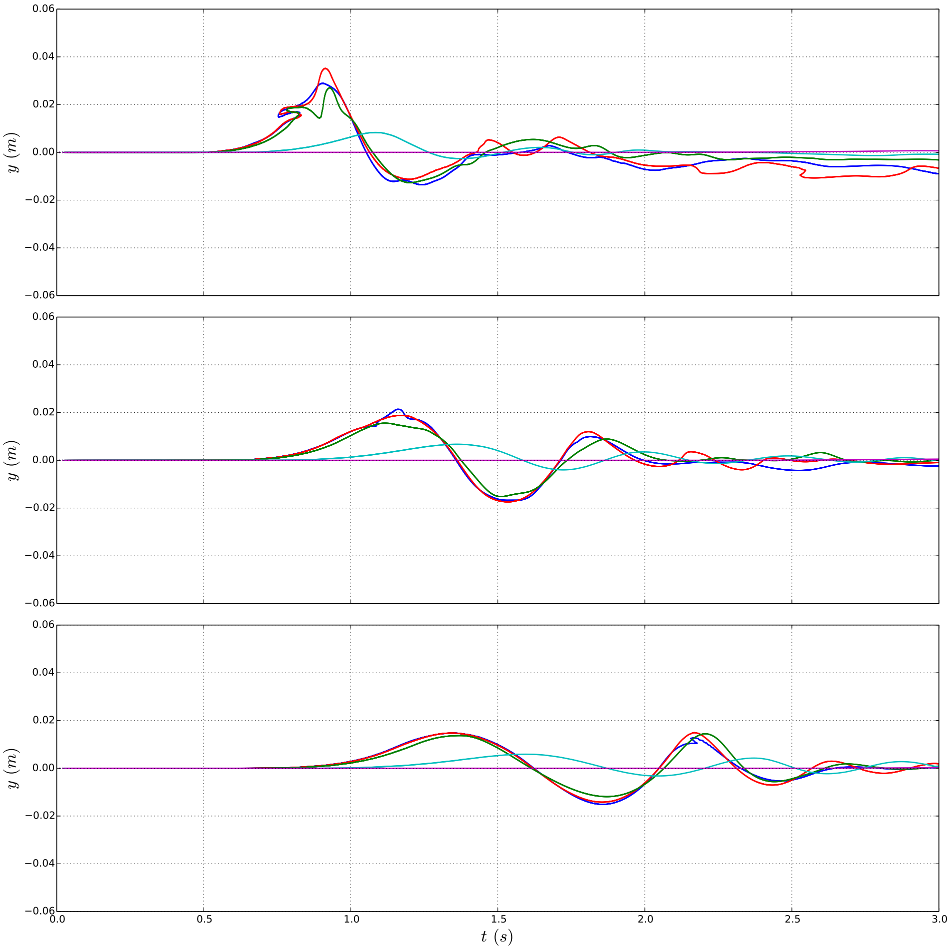

Figure 5.19: Wave elevation at gauges WG1 to WG3 for 5 viscosity values: $\mu = 0.001\,Pa.s$ (blue), $\mu = 0.01\,Pa.s$ (red), $\mu = 0.1\,Pa.s$ (green), $\mu = 1.0\,Pa.s$ (cyan), $\mu = 10.0\,Pa.s$ (magenta)

slide to wave energy ensuring the possiblity to model pyroclastic flow as a Newtonian fluid during wave generation simulations. This hypothesis will be verified with simulations on experiments realised in the framework of the RAVEX project.

From this work, a more in-depth study of the influence of parameters could be realised both experimentally and numerically. In addition to parameters discussed in this chapter, the slope angle and the temperature could be added.

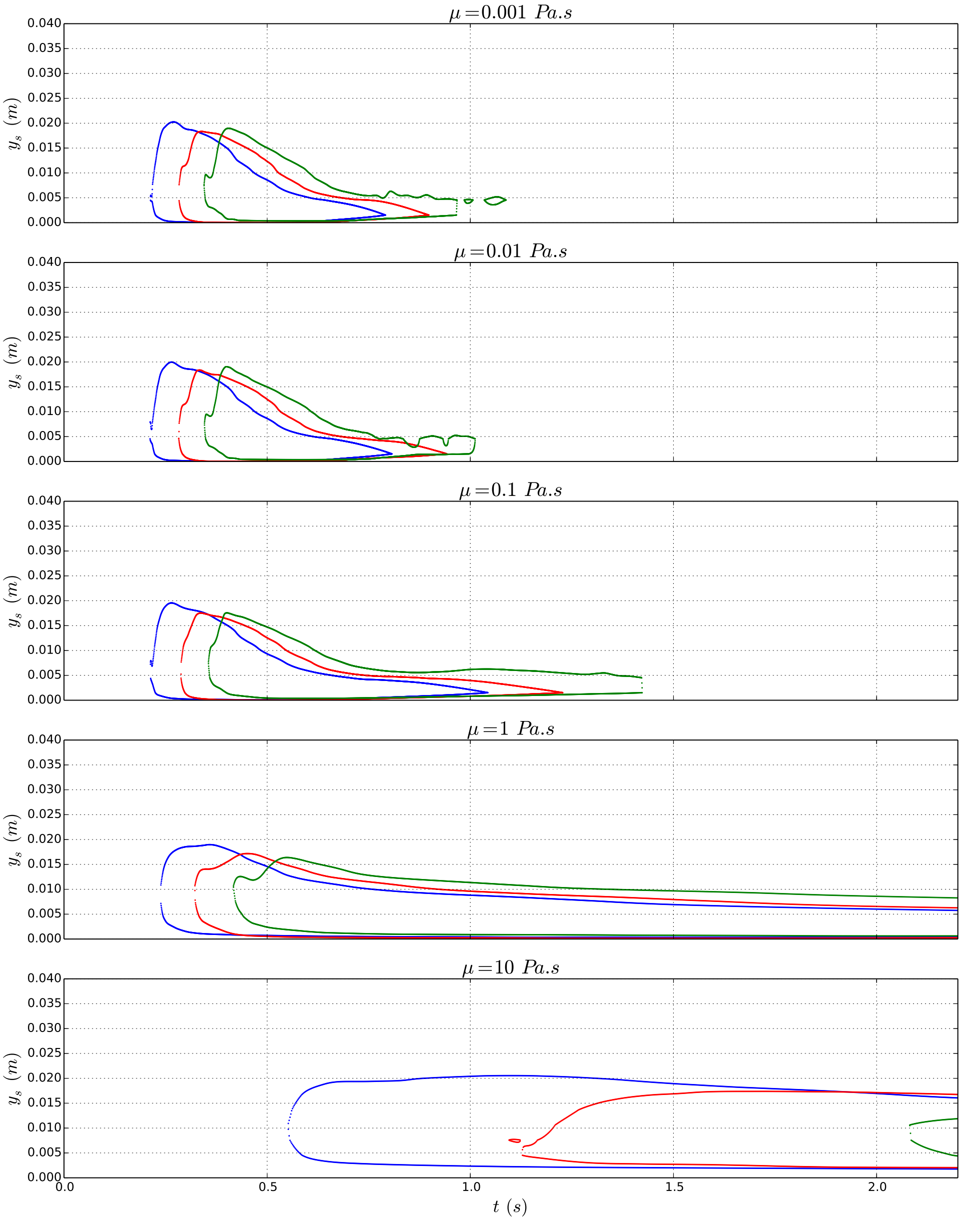

Figure 5.20: Slide contour detected by SG1 to SG3 for 5 viscosity values

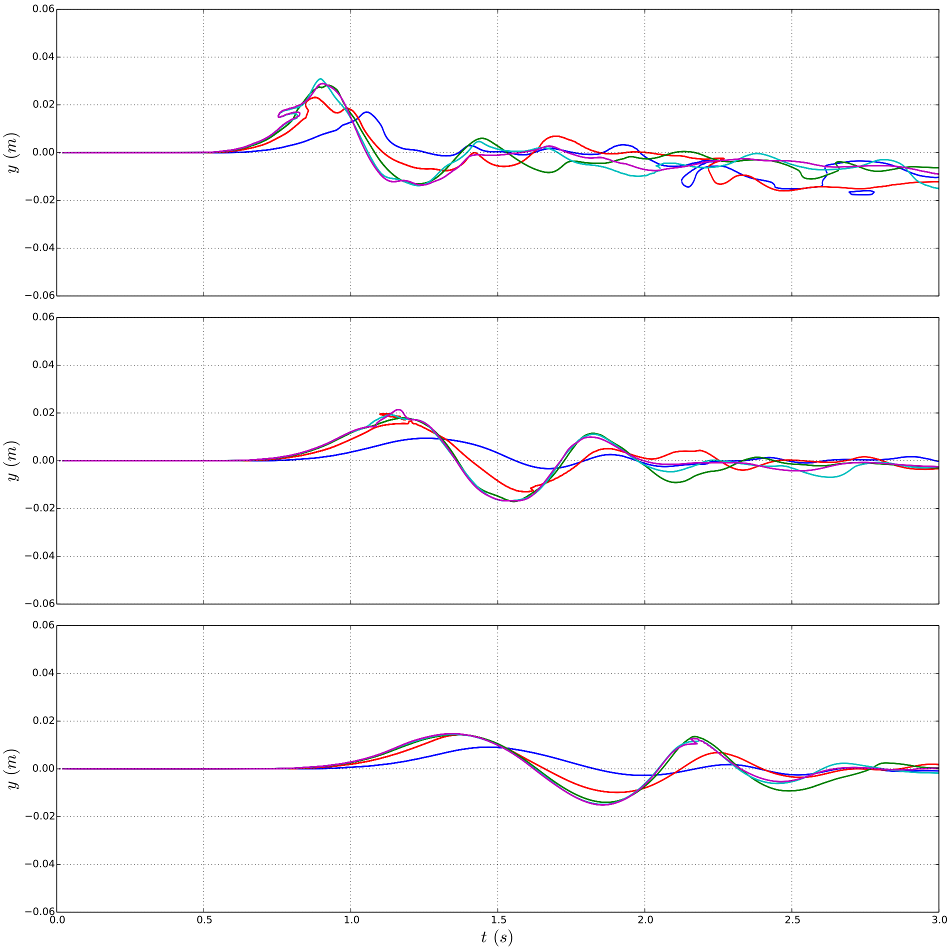

Figure 5.21: Wave elevation at gauges WG1 to WG3 for 5 gate opening heights: $h_g = 0.02\,m$ (blue), $\mu = 0.04\,m$ (red), $\mu = 0.06\,m$ (green), $\mu = 0.08\,m$ (cyan), $\mu = 0.1\,m$ (magenta)

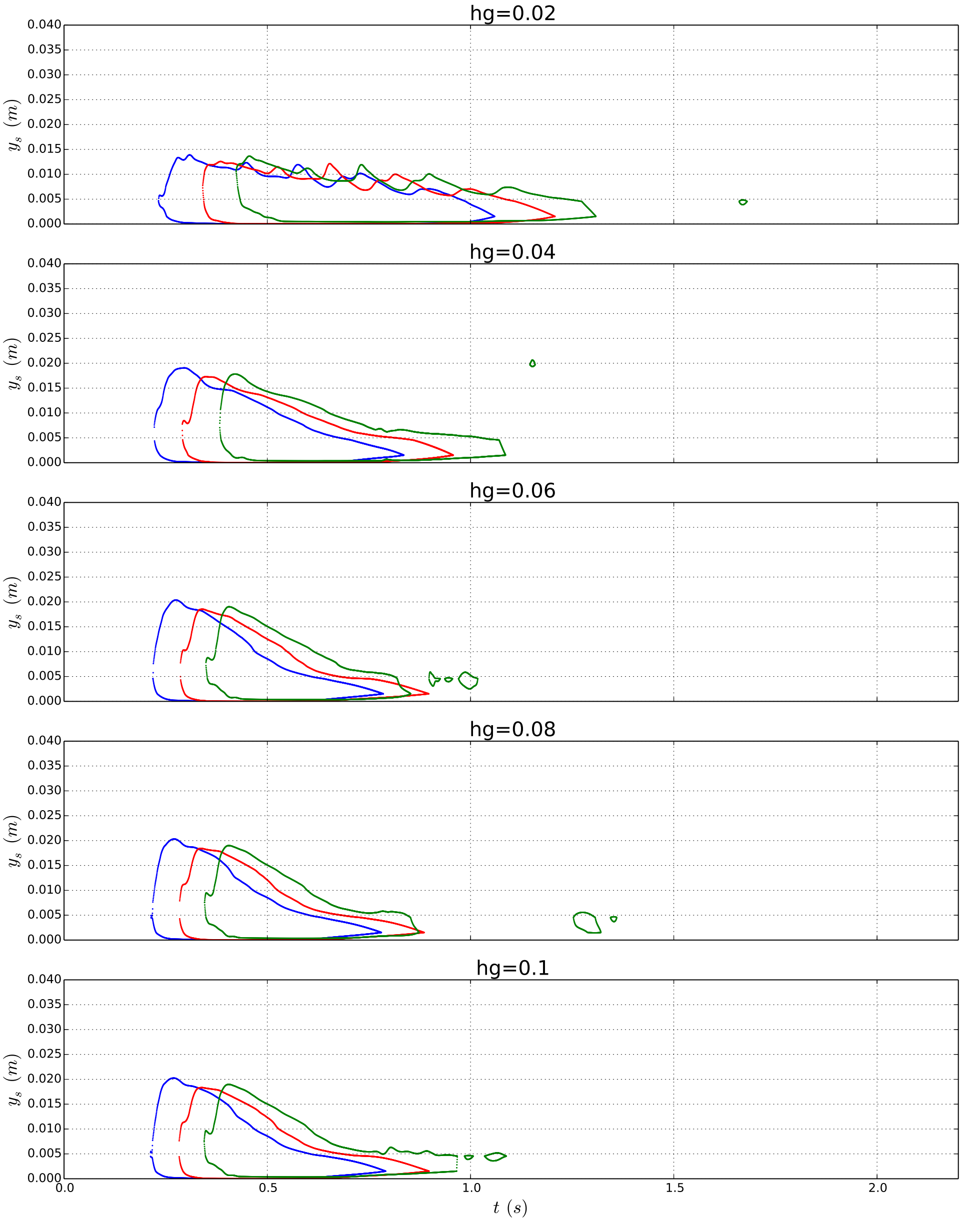

Figure 5.22: Slide contour detected by SG1 to SG3 for 5 gate opening heights

CONCLUSION AND PERSPECTIVES

This thesis have focused on two modelling approaches: first, modelling a landslide by discontinuous media by adding a method to solve solid collisions in a Navier-Stokes code and then modelling a landslide as a continuous media with an emphasis on energy transfers during the generation process. The principal results and the perpectives for future work are presented in this chapter.

On the discontinuous approach

A discontinuous model for landslides has been developped by adding a routine which manages solid/solid collisions to a Navier-Stokes code. In this model, a landslide is composed of discs made up of penalised fluid. Without the routine, these discs behave as solid blocks whose collisions are perfectly plastic. The routine enables to avoid plastic collisions, corrects the discs trajectories in order to follow a physical trajectory considering a collision with a restitution coefficient between 0 and 1. This routine has been tested in comparison with experimental results of cylinders and half-cylinders packs sliding on an incline in a tank filled with water. The simulations give moderatly successful results in terms of cylinder motion and wave amplitudes but this has to be modulated by the chaotic nature of the experiments performed.

In the continuity of this study, it would be interesting to validate the method on experiments less chaotic for example with less cylinders. These experiments are being prepared in the perspective to write an article presenting the method. Moreover, the routine could be improved to expand its possibilities. For instance, it could be possible to consider other geometries than the discs, to add interaction with fixed obstacles and boundaries or make the model more complex by adding friction between blocks. A model mixing continuous media (Newtonian fluid for instance) and solid blocks in order to take into account the difference of scale in real landslide blocks and their interaction could be imagined using this method. We could also apply this method on other applications than wave generation like predicting blocks motion composing a breakwater under wave impact.

On the continuous approach for granular slide

Two continuous models for subaerial and submarine slides have been tested: the Newtonian fluid and the $\mu(I)$-rheology. Both of these models give satisfactory results on wave amplitudes for subaerial slide. Moreover, it is possible to calibrate the Newtonian fluid with the $\mu(I)$-rheology following Ionescu et al. [44]. The use of $\mu(I)$-rheology for submarine slide has not been possible with THETIS. A study of energy transfer from slide to waves have be carried out, showing that the transfer is very quick after the penetration of the slide into water. The process is more efficient for subaerial slide than for submarine slide. Moreover, simulations showed that the wave train is a consequence of the first wave generation. Therefore, for wave generation purpose, the slide needs to be correctly model only during this short period of time. Following this work, new computations have been performed on the Cumbre Vieja Volcano case.

In the continuity of this work, it could be interesting to apply the energy transfer study on other subaerial or submarine cases and other slide models (Bingham fluid, discontinuous slide). The TANDEM project focused on the Cumbre Vieja case but the Newtonian model and $\mu(I)$-rheology can be applied on other real cases. By solving the initiation problem of $\mu(I)$-rheology underwater, this model could also be applied on submarine landslide.

On the continuous approach for pyroclastic flow

Simulations of water subaerial slide generating waves in a water-filled tank showed the complexity of solving these cases with THETIS. From the validated cases, the energy transfer from slide to water is, similarly to previous simulations with higher viscosity for the modelling of granular slide, done in a short period of time after the penetration of the slide into the water initially at rest. Litterature presents pyroclastic flow as a granular flow with high mobility close to a low viscosity fluid flow. These results of energy transfer during water/water experiments show that pyroclastic flow can be modelled as a low viscosity fluid during the wave generation process. Moreover, a preliminary parameter influence study has been realised on the slide density, viscosity and the gate opening height (which govern the slide penetration velocity magnitude). As expected the wave amplitude increases with the density and with decreasing viscosity values. Gate opening height has a low influence on the wave amplitude except for low values where the slide thickness and velocity are reduced.

This work is ongoing in the framework of the RAVEX project. Following the present study, simulations on the waves generated by fluidised granular slide with slide modelled as a Newtonian fluid are expected. Moreover, the parameter influence study can be used as a basis for a more in-depth study of the parameters both experimentally and numerically. These simulations would aim to calibrate a model of pyroclastic flow in order to be applied on the Montagne Pelée Volcano and assess the risk of tsunami generated by an explosive eruption on the coast potentially threatened.

BIBLIOGRAPHY

[1] Abadie, S., Harris, J., Grilli, S. & Fabre, R. [2012], 'Numerical modeling of tsunami waves generated by the flank collapse of the cumbre vieja volcano (la palma, canary islands): tsunami source and near field effects', *Journal of Geophysical Research: Oceans* **117**(C5).

[2] Abadie, S., Morichon, D., Grilli, S. & Glockner, S. [2010], 'Numerical simulation of waves generated by landslides using a multiple-fluid navier–stokes model', *Coastal engineering* **57**(9), 779–794.

[3] Angot, P. [1989], Contribution à l'étude des transferts thermiques dans des systèmes complexes: application aux composants électroniques, PhD thesis, Bordeaux 1.

[4] Ataie-Ashtiani, B. & Najafi-Jilani, A. [2008], 'Laboratory investigations on impulsive waves caused by underwater landslide', *Coastal Engineering* **55**(12), 989–1004.

[5] Ataie-Ashtiani, B. & Nik-Khah, A. [2008], 'Impulsive waves caused by subaerial landslides', *Environmental Fluid Mechanics* **8**(3), 263–280.

[6] Ataie-Ashtiani, B. & Yavari-Ramshe, S. [2011], 'Numerical simulation of wave generated by landslide incidents in dam reservoirs', *Landslides* **8**(4), 417–432.

[7] Bondevik, S., Stormo, S. K. & Skjerdal, G. [2012], 'Green mosses date the storegga tsunami to the chilliest decades of the 8.2 ka cold event', *Quaternary Science Reviews* **45**, 1–6.

[8] Bryant, E. [2014], *Tsunami: the underrated hazard*, Springer.

[9] Buckingham, E. [1914], 'On physically similar systems; illustrations of the use of dimensional equations', *Physical review* **4**(4), 345.

[10] Carey, S., Sigurdsson, H., Mandeville, C. & Bronto, S. [2000], Volcanic hazards from pyroclastic flow discharge into the sea: Examples from the 1883 eruption of Krakatau, Indonesia, *in* 'Special Paper 345: Volcanic Hazards and Disasters in Human Antiquity', Vol. 345, Geological Society of America, pp. 1–14.

[11] Cas, R. A. & Wright, J. V. [1991], 'Subaqueous pyroclastic flows and ignimbrites: an assessment', *Bulletin of Volcanology* **53**(5), 357–380.

[12] Cassar, C., Nicolas, M. & Pouliquen, O. [2005], 'Submarine granular flows down inclined planes', *Physics of fluids* **17**(10), 103301.

[13] Chorin, A. J. [1967], 'A numerical method for solving incompressible viscous flow problems', *Journal of computational physics* **2**(1), 12–26.

[14] Davies, T. & McSaveney, M. [2009], 'The role of rock fragmentation in the motion of large landslides', *Engineering Geology* **109**(1-2), 67–79.

[15] Desombre, J., Morichon, D. & Mory, M. [2012], 'Simultaneous surface and subsurface air and water flows modelling in the swash zone', *Coastal Engineering Proceedings* **1**(33), 56.

[16] Druitt, T. H., Avard, G., Bruni, G., Lettieri, P. & Maez, F. [2007], 'Gas retention in fine-grained pyroclastic flow materials at high temperatures', *Bulletin of Volcanology* **69**(8), 881–901.

[17] du Pont, S. C., Gondret, P., Perrin, B. & Rabaud, M. [2003], 'Granular avalanches in fluids', *Physical review letters* **90**(4), 044301.

[18] Ducassou, B. [2016], Modélisation de l'interaction entre un fluide à surface libre et un solide rigide soumis à des efforts extérieur par une méthode de pénalisation, PhD thesis, Université de Pau et des Pays de l'Adour, France.

[19] Ducassou, B., Nuñez, J., Cruchaga, M. & Abadie, S. [2017], 'A fictitious domain approach based on a viscosity penalty method to simulate wave/structure interaction', *Journal of Hydraulic Research* pp. 1–16.

[20] Eilers, v. H. [1941], 'Die viskosität von emulsionen hochviskoser stoffe als funktion der konzentration', *Kolloid-Zeitschrift* **97**(3), 313–321.

[21] Enet, F. & Grilli, S. T. [2007], 'Experimental study of tsunami generation by three-dimensional rigid underwater landslides', *Journal of waterway, port, coastal, and ocean engineering* **133**(6), 442–454.

[22] Frankel, N. & Acrivos, A. [1967], 'On the viscosity of a concentrated suspension of solid spheres', *Chemical Engineering Science* **22**(6), 847–853.

[23] Freundt, A. [2003], 'Entrance of hot pyroclastic flows into the sea: experimental observations', *Bulletin of Volcanology* **65**(2-3), 144–164.

[24] Fritz, H., Hager, W. & Minor, H.-E. [2004], 'Near field characteristics of landslide generated impulse waves', *Journal of waterway, port, coastal, and ocean engineering* **130**(6), 287–302.

[25] Fritz, H., Hager, W. & Minor, H.-E. [n.d.], 'Lituya bay case rockslide impact and wave run-up'.

[26] Fritz, H. M., Mohammed, F. & Yoo, J. [2009], Lituya bay landslide impact generated mega-tsunami 50 th anniversary, *in* 'Tsunami Science Four Years after the 2004 Indian Ocean Tsunami', Springer, pp. 153–175.

[27] G. Nezami, E., MA Hashash, Y., Zhao, D. & Ghaboussi, J. [2006], 'Shortest link method for contact detection in discrete element method', *International Journal for Numerical and Analytical Methods in Geomechanics* **30**(8), 783–801.

[28] GDR MiDi [2004], 'On dense granular flows', *The European Physical Journal E* **14**(4), 341–365.

[29] Goda, K. [1979], 'A multistep technique with implicit difference schemes for calculating two-or three-dimensional cavity flows', *Journal of Computational Physics* **30**(1), 76–95.

[30] Grilli, S. T., Dias, F., Guyenne, P., Fochesato, C. & Enet, F. [2010], Progress in fully nonlinear potential flow modeling of 3d extreme ocean waves, *in* 'Advances in numerical simulation of nonlinear water waves', World Scientific, pp. 75–128.

[31] Grilli, S. T., Shelby, M., Kimmoun, O., Dupont, G., Nicolsky, D., Ma, G., Kirby, J. T. & Shi, F. [2017], 'Modeling coastal tsunami hazard from submarine mass failures: effect of slide rheology, experimental validation, and case studies off the us east coast', *Natural hazards* **86**(1), 353–391.

[32] Grilli, S. T., Vogelmann, S. & Watts, P. [2002], 'Development of a 3d numerical wave tank for modeling tsunami generation by underwater landslides', *Engineering Analysis with Boundary Elements* **26**(4), 301–313.

[33] Grilli, S. T. & Watts, P. [1999], 'Modeling of waves generated by a moving submerged body. applications to underwater landslides', *Engineering Analysis with boundary elements* **23**(8), 645–656.

[34] Grilli, S. T. & Watts, P. [2005], 'Tsunami generation by submarine mass failure. i: Modeling, experimental validation, and sensitivity analyses', *Journal of waterway, port, coastal, and ocean engineering* **131**(6), 283–297.

[35] Harbitz, C. B. & Pedersen, G. [1992], 'Model theory and analytical solutions for large water waves due to landslides', *Preprint series. Mechanics and Applied Mathematics http://urn. nb. no/URN: NBN: no-23418* .

[36] Harbitz, C., Pedersen, G. & Gjevik, B. [1993], 'Numerical simulations of large water waves due to landslides', *Journal of Hydraulic Engineering* **119**(12), 1325–1342.

[37] Harlow, F. H. & Welch, J. E. [1965], 'Numerical calculation of time-dependent viscous incompressible flow of fluid with free surface', *The physics of fluids* **8**(12), 2182–2189.

[38] Heinrich, P. [1992], 'Nonlinear water waves generated by submarine and aerial landslides', *Journal of Waterway, Port, Coastal, and Ocean Engineering* **118**(3), 249–266.

[39] Heinrich, P., Piatanesi, A. & Hebert, H. [2001], 'Numerical modelling of tsunami generation and propagation from submarine slumps: the 1998 papua new guinea event', *Geophysical Journal International* **145**(1), 97–111.

[40] Heller, V. [2007], Landslide generated impulse waves, PhD thesis, ETH Zurich.

[41] Heller, V., Bruggemann, M., Spinneken, J. & Rogers, B. D. [2016], 'Composite modelling of subaerial landslide–tsunamis in different water body geometries and novel insight into slide and wave kinematics', *Coastal Engineering* **109**, 20–41.

[42] Heller, V. & Hager, W. [2011], 'Wave types of landslide generated impulse waves', *Ocean Engineering* **38**(4), 630–640.

[43] Heller, V. & Hager, W. H. [2010], 'Impulse product parameter in landslide generated impulse waves', *Journal of waterway, port, coastal, and ocean engineering* **136**(3), 145–155.

[44] Ionescu, I. R., Mangeney, A., Bouchut, F. & Roche, O. [2015], 'Viscoplastic modeling of granular column collapse with pressure-dependent rheology', *Journal of Non-Newtonian Fluid Mechanics* **219**, 1–18.

[45] Itō, S. [1977], Study of the transient heave oscillation of a floating cylinder., PhD thesis, Massachusetts Institute of Technology.

[46] Iverson, R. M. & Denlinger, R. P. [2001], 'Flow of variably fluidized granular masses across three-dimensional terrain: 1. coulomb mixture theory', *Journal of Geophysical Research: Solid Earth* **106**(B1), 537–552.

[47] Jiang, L. & LeBlond, P. H. [1992], 'The coupling of a submarine slide and the surface waves which it generates', *Journal of Geophysical Research: Oceans* **97**(C8), 12731–12744.

[48] Jiang, L. & LeBlond, P. H. [1993], 'Numerical modeling of an underwater bingham plastic mudslide and the waves which it generates', *Journal of Geophysical Research: Oceans* **98**(C6), 10303–10317.

[49] Kamphuis, J. & Bowering, R. [1970], Impulse waves generated by landslides, *in* 'Coastal Engineering 1970', pp. 575–588.

[50] Kataoka, I. [1986], 'Local instant formulation of two-phase flow', *International Journal of Multiphase Flow* **12**(5), 745–758.

[51] Kelfoun, K., Giachetti, T. & Labazuy, P. [2010], 'Landslide-generated tsunamis at réunion island', *Journal of Geophysical Research: Earth Surface* **115**(F4).

[52] Khadra, K. [1994], Méthodes adaptatives de raffinement local multigrille: applications aux équations de Navier-Stokes et de l'énergie, PhD thesis, Bordeaux 1.

[53] Lagrée, P.-Y., Staron, L. & Popinet, S. [2011], 'The granular column collapse as a continuum: validity of a two-dimensional navier–stokes model with a μ (i)-rheology', *Journal of Fluid Mechanics* **686**, 378–408.

[54] Legros, F. [2002], 'The mobility of long-runout landslides', *Engineering Geology* **63**(3-4), 301–331.

[55] Liu, P.-F., Wu, T.-R., Raichlen, F., Synolakis, C. & Borrero, J. [2005], 'Runup and rundown generated by three-dimensional sliding masses', *Journal of fluid Mechanics* **536**, 107–144.

[56] Lo, H.-Y. & Liu, P. L.-F. [2017], 'On the analytical solutions for water waves generated by a prescribed landslide', *Journal of Fluid Mechanics* **821**, 85–116.

[57] Løvholt, F., Pedersen, G. & Gisler, G. [2008], 'Oceanic propagation of a potential tsunami from the la palma island', *Journal of Geophysical Research: Oceans* **113**(C9).

[58] Lynett, P. & Liu, P. L.-F. [2002], A numerical study of submarine–landslide–generated waves and run–up, *in* 'Proceedings of the Royal Society of London A: Mathematical, Physical and Engineering Sciences', Vol. 458, The Royal Society, pp. 2885–2910.

[59] Ma, G., Kirby, J. T., Hsu, T.-J. & Shi, F. [2015], 'A two-layer granular landslide model for tsunami wave generation: theory and computation', *Ocean Modelling* **93**, 40–55.

[60] Maeno, F. & Imamura, F. [2007], 'Numerical investigations of tsunamis generated by pyroclastic flows from the kikai caldera, japan', *Geophysical Research Letters* **34**(23).

[61] Maeno, F. & Imamura, F. [2011], 'Tsunami generation by a rapid entrance of pyroclastic flow into the sea during the 1883 krakatau eruption, indonesia', *Journal of Geophysical Research: Solid Earth* **116**(B9).

[62] Maskell, S. & Ursell, F. [1970], 'The transient motion of a floating body', *Journal of Fluid Mechanics* **44**(2), 303–313.

[63] Miller, G. S., Andy Take, W., Mulligan, R. P. & McDougall, S. [2017], 'Tsunamis generated by long and thin granular landslides in a large flume', *Journal of Geophysical Research: Oceans* **122**(1), 653–668.

[64] Mio, H., Shimosaka, A., Shirakawa, Y. & Hidaka, J. [2007], 'Cell optimization for fast contact detection in the discrete element method algorithm', *Advanced Powder Technology* **18**(4), 441–453.

[65] Mohammed, F. & Fritz, H. M. [2012], 'Physical modeling of tsunamis generated by three-dimensional deformable granular landslides', *Journal of Geophysical Research: Oceans* **117**(C11).

[66] Monroy, C., Seng, S., Malenica, Š. & Veritas, B. [n.d.], 'Developpements et validation de l'outil cfd openfoam pour le calcul de tenuea la mer'.

[67] Mulligan, R. P. & Take, W. A. [2017], 'On the transfer of momentum from a granular landslide to a water wave', *Coastal Engineering* **125**, 16–22.

[68] Munjiza, A. & Andrews, K. [1998], 'Nbs contact detection algorithm for bodies of similar size', *International Journal for Numerical Methods in Engineering* **43**(1), 131–149.

[69] Nishimura, Y., Nakagawa, M., Kuduon, J. & Wukawa, J. [2005], Timing and scale of tsunamis caused by the 1994 rabaul eruption, east new britain, papua new guinea, *in* 'Tsunamis', Springer, pp. 43–56.

[70] Paris, R. [2015], 'Source mechanisms of volcanic tsunamis', *Phil. Trans. R. Soc. A* **373**(2053), 20140380.

[71] Patankar, S. [1980], *Numerical heat transfer and fluid flow*, CRC press.

[72] Pedersen, G. & Løvholt, F. [2008], 'Documentation of a global boussinesq solver', *Preprint series. Mechanics and Applied Mathematics http://urn. nb. no/URN: NBN: no-23418* .

[73] Pelinovsky, E., Zahibo, N., Dunkley, P., Edmonds, M., Herd, R., Talipova, T., Kozelkov, A. & Nikolkina, I. [2004], 'Tsunami generated by the volcano eruption on july 12–13, 2003 at montserrat, lesser antilles', *Sci. Tsunami Hazards* **22**(1), 44–57.

[74] Perkins, E. & Williams, J. R. [2001], 'A fast contact detection algorithm insensitive to object sizes', *Engineering Computations* **18**(1/2), 48–62.

[75] Petrášek, Z. & Schwille, P. [2008], 'Precise measurement of diffusion coefficients using scanning fluorescence correlation spectroscopy', *Biophysical journal* **94**(4), 1437–1448.

[76] Pianet, G., Vincent, S., Leboi, J., Caltagirone, J. & Anderhuber, M. [2010], 'Simulating compressible gas bubbles with a smooth volume tracking 1-fluid method', *International Journal of Multiphase Flow* **36**(4), 273–283.

[77] Pouliquen, O. & Forterre, Y. [2002], 'Friction law for dense granular flows: application to the motion of a mass down a rough inclined plane', *Journal of fluid mechanics* **453**, 133–151.

[78] Quemada, D. [1977], 'Rheology of concentrated disperse systems and minimum energy dissipation principle', *Rheologica Acta* **16**(1), 82–94.

[79] Roche, O., Montserrat, S., Niño, Y. & Tamburrino, A. [2008], 'Experimental observations of water-like behavior of initially fluidized, dam break granular flows and their relevance for the propagation of ash-rich pyroclastic flows', *Journal of Geophysical Research: Solid Earth* **113**(B12).

[80] Ruff, L. [2003], Some aspects of energy balance and tsunami generation by earthquakes and landslides, *in* 'Landslide Tsunamis: Recent Findings and Research Directions', Springer, pp. 2155–2176.

[81] Savage, S. B. & Hutter, K. [1989], 'The motion of a finite mass of granular material down a rough incline', *Journal of fluid mechanics* **199**, 177–215.

[82] Shi, F., Kirby, J. T., Harris, J. C., Geiman, J. D. & Grilli, S. T. [2012], 'A high-order adaptive time-stepping tvd solver for boussinesq modeling of breaking waves and coastal inundation', *Ocean Modelling* **43**, 36–51.

[83] Siebert, L. [2002], Landslides resulting from structural failure of volcanoes, *in* 'Catastrophic landslides: effects, occurrence, and mechanisms', Vol. 15, Geological Society of America, pp. 209–235.

[84] Sue, L., Nokes, R. & Davidson, M. [2011], 'Tsunami generation by submarine landslides: comparison of physical and numerical models', *Environmental fluid mechanics* **11**(2), 133–165.

[85] Vincent, S. & Caltagirone, J.-P. [1999], 'Efficient solving method for unsteady incompressible interfacial flow problems', *International Journal for numerical methods in fluids* **30**(6), 795–811.

[86] Viroulet, S. [2013], Simulations de tsunamis générés par glissements de terrains aériens, PhD thesis, Aix-Marseille.

[87] Viroulet, S., Sauret, A. & Kimmoun, O. [2014], 'Tsunami generated by a granular collapse down a rough inclined plane', *EPL (Europhysics Letters)* **105**(3), 34004.

[88] Viroulet, S., Sauret, A., Kimmoun, O. & Kharif, C. [2016], Tsunami waves generated by cliff collapse: comparison between experiments and triphasic simulations, *in* 'Extreme Ocean Waves', Springer, pp. 173–190.

[89] Wang, Y. & Mason, M. T. [1992], 'Two-dimensional rigid-body collisions with friction', *Journal of Applied Mechanics* **59**(3), 635–642.

[90] Ward, S. N. & Day, S. [2001], 'Cumbre vieja volcano—potential collapse and tsunami at la palma, canary islands', *Geophysical Research Letters* **28**(17), 3397–3400.

[91] Watts, P. [1997], Water waves generated by underwater landslides, PhD thesis, California Institute of Technology.

[92] Watts, P., Grilli, S., Kirby, J., Fryer, G. & Tappin, D. [2003], 'Landslide tsunami case studies using a boussinesq model and a fully nonlinear tsunami generation model', *Natural Hazards And Earth System Science* **3**(5), 391–402.

[93] Watts, P., Grilli, S. T., Tappin, D. R. & Fryer, G. J. [2005], 'Tsunami generation by submarine mass failure. ii: Predictive equations and case studies', *Journal of waterway, port, coastal, and ocean engineering* **131**(6), 298–310.

[94] Watts, P. & Waythomas, C. [2003], 'Theoretical analysis of tsunami generation by pyroclastic flows', *Journal of Geophysical Research: Solid Earth* **108**(B12).

[95] Watts, P. et al. [2003], Underwater landslide shape, motion, deformation, and tsunami generation, *in* 'The Thirteenth International Offshore and Polar Engineering Conference', International Society of Offshore and Polar Engineers.

[96] Waythomas, C. F. & Watts, P. [2003], 'Numerical simulation of tsunami generation by pryoclastic flow at aniakchak volcano, alaska', *Geophysical research letters* **30**(14).

[97] Wei, G., Kirby, J. T., Grilli, S. T. & Subramanya, R. [1995], 'A fully nonlinear boussinesq model for surface waves. part 1. highly nonlinear unsteady waves', *Journal of Fluid Mechanics* **294**, 71–92.

[98] Yavari-Ramshe, S. & Ataie-Ashtiani, B. [2016], 'Numerical modeling of subaerial and submarine landslide-generated tsunami waves—recent advances and future challenges', *Landslides* **13**(6), 1325–1368.

[99] Yim, S. C., Yuk, D., Panizzo, A., Di Risio, M. & Liu, P.-F. [2008], 'Numerical simulations of wave generation by a vertical plunger using rans and sph models', *Journal of waterway, port, coastal, and ocean engineering* **134**(3), 143–159.

[100] Zhao, T., Utili, S. & Crosta, G. [2016], 'Rockslide and impulse wave modelling in the vajont reservoir by dem-cfd analyses', *Rock Mechanics and Rock Engineering* **49**(6), 2437–2456.

[101] Zweifel, A., Hager, W. H. & Minor, H.-E. [2006], ‘Plane impulse waves in reservoirs’, *Journal of waterway, port, coastal, and ocean engineering* **132**(5), 358–368.